The Generation of Mesoscale
Hydrodynamic Phenomena by the Grappler
and Whiting Seamounts, Southeast of Puerto Rico*

by

Jorge E. Capella

The Generation of Mesoscale
Hydrodynamic Phenomena by the Grappler
and Whiting Seamounts, Southeast of Puerto Rico*

by

Jorge E. Capella

*MS Thesis, Marine Sciences, RUM UPR (1983)

ABSTRACT

This work presents the results of research on topo-
graphically generated mesoscale eddies in the region of the
Grappler and Whiting Seamounts which are located 22km south-
east of Puerto Rico. Three different data sets were used:
1) site specific hydrographic data, 2) satellite images from
TIROS/NOAA, Landsat and Skylab satellites, and 3) free-
drifting drogued-buoy tracks. A reference current meter
station was established at the Benchmark B OTEC site (17°
57.3' N, 65° 51.5' W), at a depth of 20 meters. Predictions
from numerical and analytical models were tested using the
site specific data and then compared to experimental re-
sults. The hydrographic and drogue data definitively estab-
lish the presence of perturbations over the seamounts which
are qualitatively consistent with model predictions. Closed
contour regions in the distribution of dynamic heights, tem-
perature, salinity and dissolved oxygen were found in the
surface and subsurface waters above the top of Grappler Sea-
mount. Horizontal flow perturbations, detected down to 100m,
probably extend deeper. Whiting Seamount's effect was de-
tected in the depth range from 200-300m, also near its top.
Two distinct warm and cold regions were detected over this
seamount. A cyclonic eddy-like feature located close to
Grappler Seamount, in the satellite images, also suggests
that eddies are being shed from the seamount region.

RESUMEN

En este trabajo se investiga la formación de fenómenos hidrodinámicos en las aguas oceánicas al sureste de Puerto Rico las cuales son generados por los montes submarinos de Grappler y Whiting, 22km al sureste de la isla. Se utilizaron tres técnicas diferentes en la recopilación de datos: 1) muestreo hidrográfico, 2) fotos tomadas por satélites, y 3) trayectorias de boyas en la vecindad del Monte Grappler. Se ocupó una estación de referencia para la observación de las corrientes marinas en el punto llamado Benchmark B (17° 57.3'N, 65° 51.5'W), a una profundidad de 20m. Las predicciones de varios modelos numéricos fueron probadas con los datos hidrográficos y topográficos específicos para el área. El resultado de esta prueba fué luego comparado con los productos gráficos descriptivos creados en base a los datos hidrográficos, las fotos de satélite y las trayectorias de boyas. Los datos establecen la presencia de perturbaciones sobre los montes submarinos las cuales son consistentes con las predicciones teóricas. Sobre la cima del Monte Grappler se observaron regiones circulares (eddies) en la representación gráfica de las distribuciones de la anomalía geopotencial, la temperatura, la salinidad y el oxígeno disuelto en las aguas superficiales y cercanas a la superficie. Ajustes en las trayectorias de las boyas debido a la presencia del Monte Grappler fueron observadas

hasta una profundidad de 100m. El efecto producido por
el Monte Whiting se detectó en profundidades entre 200 y
300m, cerca de su cima. La distribución de los parámetros
revela dos regiones diferentes, una de baja temperatura
y otra de alta temperatura (relativas al ambiente cir-
cundante) sobre este monte submarino. Una estructura
similar a un "eddy" fué detectada en las fotos de satélite
al suroeste del Monte Grappler, su tamaño y posición son
indicativos de una posible asociación con el monte submarino.

ACKNOWLEDGEMENTS

First of all, I want to sincerely thank Dr. Manuel L. Hernandez-Avila who, aside from being the chairman of my graduate committee, is also a great friend; his counsel and guidance led me through the hardest moments. Thanks to all the personnel of the Marine Ecology Division and the Department of Marine Sciences, specially to Vance P. Vicente for his help with the photographic work, to Ms. Mary Brecken and Mr. Angel Alers for the drafting work, to Ms. Terry Robles who typed this document and very specially to Dr. John A. Fornshell for his day to day support. This research was conducted under partial support from the U.S. Department of Energy, Contract No. DE-AC05-76OR01833. The research was performed under appointment to the Laboratory Graduate Participation Program administered by Oak Ridge Associated Universities for the U.S. Department of Energy.

TABLE OF CONTENTS

LIST OF TABLES

Text:

APPENDIX C:

LIST OF PLATES AND FIGURES

Plates:

Figures:

INTRODUCTION

Oceanographic observations conducted during the last decade (1970-1980) have established the role of underwater topographic features as sources of flow perturbations in the world oceans. The effect of islands, reefs, canyons, ridges, bumps (Charleston Bump), banks, seamount chains and isolated seamounts in the generation of dynamic oceanic variability at various space and time scales is well-documented in the scientific literature.

Oceanographic research conducted in the Caribbean Sea revealed the existence of mesoscale eddies in the oceanic environment south and southeast of Puerto Rico (Fornshell and Capella, 1981). These eddies, with length scales in the order of 20km, were observed in the vicinity of the Grappler and Whiting Seamounts. The possible relationship between these mesoscale eddies and the seamounts became quite evident in spite of the fact that the hydrographic station spacing utilized was too large to conclusively establish such a relationship.

As a continuation of the previous study, the objectives of this work are to answer the following questions:

    1) Are the Grappler and/or Whiting Seamounts generating detectable perturbations?

    2) If so, what kind?

3) How does the answer to (1) and (2)

compare with theoretical predictions?

To answer these questions a field data set was obtained to allow us to approach the first question in a variety of ways. The data set consisted of: 1) closely spaced hydrographic data from the seamount region, 2) satellite images for the area, and 3) buoy drifter trajectories near Grappler Seamount. These data provided a detailed oceanographic description of the seamount region. The parametric predictions from the theoretical models of Hogg (1973), Huppert (1975) and Huppert and Bryan (1976), which are based on Taylor column theory regarding the formation of closed streamline regions (Taylor columns or eddies) by seamounts, were then tested against the field data; the outcome was then compared to the descriptive data from the seamount region.

The characterization of dynamic perturbations generated by the Grappler and Whiting Seamounts is of practical importance in relation to the establishment of an OTEC (Ocean Thermal Energy Conversion) plant anywhere in Puerto Rico's south coast. Changes to the thermal resource available to an OTEC plant could affect the criteria for its establishment; seamounts are known to generate perturbations in the temperature field. These seamounts are close enough to shore (22km from Punta Tuna) as to be potentially important thru the advection of nutrients, pollutants and plankton

along Puerto Rico's south coast, in affecting the insular shelf environment and circulation. These seamounts are also important fishing grounds, specially the Grappler Seamount, whose yield could also be related to the environmental changes produced by the dynamics of seamount-flow interactions.

LITERATURE REVIEW

Most observations of dynamic perturbations associated with seamounts and other topographic features have been interpreted in terms of Taylor column theory (Hogg, 1973; Huppert, 1975; Huppert and Bryan, 1976; Vastano and Warren, 1976; Eide, 1979; Owens and Hogg, 1980). A Taylor column is the stagnant region formed over an obstacle immersed in a homogeneous, slow moving fluid in a rapidly rotating system. The flow is divided by the obstacle into two symmetric branches with the region in between remaining motionless all the way to the surface (Davies, 1972). Such a feature was first experimentally created by Taylor (1923).

Although the theory explaining Taylor column formation in homogeneous fluids dates from early in this century (Proudman, 1916; Taylor, 1917), observations of related phenomena in nature were few and ambiguous before 1970. Creation of Taylor columns in the laboratory is a classical experiment in fluid dynamics; the theory evolved from the simple case of homogeneous flows to the more realistic case of stratified flows and beta (B) effects (Hogg, 1973; Huppert, 1975; McCartney, 1975). The theory became popularly known through attempts by Hide (1961) to explain Jupiter's red spot as a huge Taylor column (a term he established). Recent interest in Taylor column theory arose from attempts to explain the highly variable deep currents

4

reported by Swallow (1960) using neutrally buoyant floats (Huppert and Bryan, 1976). These currents were thought of as originating from flow-bottom topography interactions.

Other theories have been proposed to explain the formation of eddies by seamounts. Eide (1979) discussed the possibility that clockwise polarized oscillating currents could induce circulation around a seamount while the storage of tidal energy could account for the cold dome over it. Lack of adequate tidal (and non-tidal) current information for the region does not allow for the testing of these theories in our study site.

The first set of observations that definitively established the existence of a Taylor column in the ocean was provided by Owens and Hogg (1980) for an unnamed seamount in the recirculation region of the Gulf Stream. Thru the use of hydrographic and long-term current meter data they established a correlation between the density field perturbation and the generation of negative vorticity (anticyclonic motion) over the seamount. Previous oceanographic observations only suggested the presence of such a phenomena. Defant (1940) reported on hydrographic and current meter data in the region of the Altair Seamount, an extinct submarine volcano north of the Azores. An upward displacement of the isotherms over the extinct volcano was interpreted as originating from a cyclonic eddy whose speed decreases towards the bottom. If the assumption is made of increasing

speeds with depth then the sense of rotation changes and the results agree with Taylor column theory. We must remember that in Defant's time the concept of slow moving deep water was still prevalent.

Vastano and Warren (1976) interpreted eddies, observed in potential temperature contours in the vicinity of the Atlantis II Seamount, in terms of Hogg's (1973) theory although they acknowledged the lack of definitive evidence to prove it. Eide (1979) presented hydrographic and current meter data collected around Halten Bank, on the Norwegian continental shelf. A cold dome found over the bank is also interpreted in terms of Hogg's (1973) and Huppert's (1975) theories although the current meter data were not adequate to describe any type of circular motion.

Perturbations in the vicinity of seamounts have also been observed in the Emperor Seamount Chain, in the Kuroshio Extension (Roden, et al., 1982), the coast of Alaska (Tabata, 1982) and in the North Pacific (Royer, 1975).

Drifter trajectories near the New England Seamount Chain, and nearby seamounts, have shown both cyclonic and anticyclonic motions which are undoubtedly associated with the seamounts (Richardson, 1981; Schmitz, et al., 1981). The lack of synoptic hydrographic data made it impossible to determine the structure of these rotating regions.

No investigation on the dynamics of seamount-flow interactions had been conducted in the Caribbean Sea previous to this work.
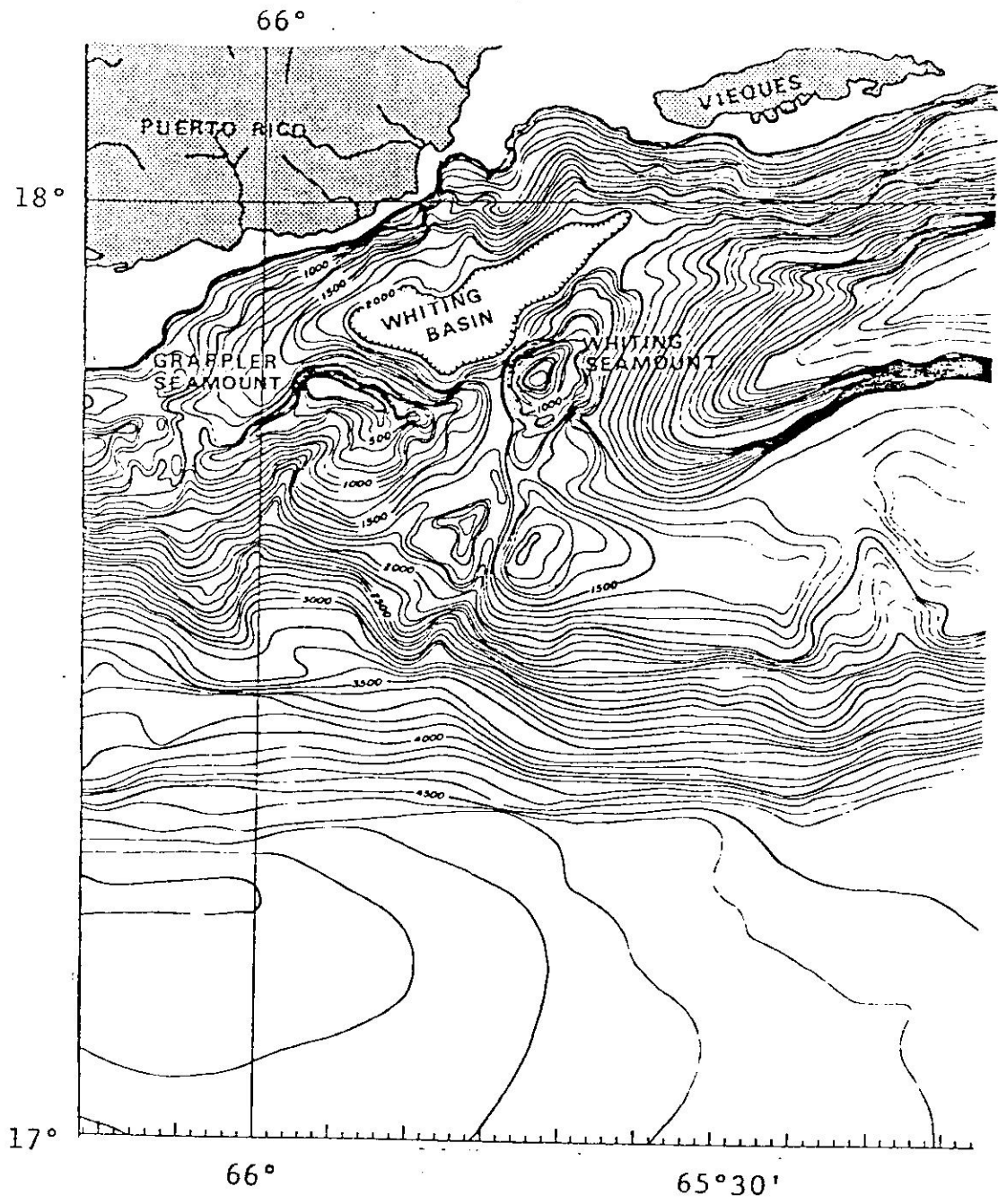
Figure 1. Seamount Region: bottom contours and
main topographic features. Depth in
meters. (from Trumbull, et al., 1981)

SITE DESCRIPTION

A. Physical Description of the Grappler and Whiting Sea-
   mounts and the Major Topographic Features in the Area.

Grappler Seamount is a mountain-like feature which
rises almost 1400m above the sea floor on Puerto Rico's
southern insular slope. Its long axis measures 9.5 km and
its short axis is 2 km in length at the 100m depth contour.
At a depth of 500m the dimensions are 13 and 5 km in length,
respectively. The smaller, more radially-symmetrical
Whiting Seamount is east of Grappler Seamount. Its di-
ameter is 4 km at a depth of 500m. Figure 1 shows the
bottom depth contours for the area, Figure 2 shows a magni-
fication of the seamount region.

Grappler Seamount rises to a depth of less than 100m
from the surface (70m is the observed minimum); the Whiting
Seamount to a depth of about 200m (218m is the reported
minimum). They are bounded on the north by the Whiting
Basin which is very flat at 2000m in depth (Goldman, et al.,
1979). Further to the north is the island of Puerto Rico
(22 km to Punta Tuna) and the Virgin Islands Passage. To
the west and south is the insular slope which plunges down
to the Venezuela Basin at an angle of about 4 degrees. The
Virgin Island Basin and the island of St. Croix, to the
east, lie at the southern limit of the Anegada-Junsfern

9
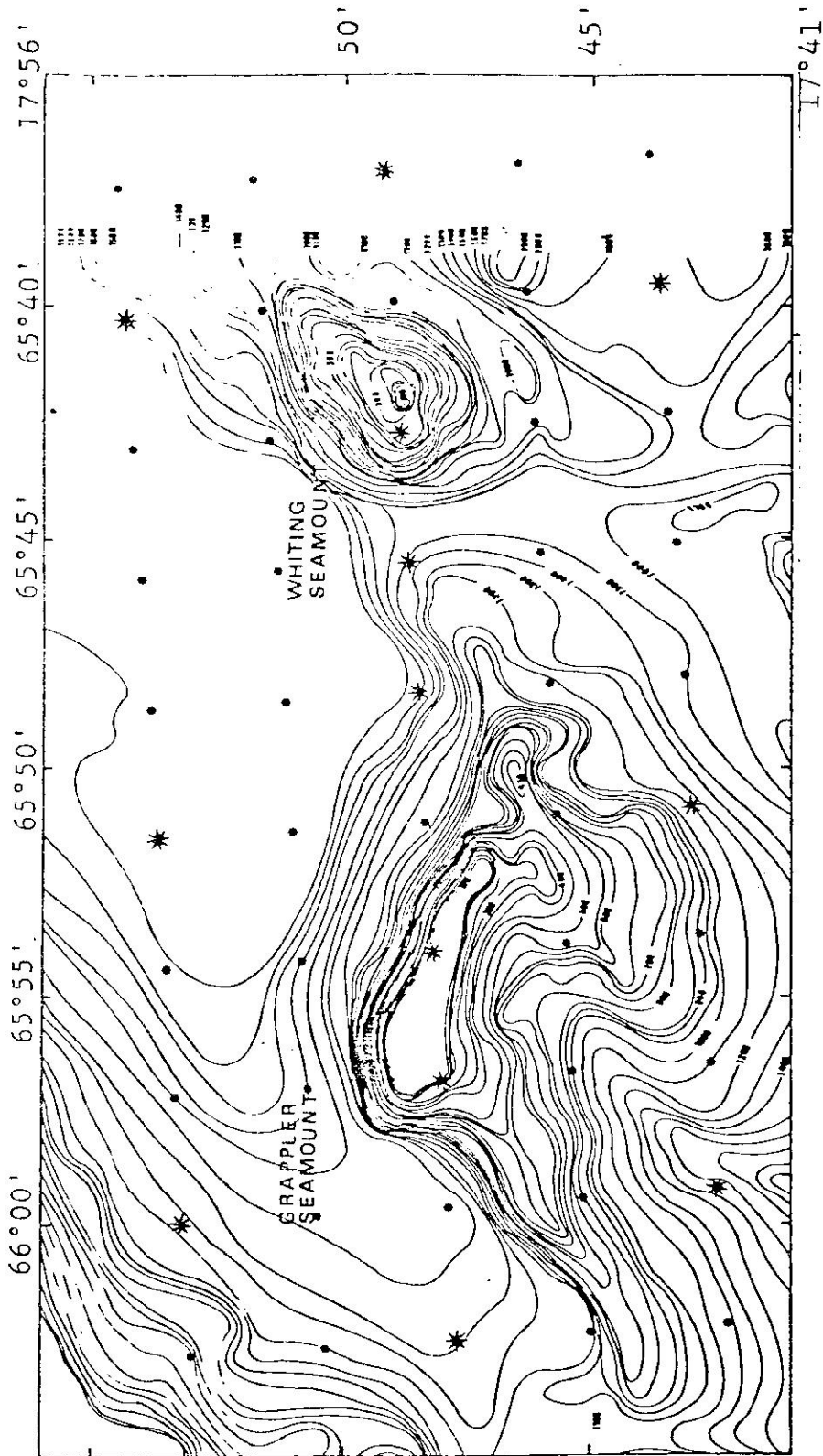
Figure 2. Magnification of the Grappler and Whiting Seamount area
showing Seamount Survey station positions; * = XBT
※ = XBT + hydrocast. Depth in meters. (from U.S.G.S. map no.
H-9595)

Passage, the only deep water channel in this part of the Caribbean (Metcalf, 1976).

Figures 3a, 3b and 3c show seismic profiles taken across both seamounts for the lines indicated in Figure 3d. As can be seen in these profiles both seamounts rise from the southern boundary of the Whiting Basin. Their elevation, relative to the basin floor, would be closer to 2000m than to the 1400m average depth. It is also important to notice the steep, flat, asymmetrical shape of the top of Grappler Seamount (like that of a guyot) versus the smooth, symmetric shape of Whiting Seamount. Due to their different shapes both seamounts could interact differently with the waters moving over them. Figure 4 shows a depth sounder trace taken on the R/V SULTANA over Grappler Seamount on a north-south direction near its center. Even at this high resolution the top of the seamount is remarkably flat and the edges are very steep.

B. Water Masses

The water mass structure of the north-eastern Caribbean Sea has been described by several investigators (Wust, 1964; Sturges, 1965; Gordon, 1967; Atwood, 1976; Nelepo, 1976 and Morrison, 1982). Recent results from the Center for Energy and Environment Research (CEER) investigations repre-sent the most detailed effort at describing the oceanic environment south and southeast of Puerto Rico. The water

a) R-101

b) R-103
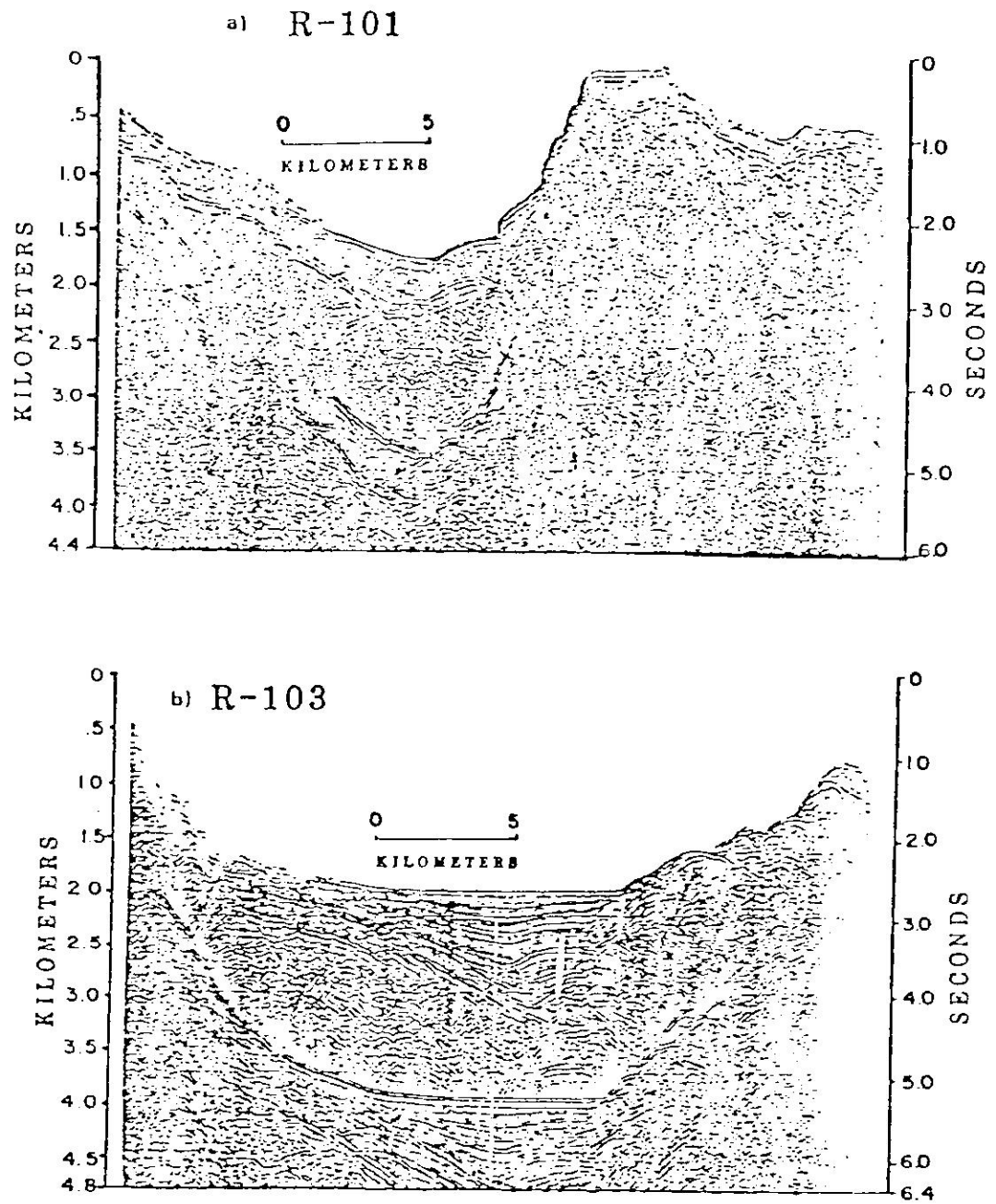
Figure 3. Seismic profiles: a) Grappler West,
b) Grappler East. (from Trumbull,
et al., 1981)

c) R-105-D
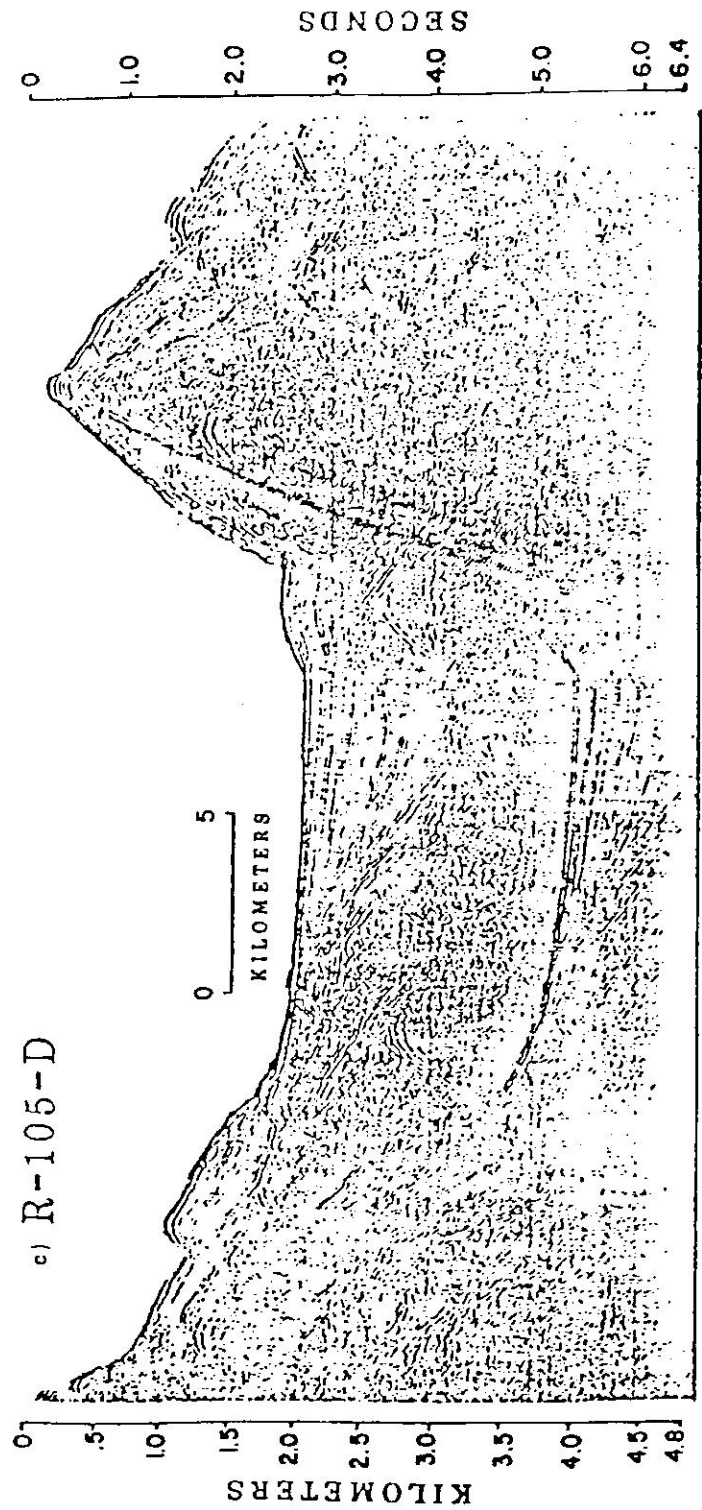
Figure 3c. Whiting Center. (from Trumbull, et al., 1981)
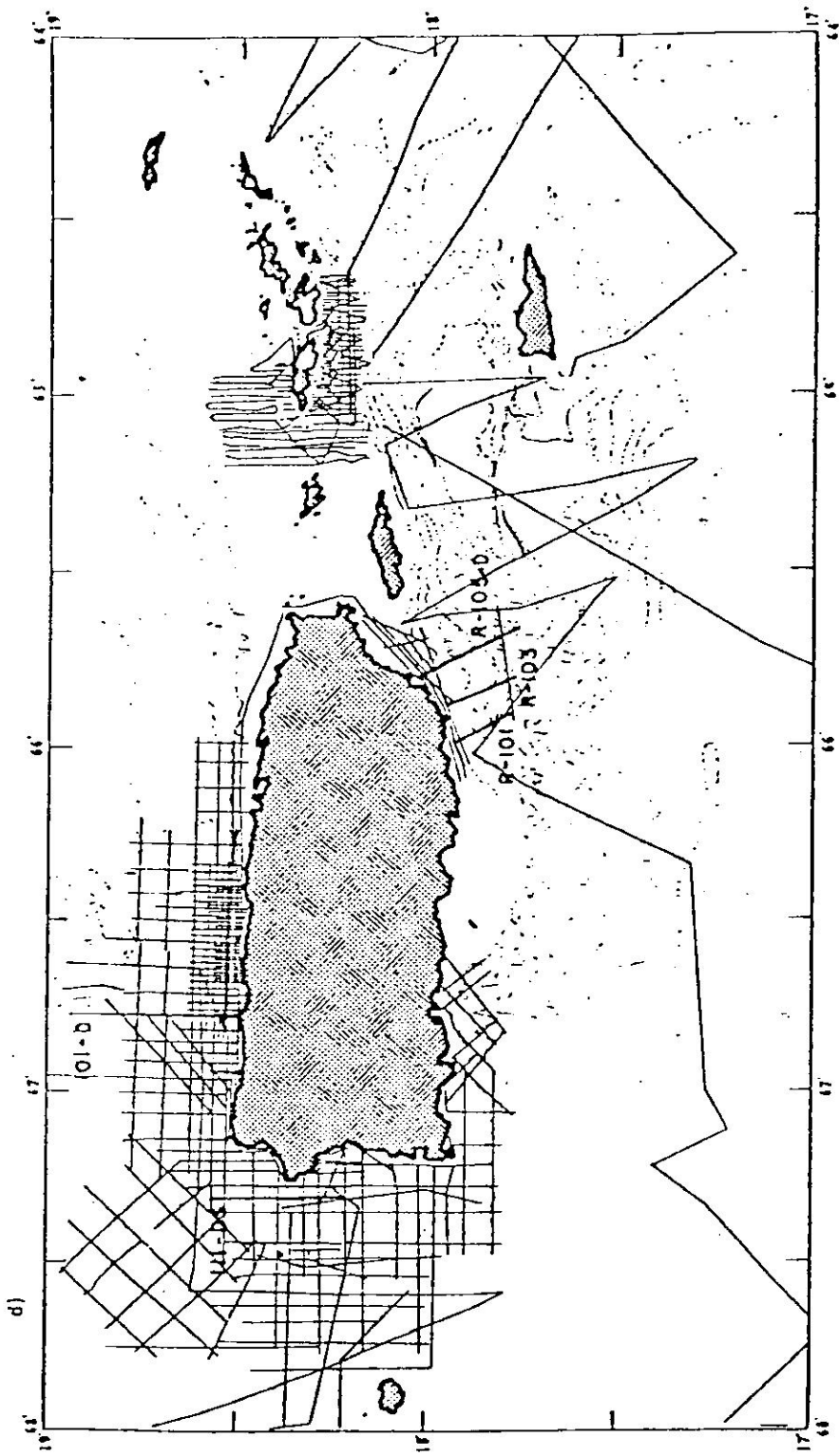
Figure 3d. Guide to transects. (from Trumbull, et al., 1981)
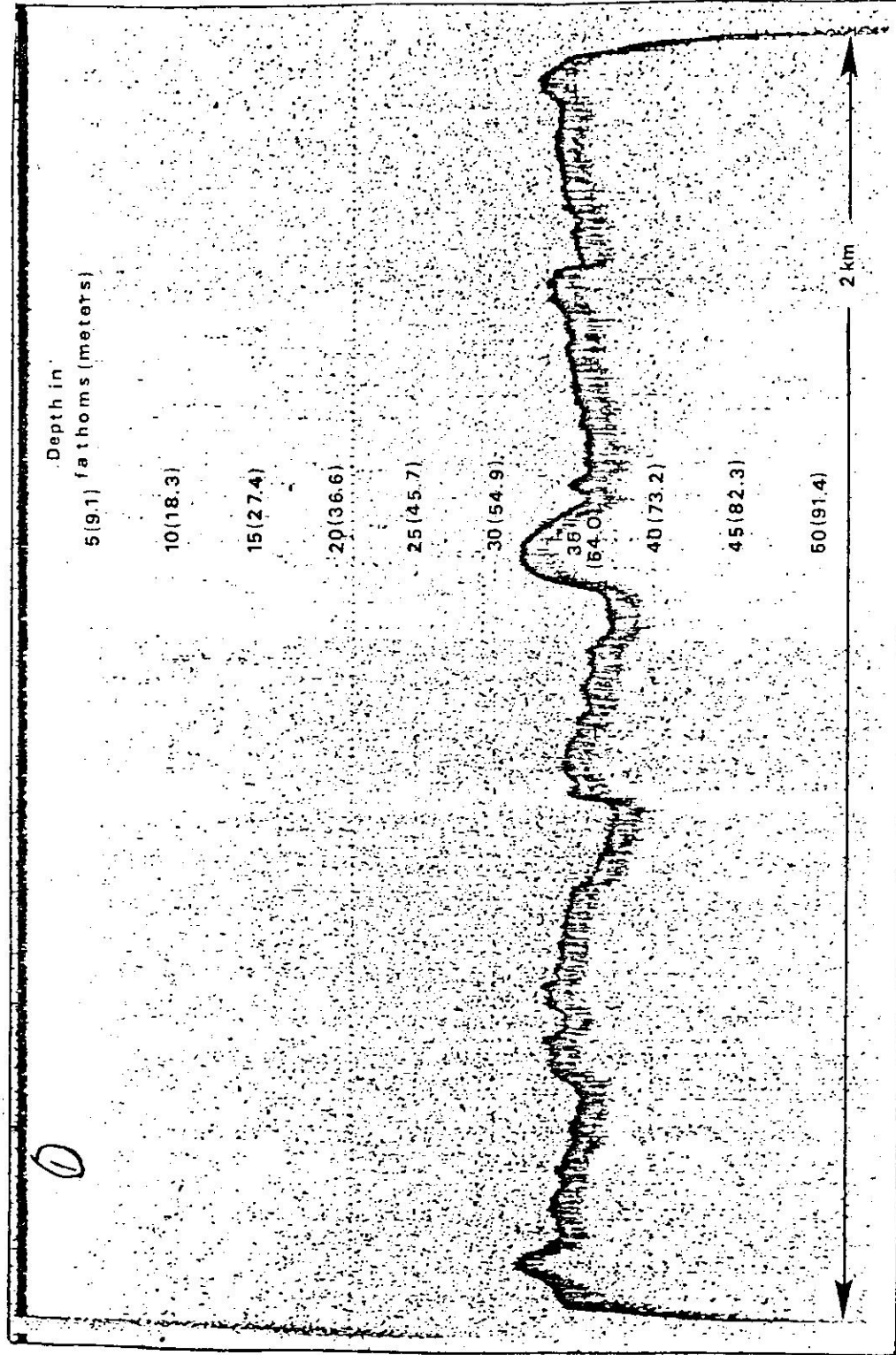
Figure 4. North-south depth sounder trace over Grappler Seamount.

mass description cited here is based on preliminary a-
nalyses of seven CEER cruises during January, March, May,
July, September and November 1980 and February 1981 (López,
et al., 1981). Data from these cruises are fitted into
Wust's (1964) framework which has come to be accepted as
the standard by most subsequent investigators referenced
above.

The water column south and southeast of Puerto Rico is
regarded as being constituted of six main layers (see
Figure 5) having the following characteristics:

1. The Caribbean Surface Water (or Surface
    Mixed Layer) is a homogeneous water mass
    which occupies the region above the sea-
    sonal thermocline. This thermocline is
    best defined in terms of a steep temper-
    ature or density gradient whose depth
    varies seasonally. Figure 6 shows the
    thermocline depth versus time. The
    greatest thermocline depths were found
    in January-March (>90m); the shallowest
    depths were found in September (<25m).
    An inshore-offshore gradient was found
    in all seven CEER cruises with mixed
    layer depths decreasing in the offshore
    direction. This fact is due to the ac-
    cumulation of waters, by wind stress, in
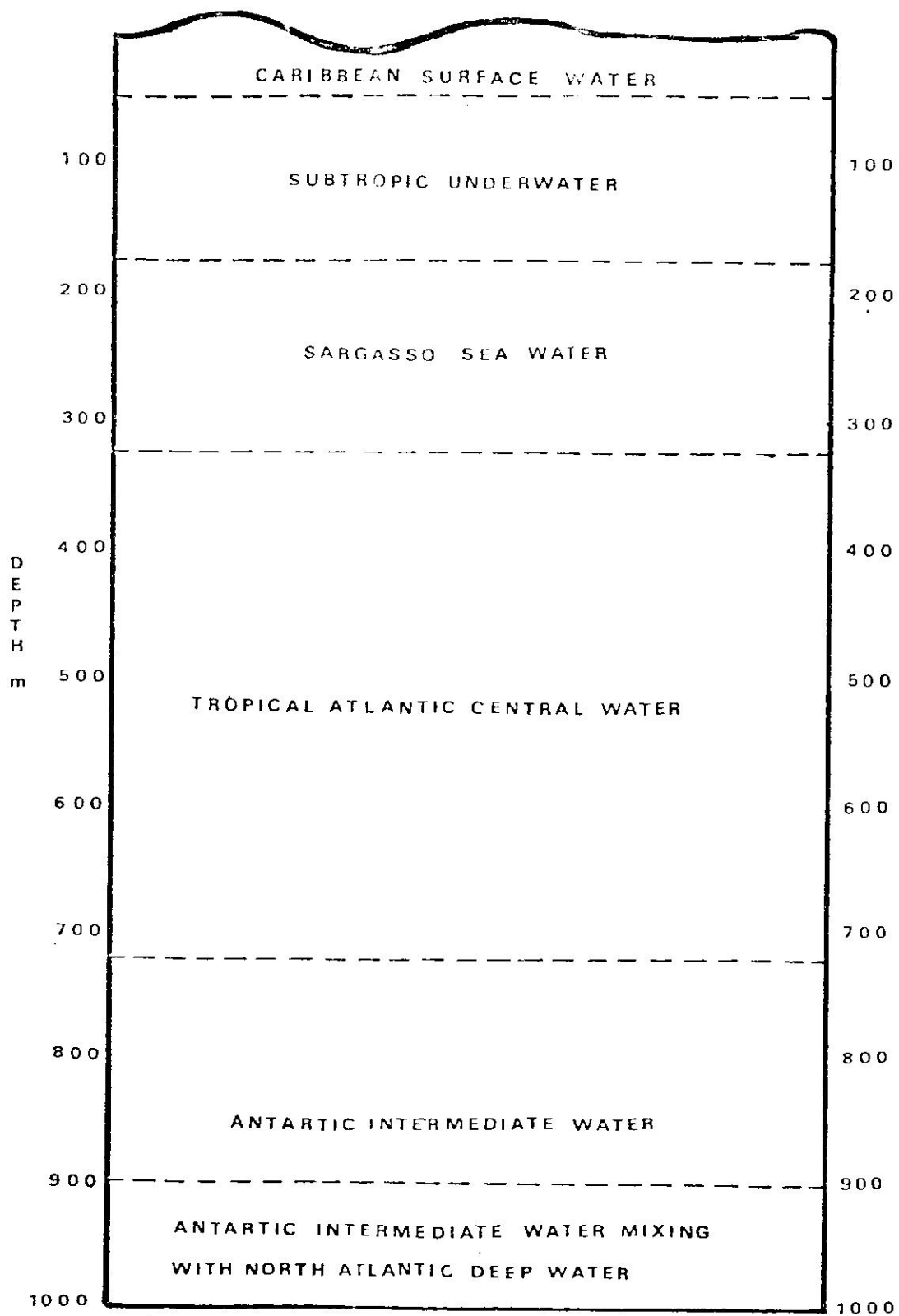
Figure 5.   Schematic representation of the
            vertical water mass distribution
            south and southeast of Puerto Rico.
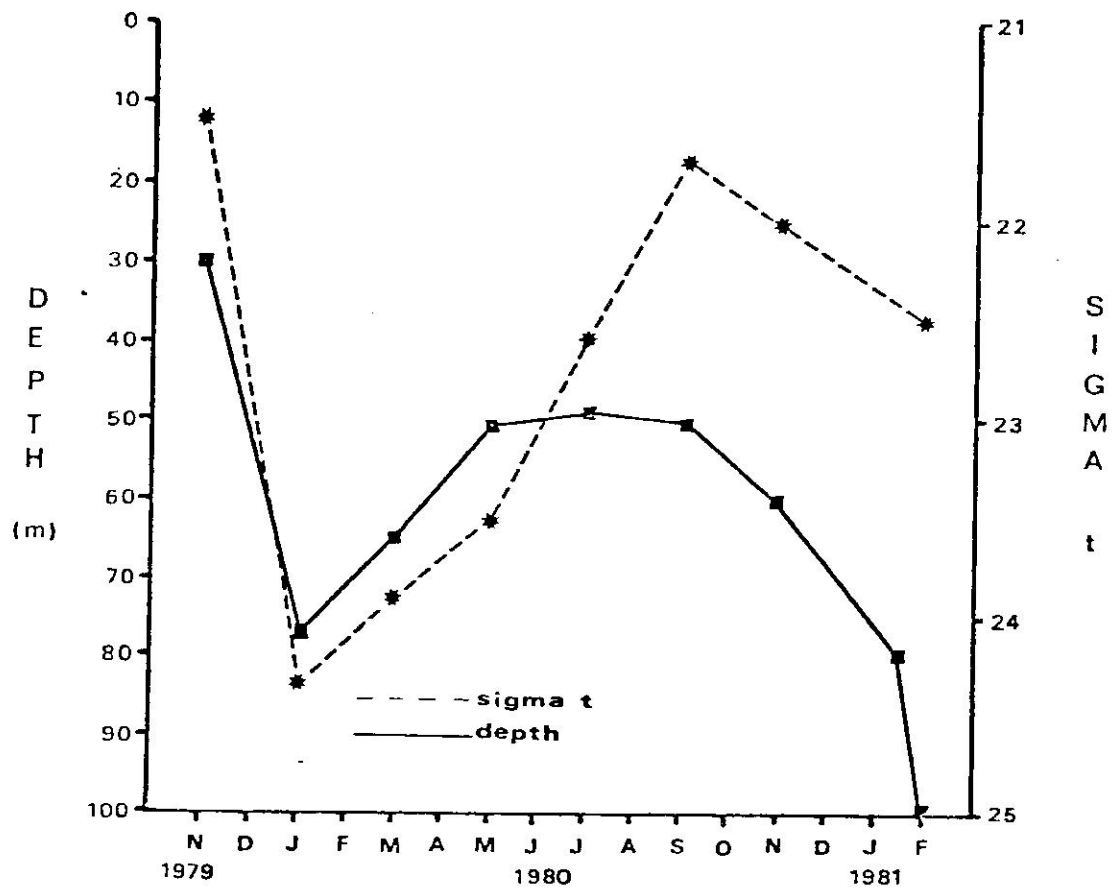
Figure 6. Thermocline (mixed layer) depth, and sigma-t versus time for off-shore waters south and southeast of Puerto Rico.

this region of the Caribbean Sea (Gordon, 1967; Atwood, 1976).

Surface salinity values show a maximum during March-May and a minimum in September. This has been well-documented and is related to the Amazon-Orinoco River discharge (Froelich and Atwood, 1976; Worthem, et al., 1976). Sigma-t, salinity and temperature variations follow the same seasonal pattern with sigma-t maxima occurring as a function of maximum salinity and temperature minima, and vice versa.

Dissolved oxygen values were found to be higher during January-March and lower in July-September. A subsurface maximum around a depth of 75m was present during the May-July-September cruises. This maximum is associated with the chlorophyl maximum and generally occurs below the thermocline. Inshore-offshore gradients (or discontinuities) were observed in dissolved oxygen and salinity concentrations but those patterns are not clear yet.

2. A Subtropical Underwater (SUW) mass is defined by a salinity maximum core of 37.00°/oo at around 125m in depth. In this layer salinity values increase in the offshore direction.

3. The Sargasso Sea Water (SSW) core was defined by Kinard, et al. (1974) as having 36.5°/oo salinity, 18°C temperature and 4.4 ml/L maxima in dissolved oxygen. This water mass was found at depths between 250-275 meters.

4. A Tropical Atlantic Central Water (TACW) is characterized by a dissolved oxygen minima (<3.0 ml/L) which was found very close to a depth of 675m at most of the monitored stations.

5. The Antarctic Intermediate Water (AIW) is identified by a salinity minimum of 34.8-34.9°/oo at a depth of approximately 800m.

6. North Atlantic Deep Water (NADW) mixing with AIW is responsible for the salinity and dissolved oxygen concentration increase found at a depth of 1000m. This mixture extends all the way to the bottom and, owing to certain changes occurring

in the Venezuela Basin, has been re-
ferred to as Venezuela Basin Water
(VBW) (Atwood, 1976).

The Caribbean Surface Water is by far the most variable
of all water masses described above. Low frequency varia-
bility was found in the deeper layers but this has not been
fully investigated. In a composite diagram of sigma-t
versus depth for all CEER cruises most of the change is
concentrated in the upper 300m (Figure 7).

A strong internal wave field is present in the Bench-
mark area. Figure 8 shows a typical isotherm depth versus
time plot obtained thru a XBT time series during the
September (1980) CEER cruise. These internal waves
generate variability in the depth distribution of all water
mass properties, at a fixed spot, which must be taken into
account before spatial variability can be ascertained.

C. Currents and Circulations

The mean, long-term motion of Caribbean Sea waters
at the study site is towards the west-southwest, at all
depths above approximately 1000m. Waters deeper than
1000m oscillate on an east-west axis imposed by the bathy-
metry of the Jungfern-Anegada Passage, the only deep water
passage in the northeastern Caribbean Sea (Wust, 1964;
Gordon, 1967; Atwood, 1976; Metcalf, 1976; Molinari, et
al., 1981; Morrison and Nowlin, 1982). Great variability
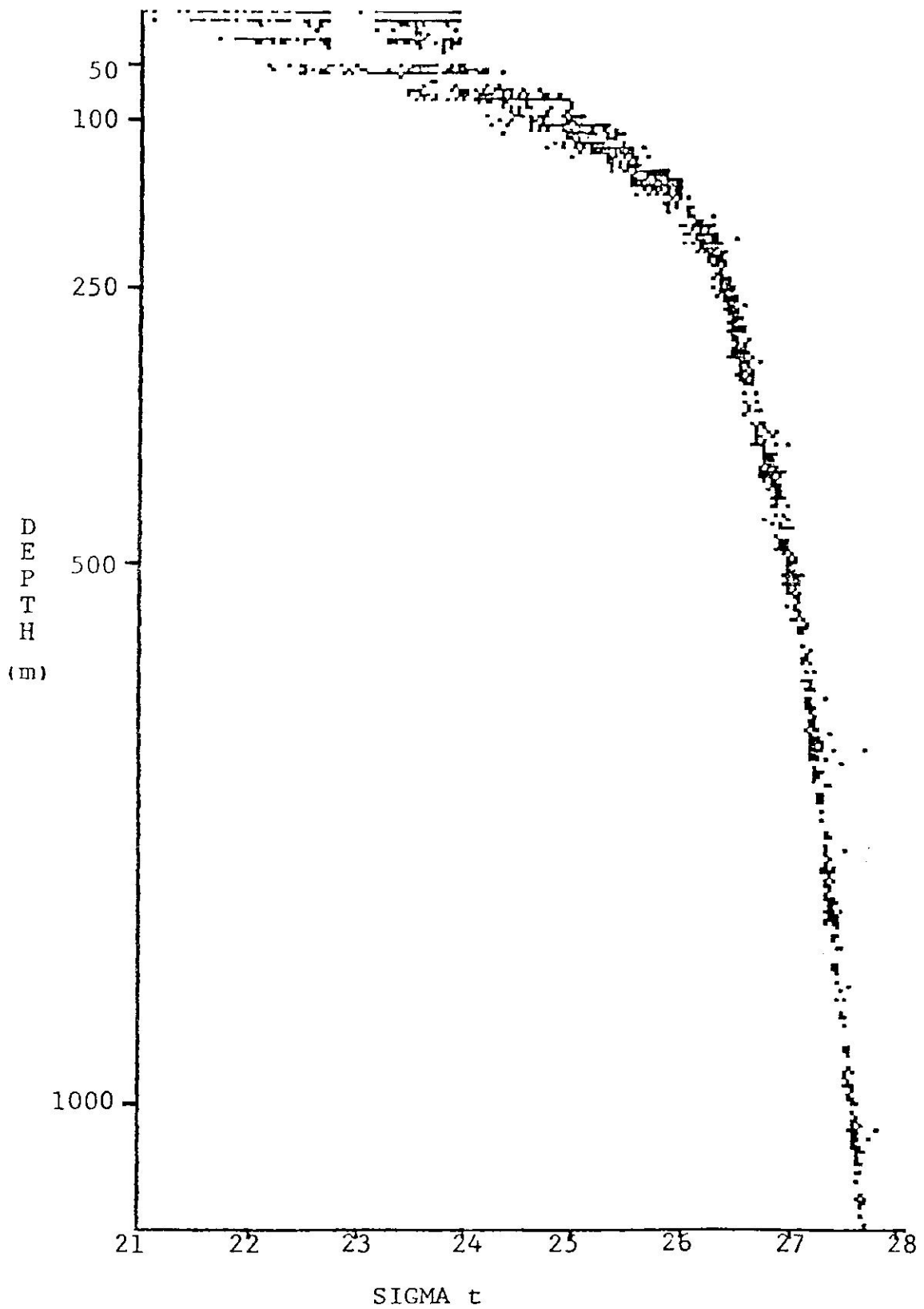
Figure 7. Sigma-t versus depth for all
CEER cruises.
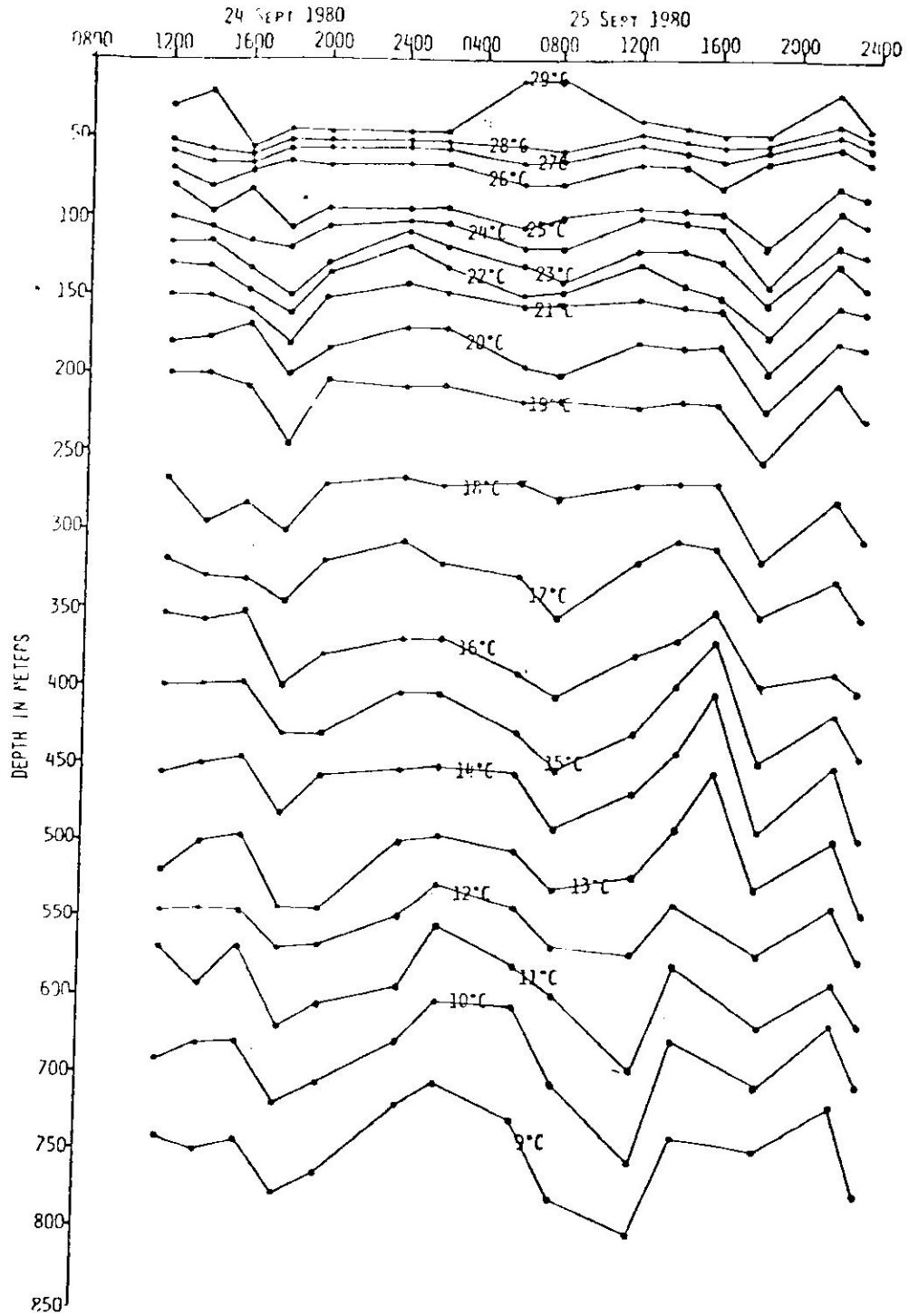
Figure 8. September XBT time series.

has been observed in currents at all depths with flows towards all compass bearings reported for the study region.

The main driving force of surface and subsurface waters is the Northeastern Trade Wind Belt, which is one of the most persistent wind regimes in the world.

MATERIALS AND METHODS

A. Seamount Hydrographic Survey

The survey was conducted from the R/V CRAWFORD during
October 15-16, 1981. The purpose of the cruise was to
obtain a detailed description of the water mass and density
structure of the waters around the seamounts. A grid of
fifty hydrocast and/or XBT (expendable bathythermograph)
stations were occupied; thirteen stations were hydrocast+
XBT stations and the rest were XBT stations (Figure 2).

The stations were spaced 5 km apart in a 900 km area
extending 15 km to the west, 10 km to the east and 10 km
perpendicular to a line drawn through the center of both
seamounts. This configuration was chosen due to the fact
that both seamounts were adequately covered at a scale
comparable to the length scale (radius at the base) of the
smaller seamount (5 km). The entire grid was completed in
38 hours. A list of all station positions is given in
Appendix A.

The instruments and techniques described below are
almost similar to those used during the seven CEER cruises.
Specific differences between both sampling strategies will
be pointed out.

1. Hydrocasts

Thirteen hydrocast stations were occupied during the cruise (Figure 2). Five-liter Niskin bottles were positioned at nominal depths of 0, 10, 25, 50, 75, 100, 125, 150, 200, 250, 300, 400, 500, 650, 800, 1000 and 1500 meters. This depth arrangement is similar to the one used during the CEER cruises with the exception of the 1500m bottle which was added to establish an adequate reference level for the dynamic computations. All the water masses in the water column are sampled with this arrangement and the data should be consistent with previous CEER hydrographic data.

Each Niskin bottle was equipped with a rack for the reversing thermometers. Three deep sea reversing thermometers, of recent calibration, went in each rack on the bottles at nominal depths of 75 to 1500 meters. Two of these thermometers were of the protected type and the third one was unprotected. The shallow bottles (0 to 50 meters) carried only two protected thermometers. The temperatures obtained in this way are accurate to 0.02°C; the depth estimates are accurate to less than 5 meters at a depth of 1000 meters.

Water samples from each bottle were analyzed for salinity and dissolved oxygen. Salinity was determined using a Hytech, Model 620, Inductive Salinometer with an

accuracy of $0.003^\circ/_{oo}$. Dissolved oxygen was determined by the Winkler method as revised by Carpenter (1965) and modified by Anderson (1971). Measurements are accurate to 0.02 milliliters/liter.

2. Expendable Bathythermographs (XBT's)

A Sippican Expendable Bathythermograph System R-603 was used to obtain temperature vs. depth profiles to determine the water column temperature structure around the seamounts. Two complete systems were employed during the cruise, one system used T-7 probes which reached down to 800 meters in depth and the other system used T-5 probes which went as deep as 1500 meters. Both sets were calibrated before and after the cruise and both functioned correctly. Figure 9 shows the distribution between the deep and shallow probes for the occupied stations.

3. Hydrographic Data Analyses

Hydrographic data from the survey were processed with an Apple II mini-computer. Software was developed to obtain final values from the raw data, to interpolate these data to standard levels, and to calculate all derived quantities (sigma-t, specific volume anomaly and geopotential anomaly). Appendix B gives all the formulas used for these calculations, together with all relevant information and references. XBT data were manually extracted from the records for all standard levels.

27
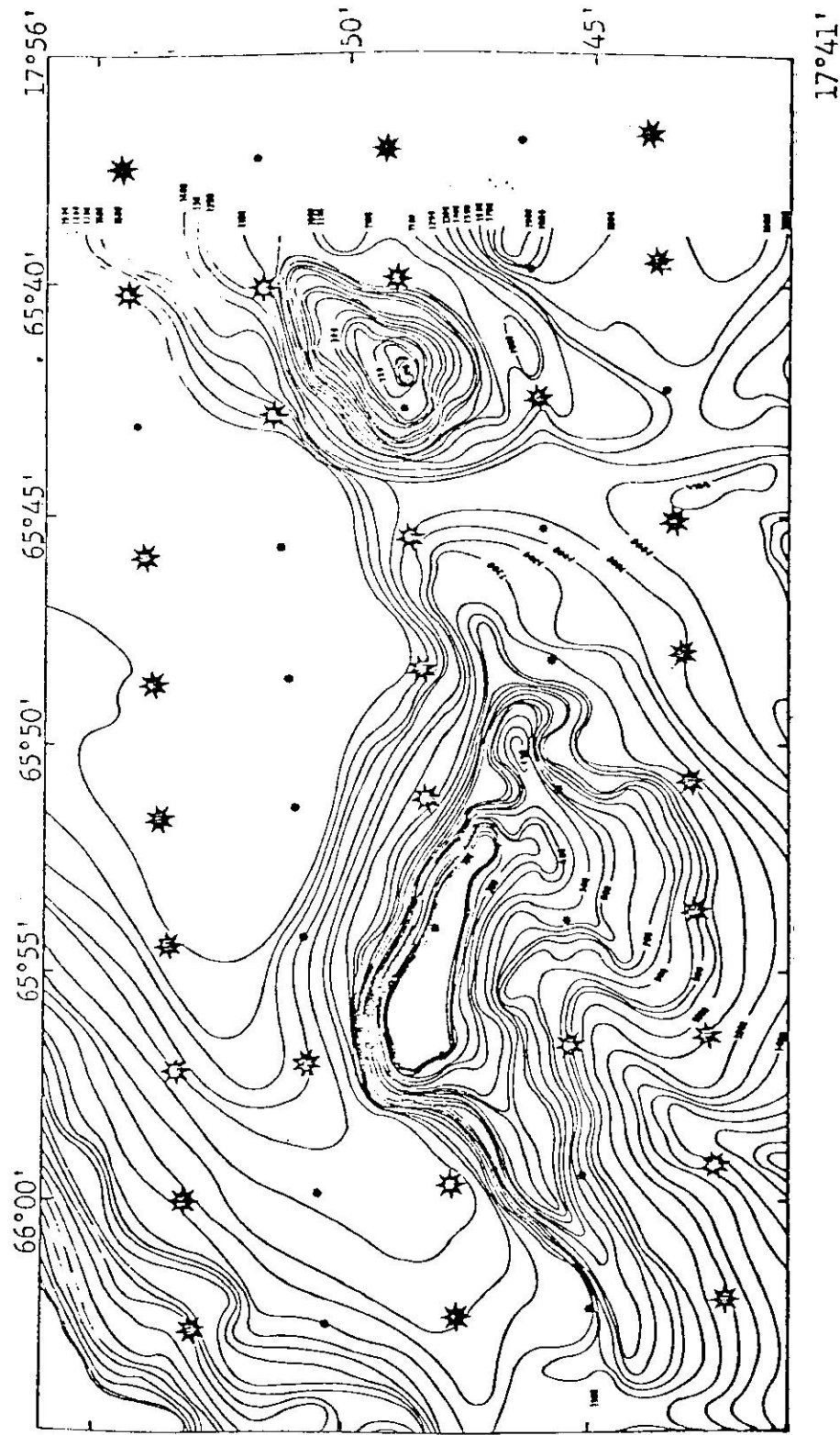
Figure 9. Distribution among deep (✸) and shallow (✳) XBTs.

The final product of the analyses is a set of contour maps at all standard depths for each of the following parameters: salinity, thermometric temperatures, XBT temperatures, dynamic heights (referenced to the 1000, 800 and 500m depth levels) and dissolved oxygen. An estimate of the variability of a given parameter at all standard levels was obtained from CEER Benchmark data. Multiple occupations at Benchmark B (Fig. 1) were executed during the seven CEER cruises, four hydrocasts were performed during a 36 hour period in each cruise. The sampling during the Seamount Survey was conducted in 38 hours so the time interval under consideration is approximately similar on all occasions. The Seamount Survey was performed during October, 1981 so Benchmark data from the September and November 1980 cruises were utilized. These data were interpolated using the same methods as for the Seamount Survey data and the sample variances among the four values at each level were calculated. This Benchmark variance was compared to the variance calculated for each parameter, for each level, from the Seamount Survey data in order to obtain a f-ratio (Seamount var./Benchmark var.) (Sokal and Rohlf, 1969a). The f-ratios relative to September and November (1980) are included in each parameter contour map, as well as the critical F value for the appropriate degrees of freedom in both the 95% and 90% confidence intervals (Sokal and Rohlf, 1969b). A significant difference between the two

variances (Seamount var. > Benchmark var. in this one tailed test) will be that for which the f-ratio exceeds the critical F value at the chosen confidence interval.

B. Current Meters

On October 5, 1981 two InterOcean, Model 135, Savonious-rotor type current meters were suspended from a moored Landing Craft Utility (LCU) at the OTEC Benchmark B. The two current meters were at depths of 20 and 200 meters for a period of 24 days, which included the time interval during which the Seamount Survey was conducted. At the time of removal it was found that the meter from 200 meters had a malfunctioning rotor so the speed data were useless (zero speeds). The other current meter (20m deep) had functioned properly.

The record from the current meter at a depth of 20m was digitized manually, with data points every ten minutes. The resultant time-series was analyzed thru the use of the OCEANS program developed at the Department of Marine Sciences. This program performs a variety of basic statistical calculations on the data and also creates high quality graphic products. The speed data were also subjected to a standard Fourier analysis in order to resolve the different periodicities present in the record.

C. Satellite Images

Forty-four satellite images, covering the seamount area, were examined in search of seamount-generated effects. Of these images, 22 were produced by satellites from the ITOS-NOAA series; 11 are from Landsat and 11 are from Sky-lab. Appendix C contains the I.D. number (for Landsat and Skylab scenes), format, date and frequency range for each image. This set is not by any means exhaustive in terms of all suitable images available from these satellites, but it is felt that the sample is representative regarding quality, area coverage and perspective.

ITOS-NOAA images were obtained directly from NOAA's Satellite Data Services Division at Washington, D.C. These images were requested for dates coincident, or close to, the CEER cruises. The observations were made by the Advanced Very High Resolution Radiometer (AVHRR) sensor on board the polar orbiting satellites of the TIROS-NOAA series. The AVHRR is a five channel imaging device whose resolution is approximately one kilometer at the satellite subpoint. Visible (channel 1, 0.62um) and infrared (channel 4, 11.0um) versions of the same scenes were obtained in the form of 25-by-25 cm black and white contact prints.

Landsat and Skylab images were requested from the U.S. Geologic Survey's EROS Data Center at Sioux Falls, South Dakota. A computer search was performed for the seamount

area and a portion of the higher quality images was selected. The most recent item on the listing was dated 1980. Apollo/Gemini products, aerial mapping and NASA aerial photography were also included in this search, but none of the images covered the critical area. The photographic products were carefully examined thru a dissecting binocular microscope.

D. DNR-NOAA Buoy Drift Data

During 1982 eight groups of window shade drogued buoys were deployed and tracked for four days (96 hrs) each time, off southeastern Puerto Rico. The drogues had a surface area of 1.86 m^2 and the buoys a surface area of 0.061 m^2. Three of the groups were deployed at a depth of 200m, three at 50m and two at 100m. Each group consisted of two drogues at the same depth except for the eighth cruise when four drogues were deployed. The buoys were tracked by the R/V SULTANA, using the ship's radar to determine position. Drifts from the first and last surveys are discussed in this work as they entered the Grappler Seamount region.

E. Numerical and Analytical Models

The theories of Hogg (1973), Huppert (1975) and Huppert and Bryan (1976) are used in this work: 1) to test their parametric predictions regarding the formation of closed streamline regions by an obstacle immersed in a rotating, moving fluid, and 2) to compare their results for ideal

conditions against our experimental findings from this study. All these theories are based on the classic Taylor column theory for homogeneous (unstratified) flows. Good reviews on the development of this theory are found in the introductions to the above-mentioned papers.

N.G. Hogg (1973) developed an analytical model to describe the effect of small, circularly symmetric topography on the slow, steady flow of an inviscid, incompressible, diffusionless, horizontally uniform, baroclinic current. The fluid is vertically stratified with a constant Brunt-Vaisala frequency (N) and a linear upstream shear (U'o(z); where the nondimensional speed at a depth z is given by Uo(z)=Uo(0)+z*U'o(z). His results define the parametric region in which closed streamlines are formed and also the vertical extent of this perturbation in terms of a stratification parameter $S=(NH/fL)^2$, a topographic parameter $B=hofLU*o(0)/HU^2$ and the previously defined upstream shear U'o(z); where H is the vertical length scale (mean depth around the obstacle), f is the Coriolis parameter ($2\Omega sin(latitude)$), L is the horizontal length scale (equal to the radius), ho is the obstacle's height, U*o(0) is the flow speed at the obstacle's level and U is the velocity scale given by $U=[\frac{1}{H} \int_o^H U*o(z*)^2 dz]^{0.5}$.

Values were calculated for S and B using the field hydrographic data and the real seamount configurations. The effect of the upstream shear in the final results is

rather small and can be ignored. The values for S and B obtained from the seamount site were then tested to determine the vertical extent of the perturbation as predicted by Hogg (1973). A perturbation is formed for all B (in the case of a right circular cylinder for which Hogg solved his equations).

Various important model assumptions are violated by the seamount site: 1) the seamounts are not relatively small, 2) the fluid stratification is not constant, and 3) our seamounts do not have a right cylindrical shape (although Grappler Seamount is nearly flat topped). The agreement between predictions and observations will determine whether the differences are more relevant, for the model, than the similarities.

Huppert (1975) solves analytically the same set of equations solved by Hogg (1973) only that the solution is expressed in a more general way which allows the consideration of arbitrary shapes for the obstacle. He arrives at the important conclusion that an obstacle with nearly vertical faces will induce closed streamline regions no matter how small it is. This may apply to Grappler Seamount due to its steep northwest slope and nearly flat top. The system he modelled consists of two planes in uniform rotation about a vertical axis; an obstacle of everywhere non-negative height is attached to the lower plane, and the fluid is constrained to flow between the

two planes. He assumed that the volume of the obstacle is finite and that the far upstream flow is uniform. His obstacle is also circularly symmetric, although the shape is arbitrary. His results are expressed in terms of $B=NH/fL$ (which is equal to the square root of Hogg's (1973) S) and $hoR-1$ (numerically equivalent to Hogg's B); where N is the Brunt-Vaisala frequency, H is the mean depth around the obstacle, f is the coriolis parameter, L is the horizontal length scale of the obstacle (effective radius) and R is the Rossby number (V/fL; where V is the far up-stream barotropic speed). Table I (from Huppert, 1975) shows the critical height, $\alpha=BhoR-1$, in the case of strong stratification ($B=>\infty$) for various obstacle configurations. The penetration of the disturbance produced by objects of more than critical height is given by fL/N.

Huppert and Bryan (1976) developed a numerical model in order to study the temporal evolution, starting from a state of rest, of the same system whose steady state solution had been analytically solved in Huppert (1975) and Hogg (1973). An analytical model is then described which approximates the numerical solution and allows more general conclusions to be made. The model predicts the formation of cyclonic (warm) and anticyclonic (cold) eddies due to the redistribution of relative vorticity induced by obstacles of greater than critical height, as determined by Huppert (1975). The warm eddy is either

TABLE I. Critical height (α) for the formation of a
Taylor Cone over an obstacle immersed in a
strongly stratified fluid ($B=>\infty$).
From Huppert (1975)

Obstacle	Shape ($h(r)$)		α
Cylindrical lens	$(1-r^2)$	; $(r<=1)$	1.75
	0	; $(r>=1)$	
Hemisphere	$(1-r^2)^{\frac{1}{2}}$	; $(r<=1)$	1.27
	0	; $(r>=1)$	
Cylindrical Gaussian	e^{-r^2}	; $(r<\infty)$	0.86
Flat-topped cylinder	1	; $(r<1)$	1.0
	0	; $(r>1)$	

$r=$ obstacle's relative radius; $h(r)=$shape as a function of
r; $\alpha=$theoretical critical height for various obstacle
configurations; $B=$stratification parameter

shed away or trapped around the cold eddy depending on the current speed. In a simple order of magnitude conclusion, the authors state that for large values of $B=NH/fL$, if Nhm/Uo is greater than a number of order unity, a Taylor column is formed above the topographic feature and if Nhm/Uo (hm is the obstacle's maximum height and Uo is the upstream barotropic speed after a time t_o) is greater than a number of order ten, the shed eddy remains close to the topographic feature.

RESULTS AND DISCUSSION

The dynamic features observed in the data are found
at well-defined depth intervals or layers. This vertical
distribution provides the framework for the following
discussion.

A. Surface and Subsurface Waters (<70m in depth)

Both the geostrophic current measurements at the sea-
mount region, and the direct Eulerian current meter obser-
vations at the Benchmark B, revealed a south-southwest
flow of nearly 15 cm/s at a depth of 20m, during the sea-
mount survey period. Geostrophic speeds ranged from 14 to
17 cm/s while the mean speeds at Benchmark remained at
14.8 cm/s towards a direction of 241° T for the period of
October 5 to 29 and 14.1 cm/s towards a direction of 131.7°
T for October 15 to 16 (synoptic with the seamount survey).
This close agreement in current velocities at a depth of
20m corroborates the geostrophic current profile and the
use of the 800m depth reference level in the dynamic compu-
tations. These velocities are also in close agreement with
those obtained for the period of March 15-19 (1982) using
Lagrangian drifters deployed at a a depth of 50m, whose
trajectories are shown in Figure 10. During this de-
ployment the southern (180°T) flow remained steady for at
least three days, when the experiment was terminated. The
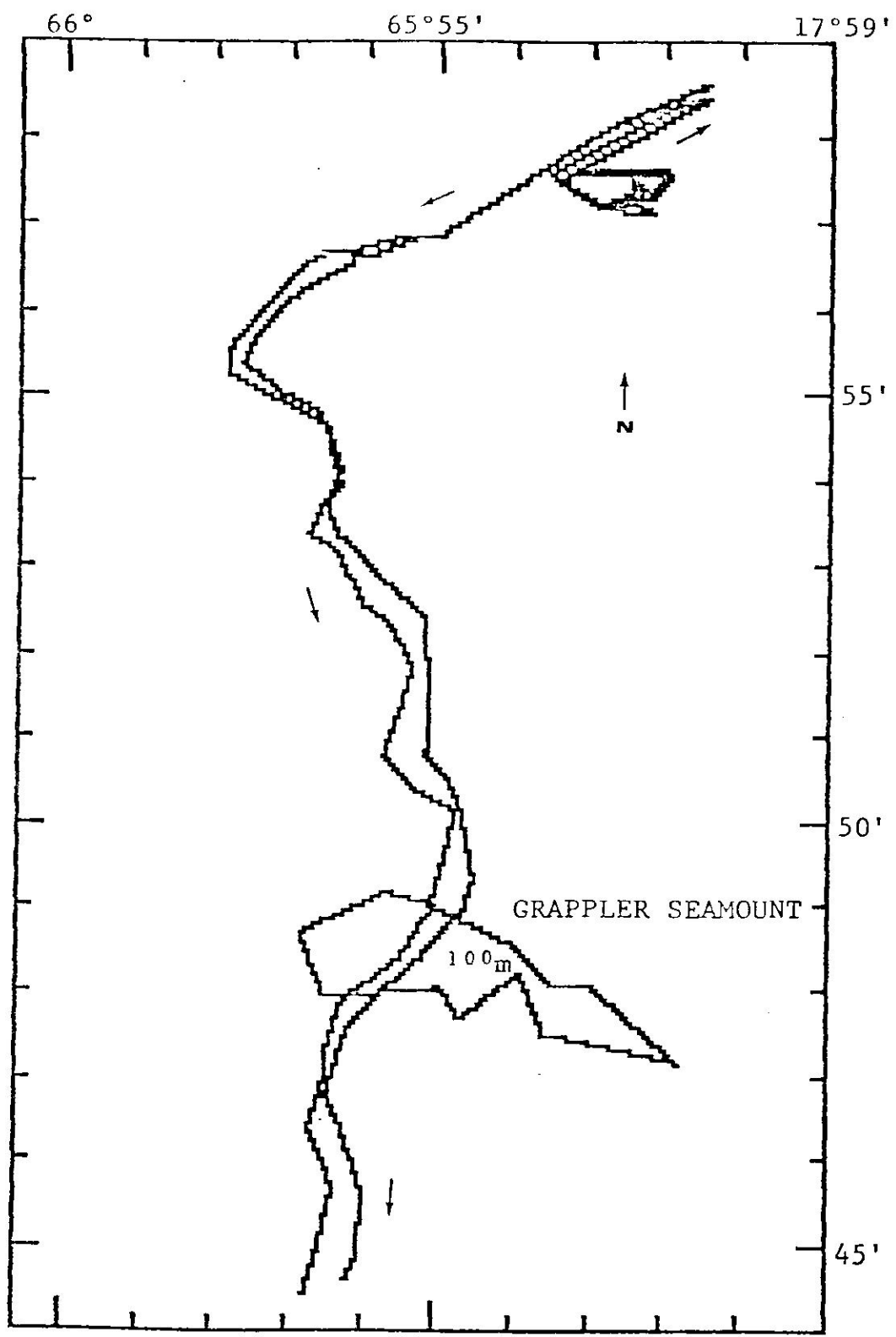mean speed during this period was 14.7 cm/s for both

Figure 10.   Drifter trajectory over Grappler
Seamount from March 15 to 19, 1982.
The drifter was drogued at a depth
of 20m.

drifters. This south-southwest current seems to be the most frequent flow pattern in the area, although observations of currents towards all directions, at all depths, have been reported by many authors using a variety of monitoring techniques (Atwood, 1976; Nelepo, 1976; Metcalf, 1976; Goldman et al., 1979; Goldman and Hernandez, 1979; Fornshell, 1982).

Figures 11, 12 and 13 show the parameter topographies at the surface and at the 20 and 50m isobaths. Each contour plot shows the f-ratios and the 95% confidence limits as an indication of signal strength against variability at Benchmark B. The surface and subsurface geostrophic flow pattern consisted of a south-southwest moving current which turned to the left (looking downstream) upon approaching Grappler Seamount, turned to the right after passing it and then continued on a more westerly direction. This flow pattern around Grappler Seamount looks very much like the streamline pattern expected outside (higher than) the region of closed streamlines produced by an obstacle with a vertical face (Hogg, 1973), or of more than critical height (Bho/R), as is the case for this seamount (Huppert, 1975; Huppert and Bryan, 1976). Such a streamline pattern is shown in Figure 14c.

The region of high salinity, low temperature (high density) and low dissolved oxygen (D.O.) over Grappler Seamount, most clearly defined at a depth of 20m, can be
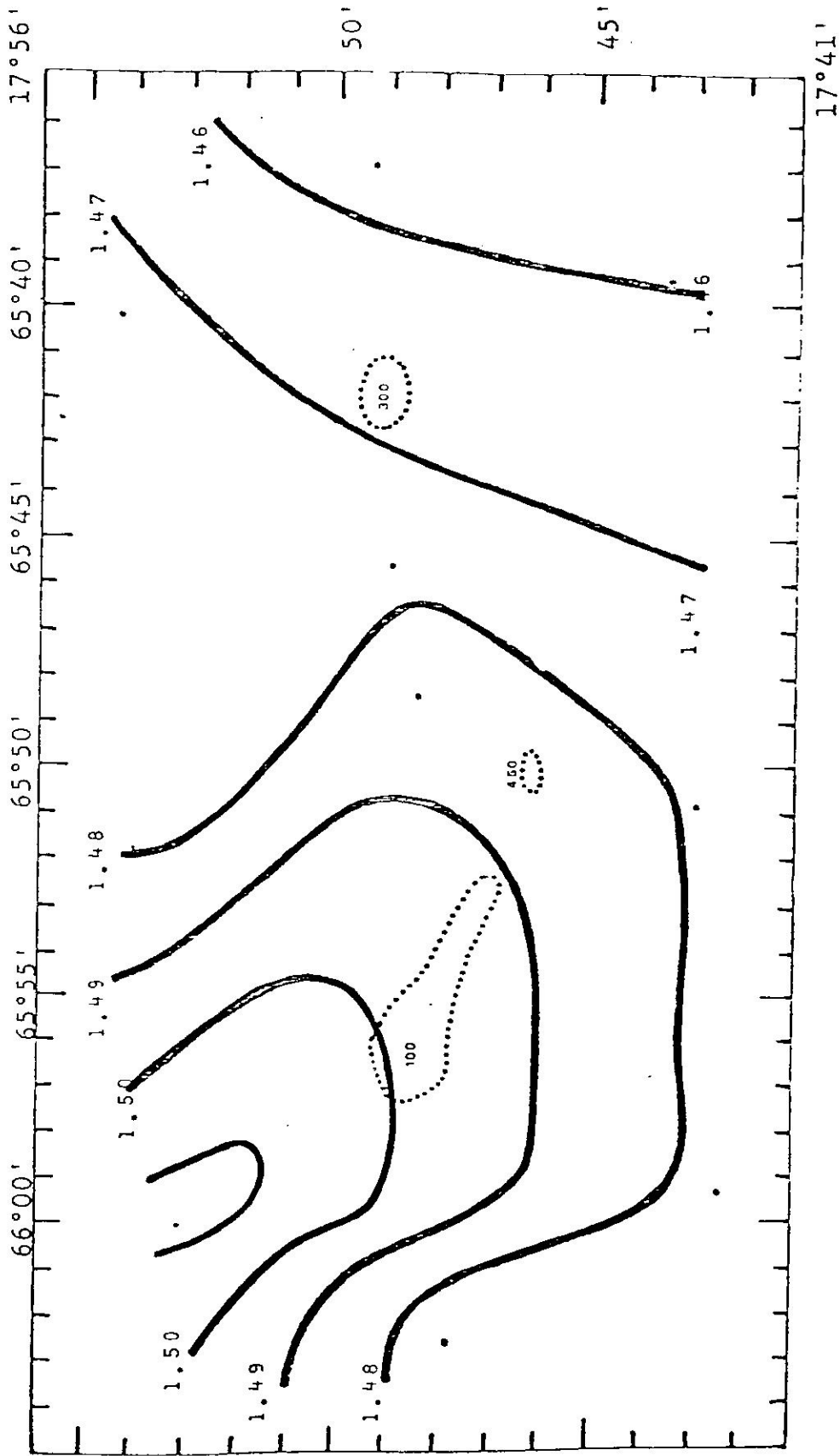
Figure 11. Parameter contours at the surface: dynamic heights relative to the 800m reference level. 95% F_c = 8.79, 90% F_c = 5.23, f_{sept} = 1.28, f_{nov} = 2.07.
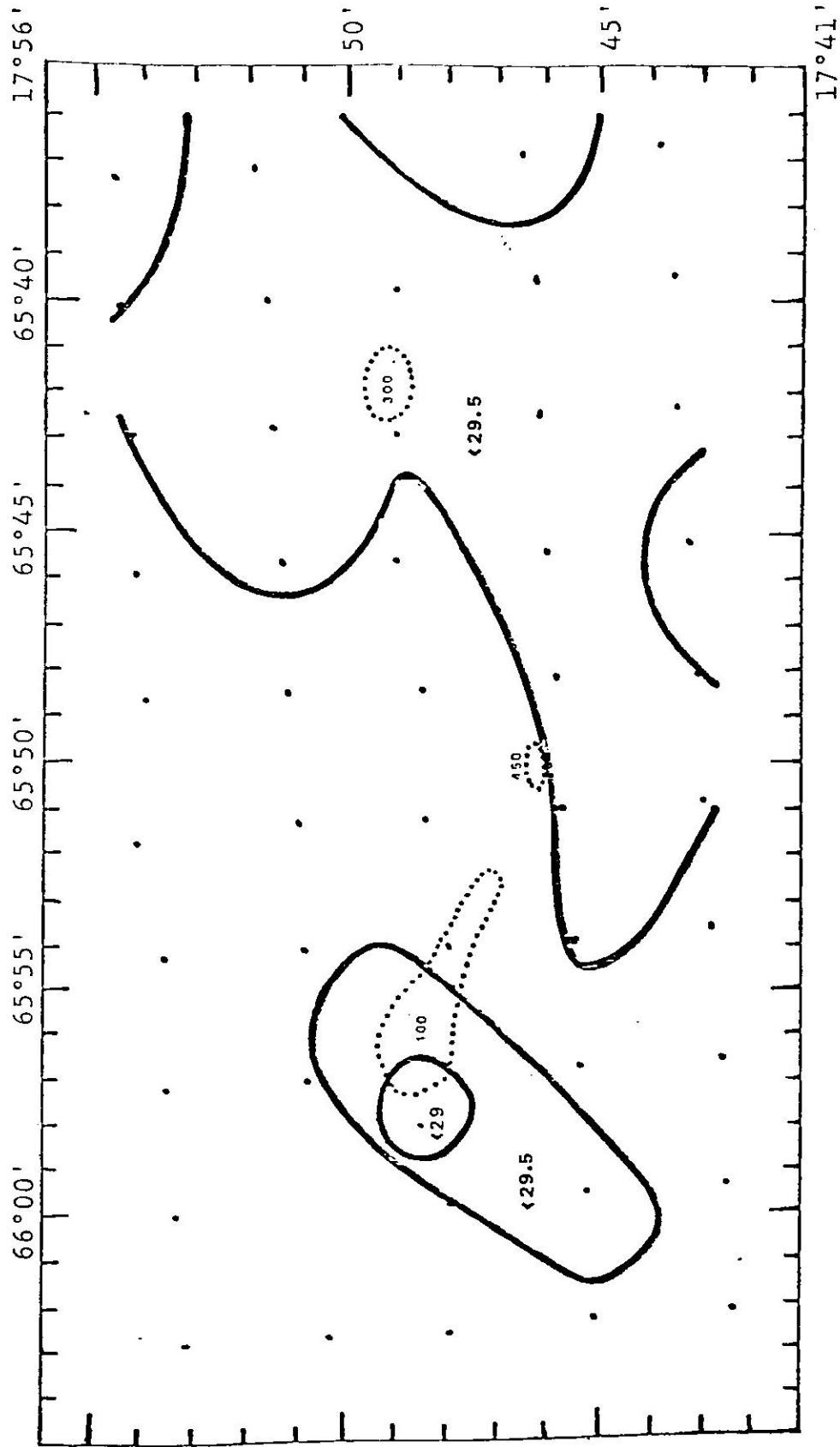
Figure 11b. Parameter contours at the surface: XBT temperature (°C).
95% F_c = 8.58, 90% F_c = 5.15, f_{sept} = 1.53, f_{nov} = 1.78.
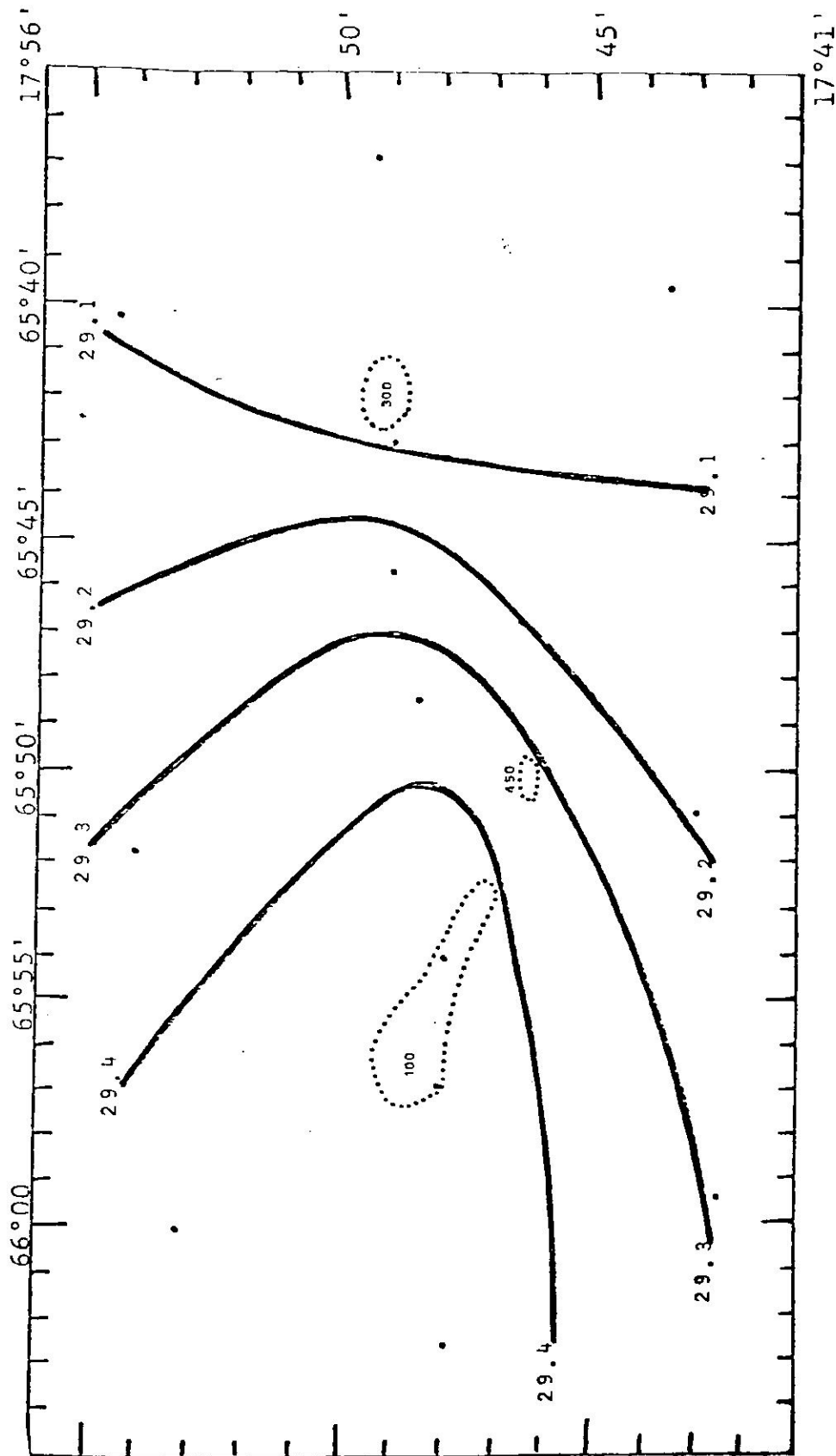
Figure 11c.   Parameter contours at the surface: hydrocast temperature (°C).
95% F_c = 8.74, 90% F_c = 5.22, f_{sept} = 1.25, f_{nov} = 1.42.

42
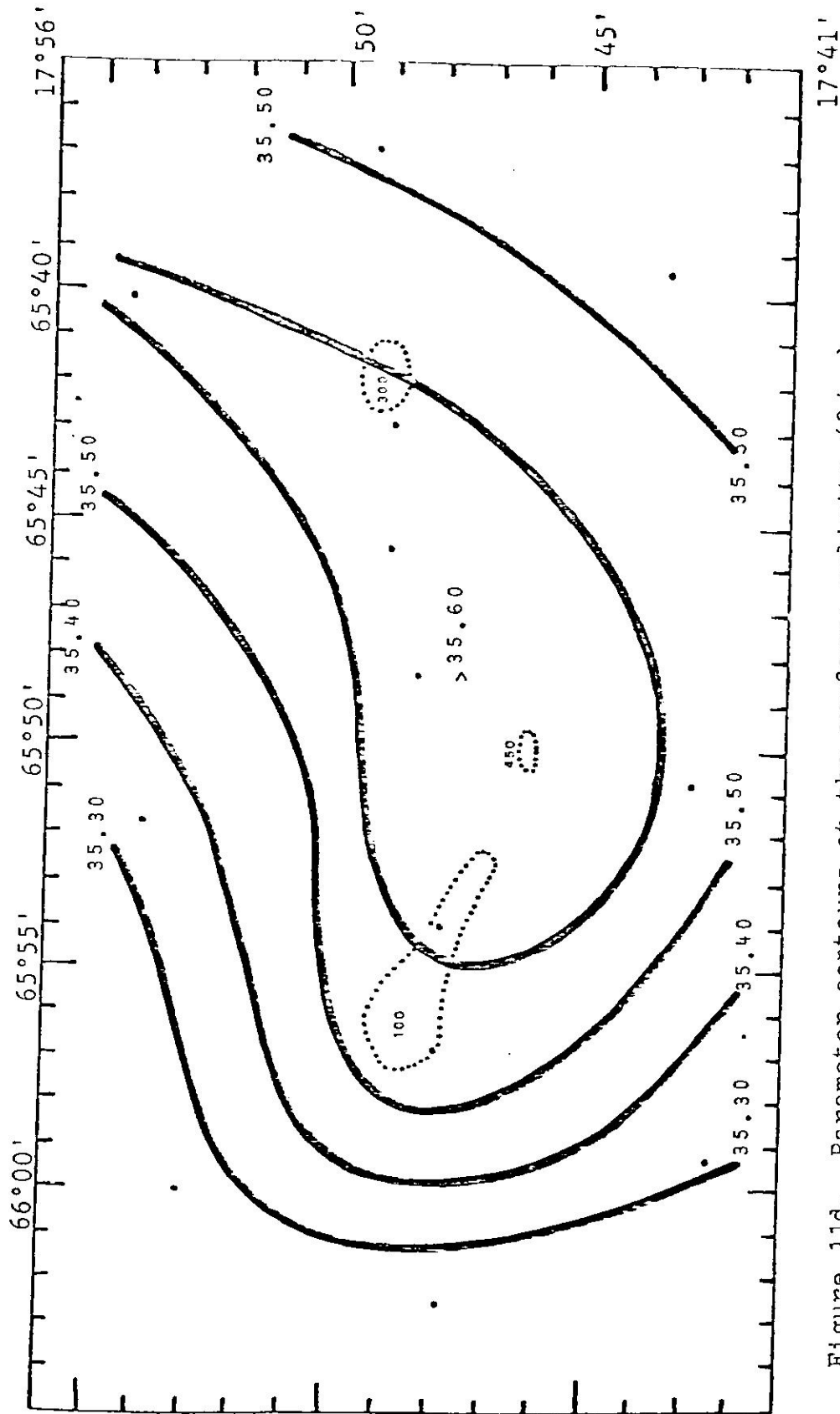
Figure 11d. Parameter contours at the surface: salinity ($^o/_{oo}$).
95% F_c = 8.74, 90% F_c = 5.22, f_{sept} = 5.11, f_{nov} = 54.9.
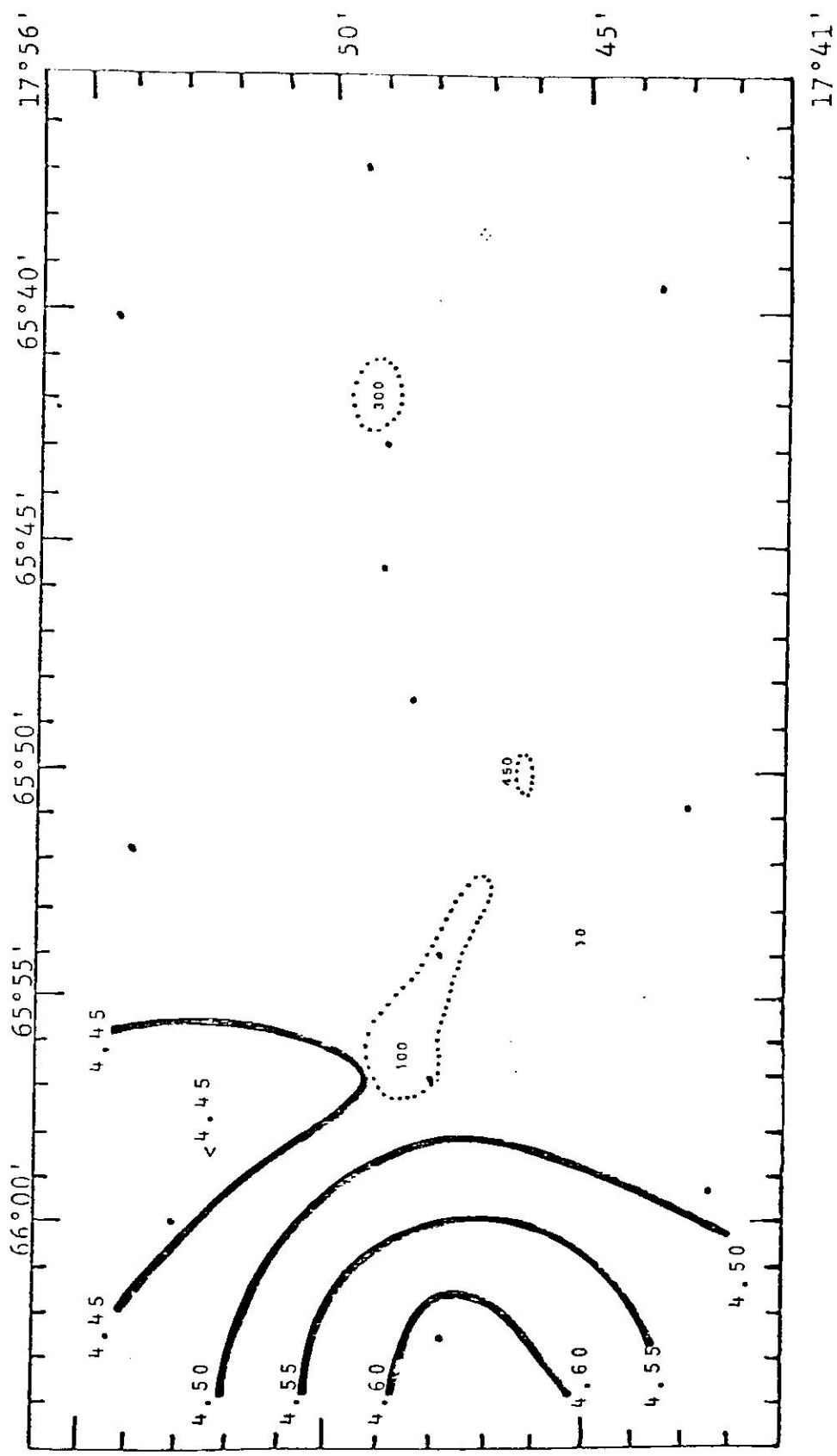
Figure 11e. Parameter contours at the surface: Dissolved oxygen (ml/L). 95% F_c = 8.74, 90% F_c = 5.22, f_{sept} = 4.88, f_{nov} = 19.5.
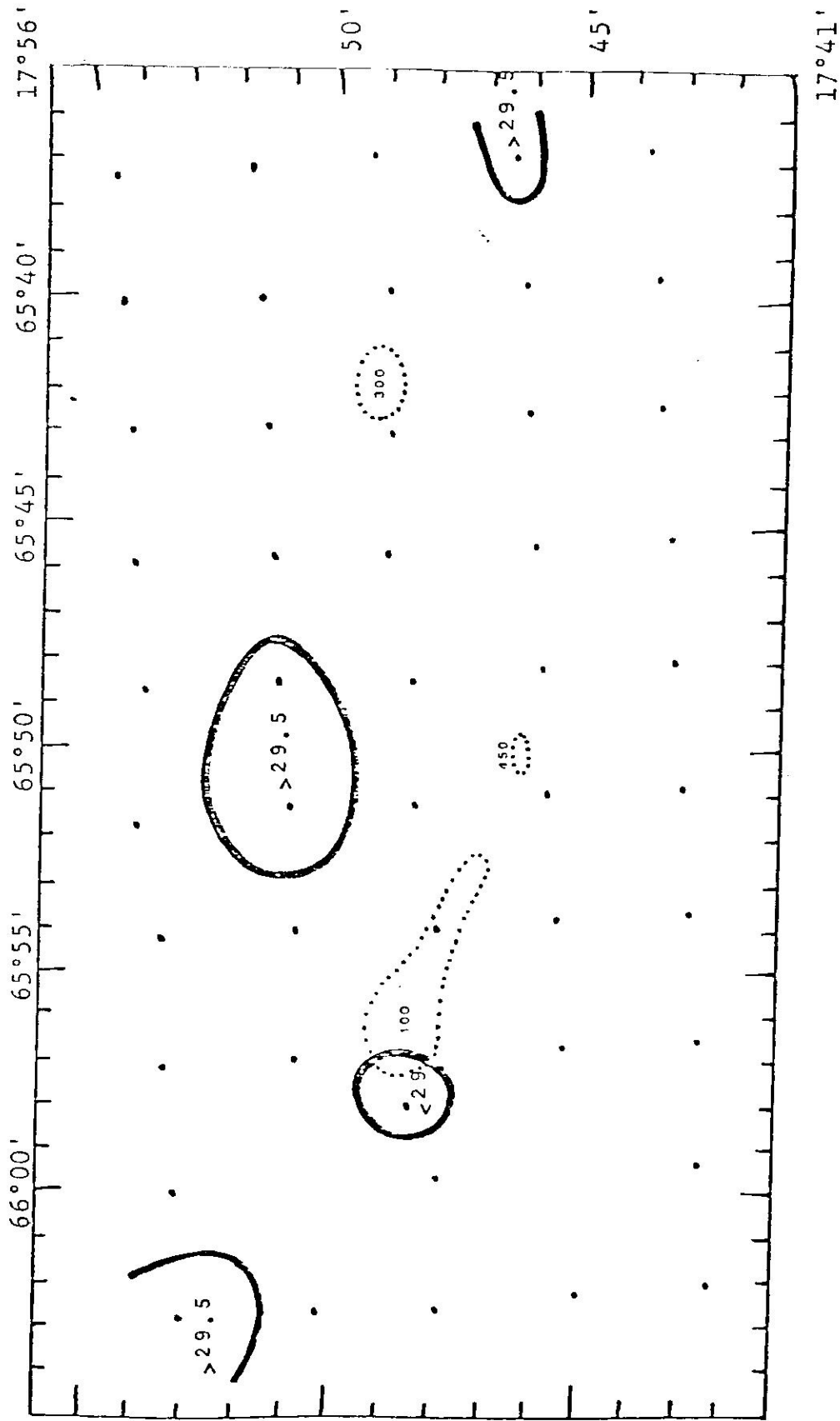
Figure 12a. Parameter contours at a depth of 20m: XBT temperature (°C).
95% F_c = 8.58, 90% F_c = 5.15, F_c = 4.67, f_{sept} = 4.67, f_{nov} = 3.50.
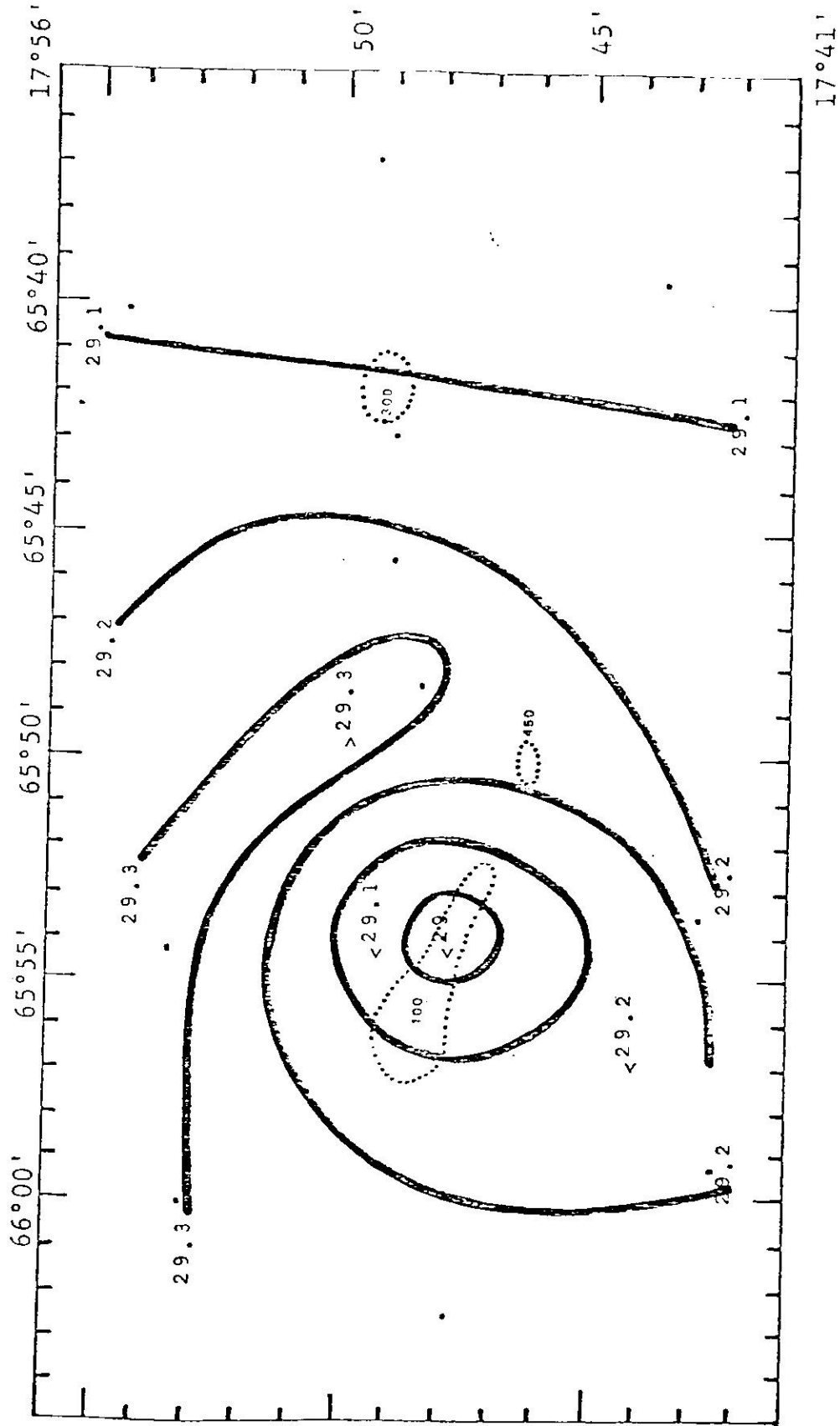
Figure 12b. Parameter contours at a depth of 20m: hydrocast temperature (°C).
95% F_c = 8.74, 90% F_c = 5.22, f_{sept} = 17.1, f_{nov} = 9.61.
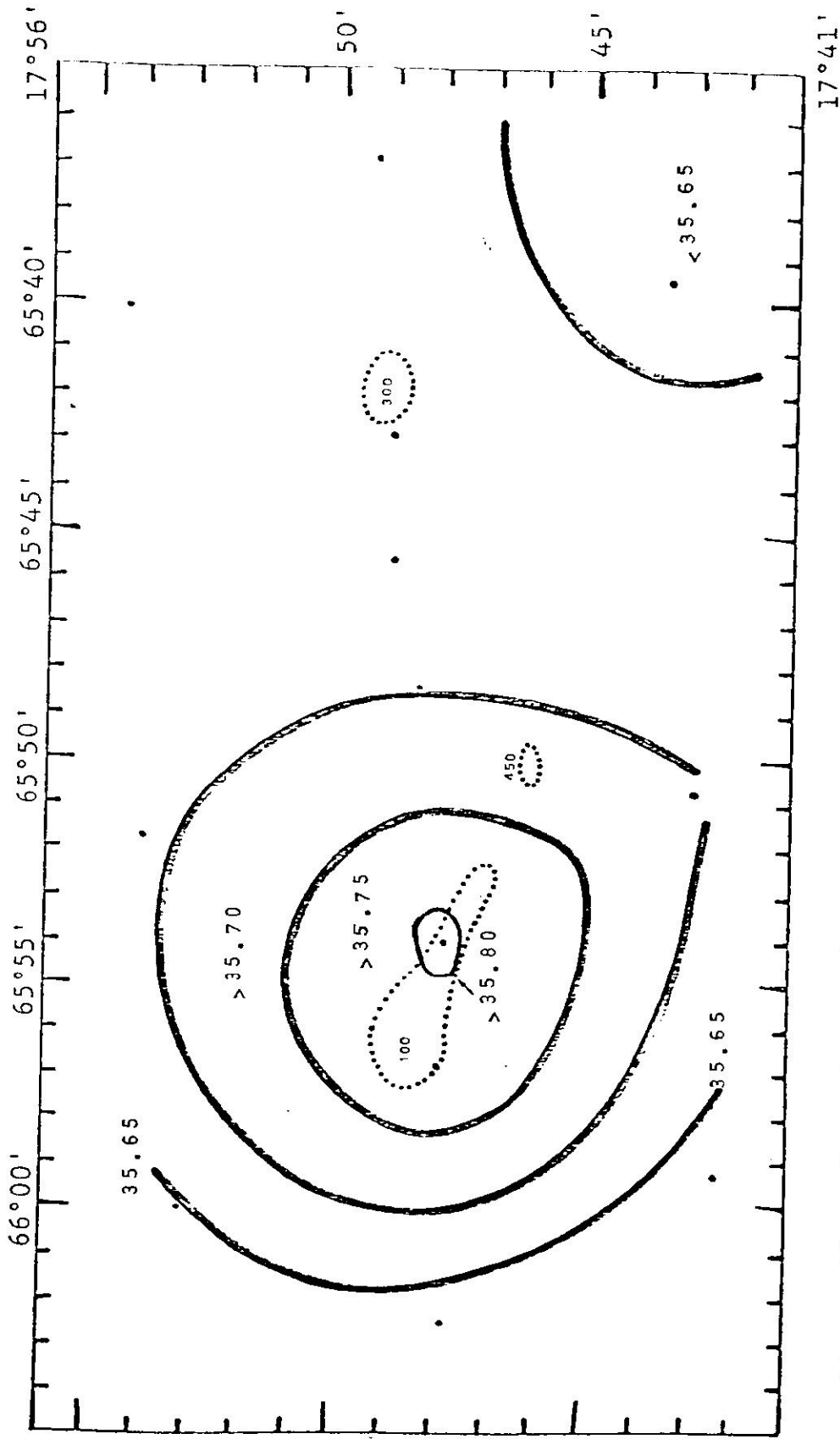
Figure 12c. Parameter contours at a depth of 20m: salinity (°/oo).
95% F_c = 8.74, 90% F_c = 5.22, f_{sept} = 3.28, f_{nov} = 4.67.
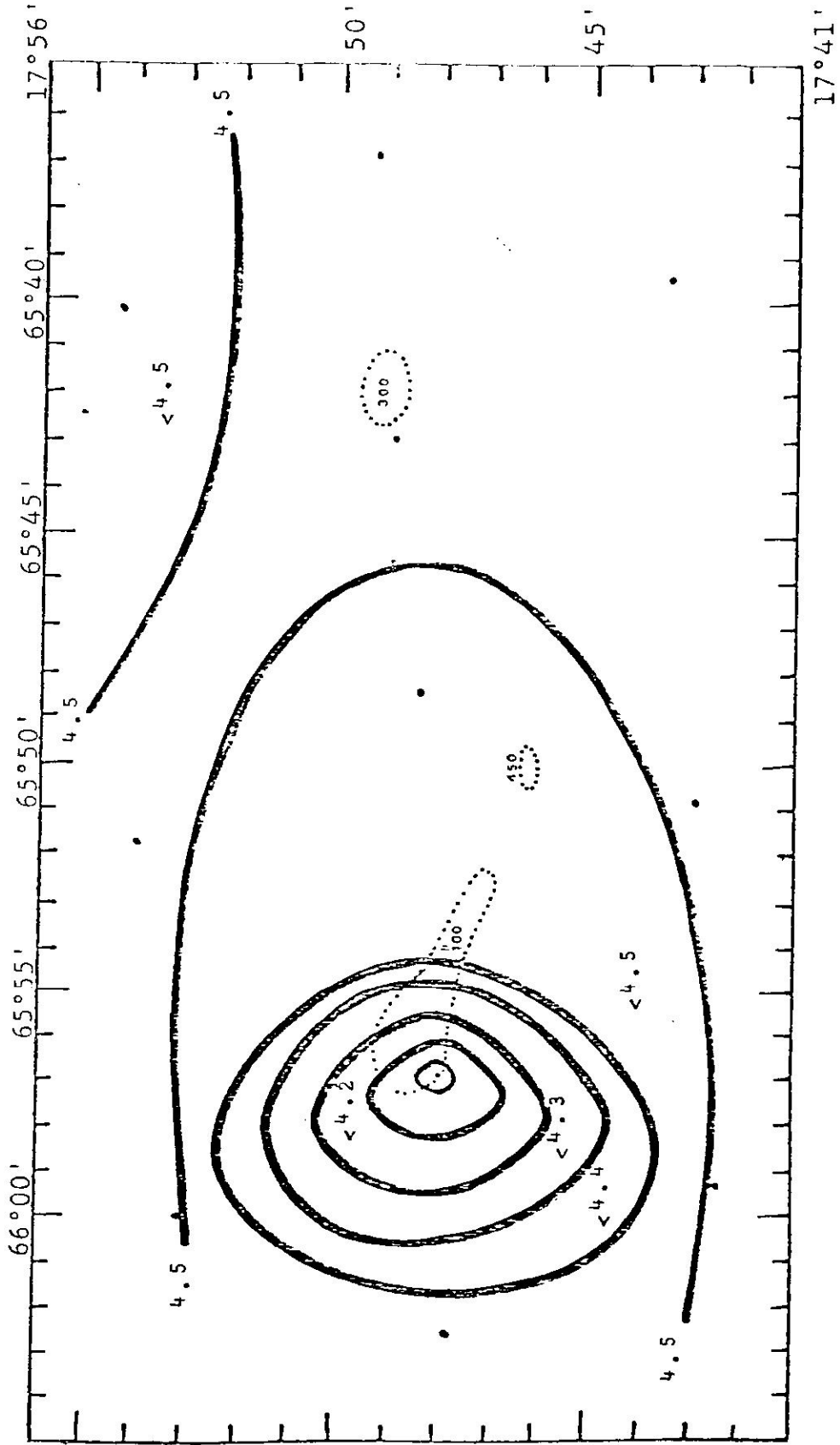
Figure 12d.   Parameter contours at a depth of 20m: dissolved oxygen. (ml/L).
95% F_c = 8.74, 90% F_c = 5.22, f_{sept} = 52.7, f_{nov} = 210.4.

48
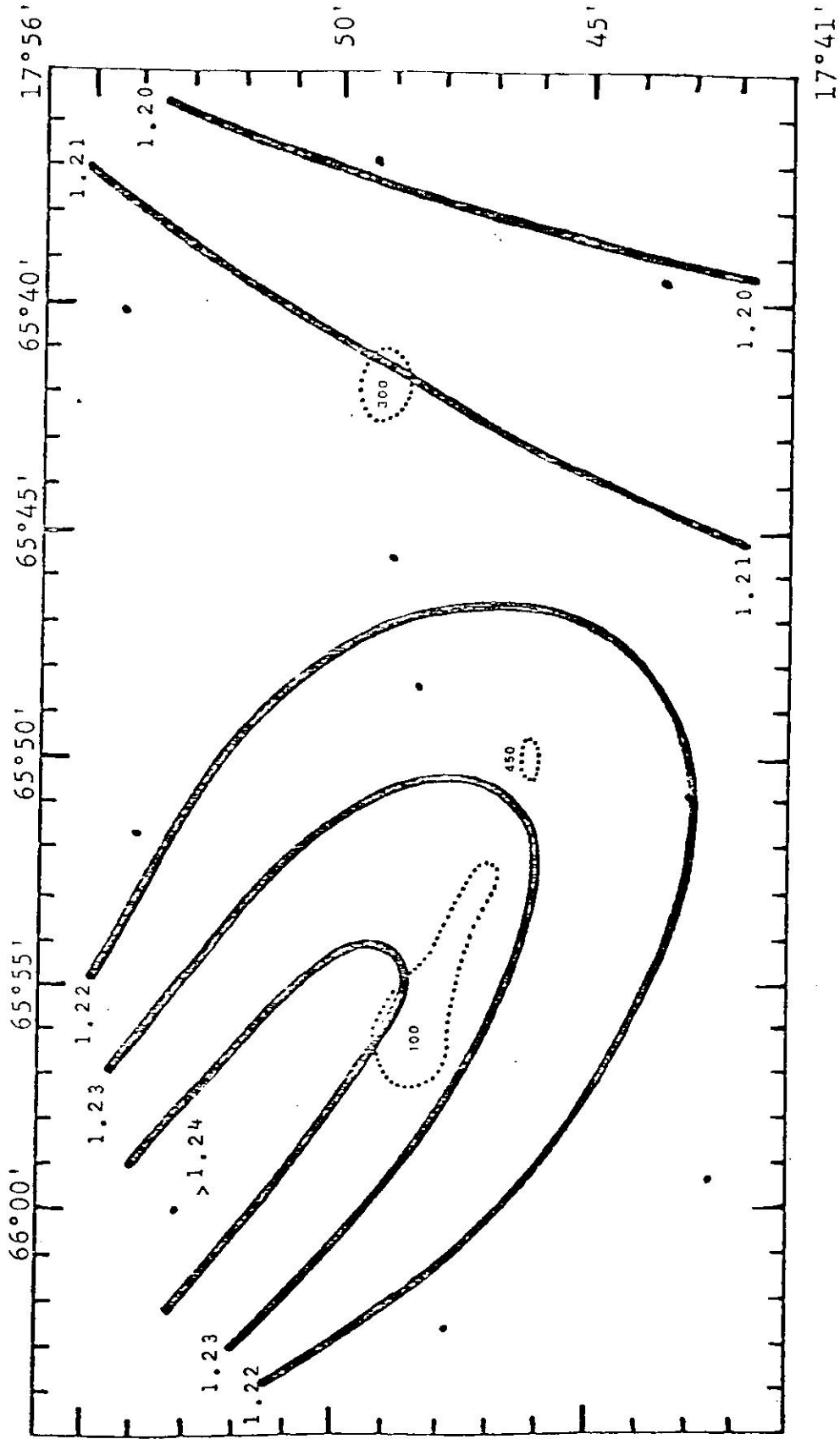
Figure 13a. Parameter contours at a depth of 50m: dynamic height. 95% $F_c = 8.79$, 90% $F_c = 5.23$, $f_{sept} = 1.48$, $f_{nov} = 1.24$.
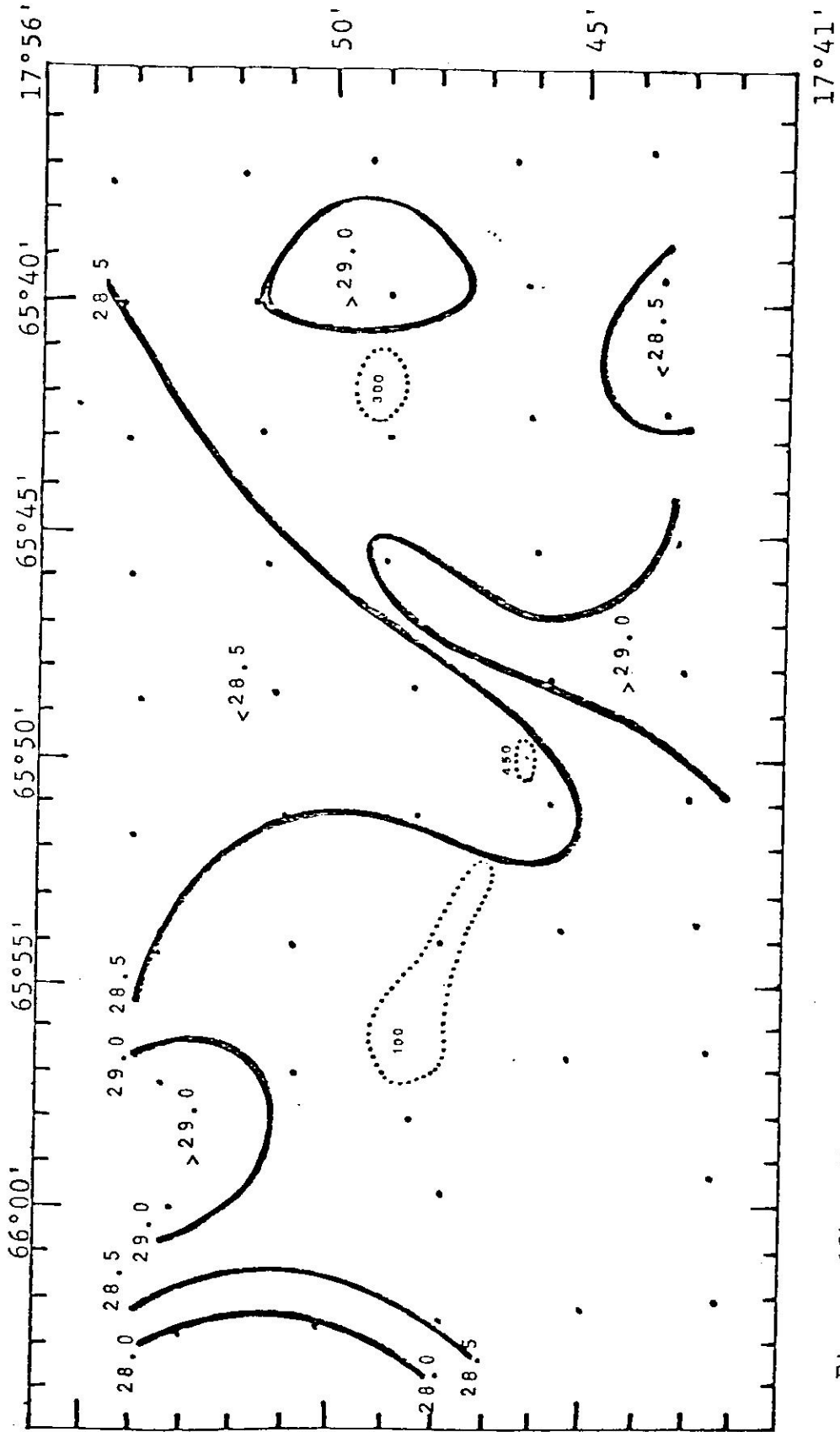
Figure 13b. Parameter contours at a depth of 50m: XBT temperature (°C).
95% F_c = 8.79, 90% F_c = 5.23, f_{sept} = 1.48, f_{nov} = 1.24.
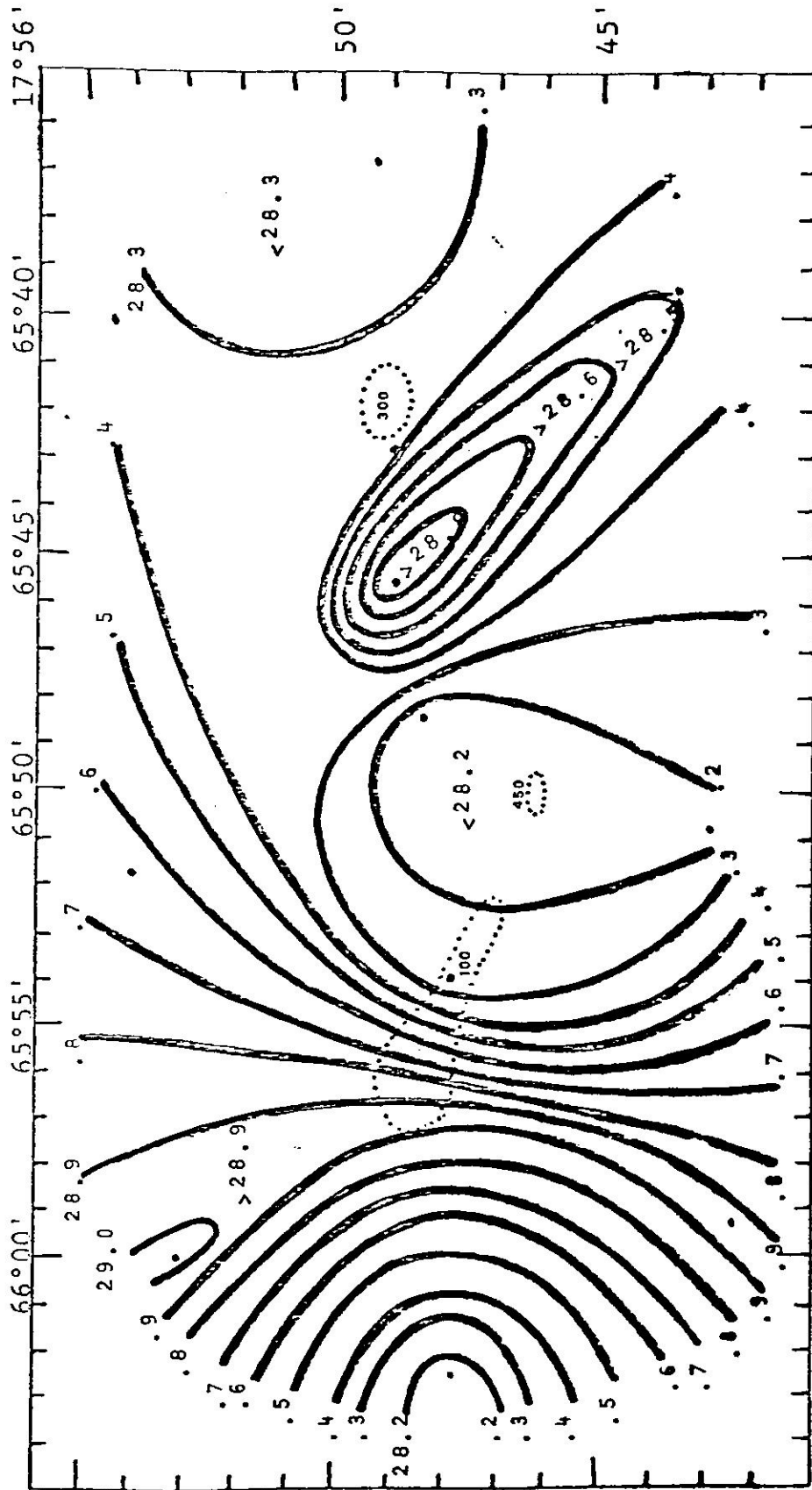
Figure 13c. Parameter contours at a depth of 50m: hydrocast temperature (°C).
95% F_c = 8.74, 90% F_c = 5.22, f_{sept} = 0.59, f_{nov} = 2.96.

51
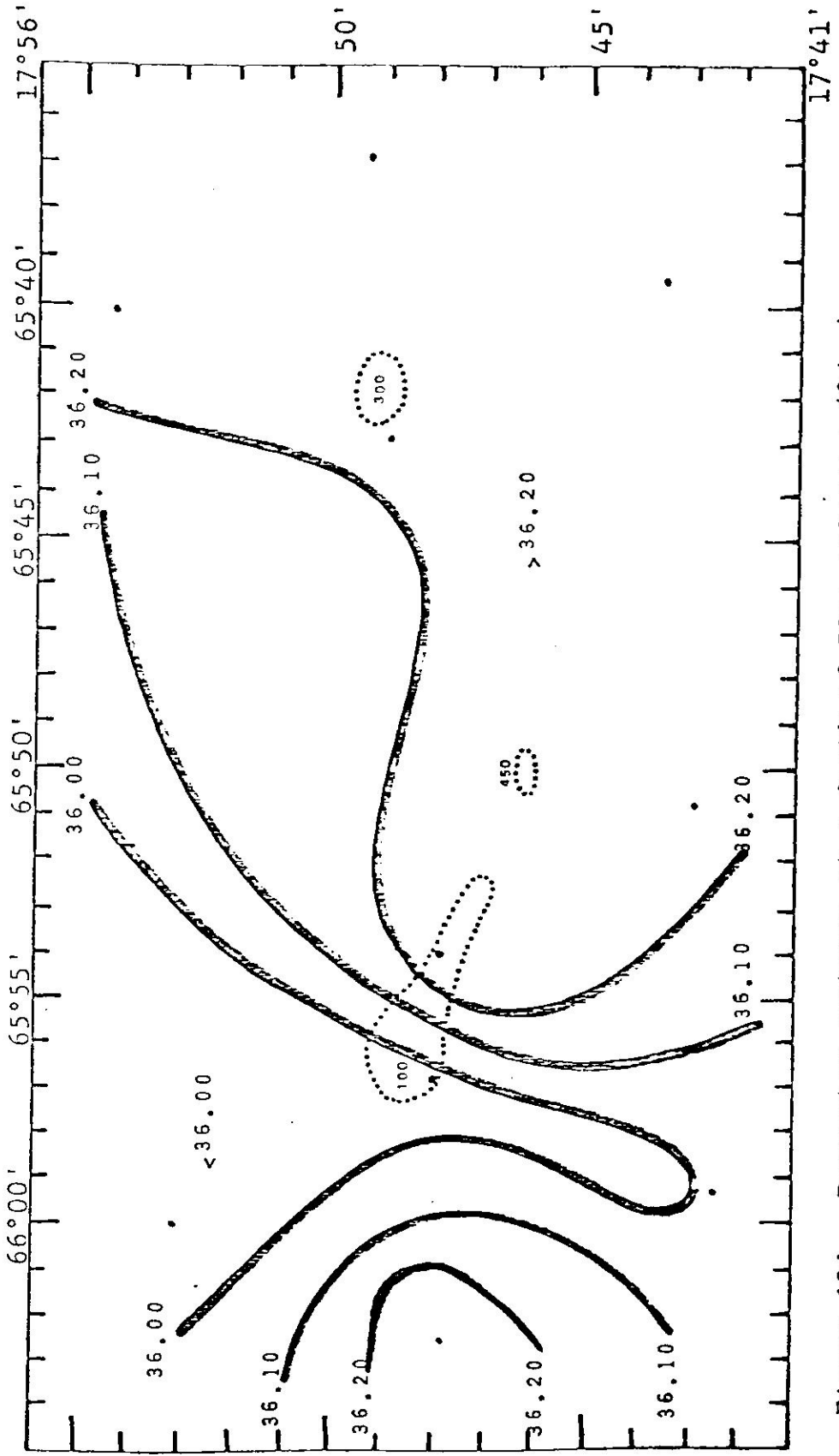
Figure 13d. Parameter contours at a depth of 50m: salinity (°/₀₀).
95% F_c = 8.74, 90% F_c = 5.22, f_{sept} = 0.98, f_{nov} = 5.90.
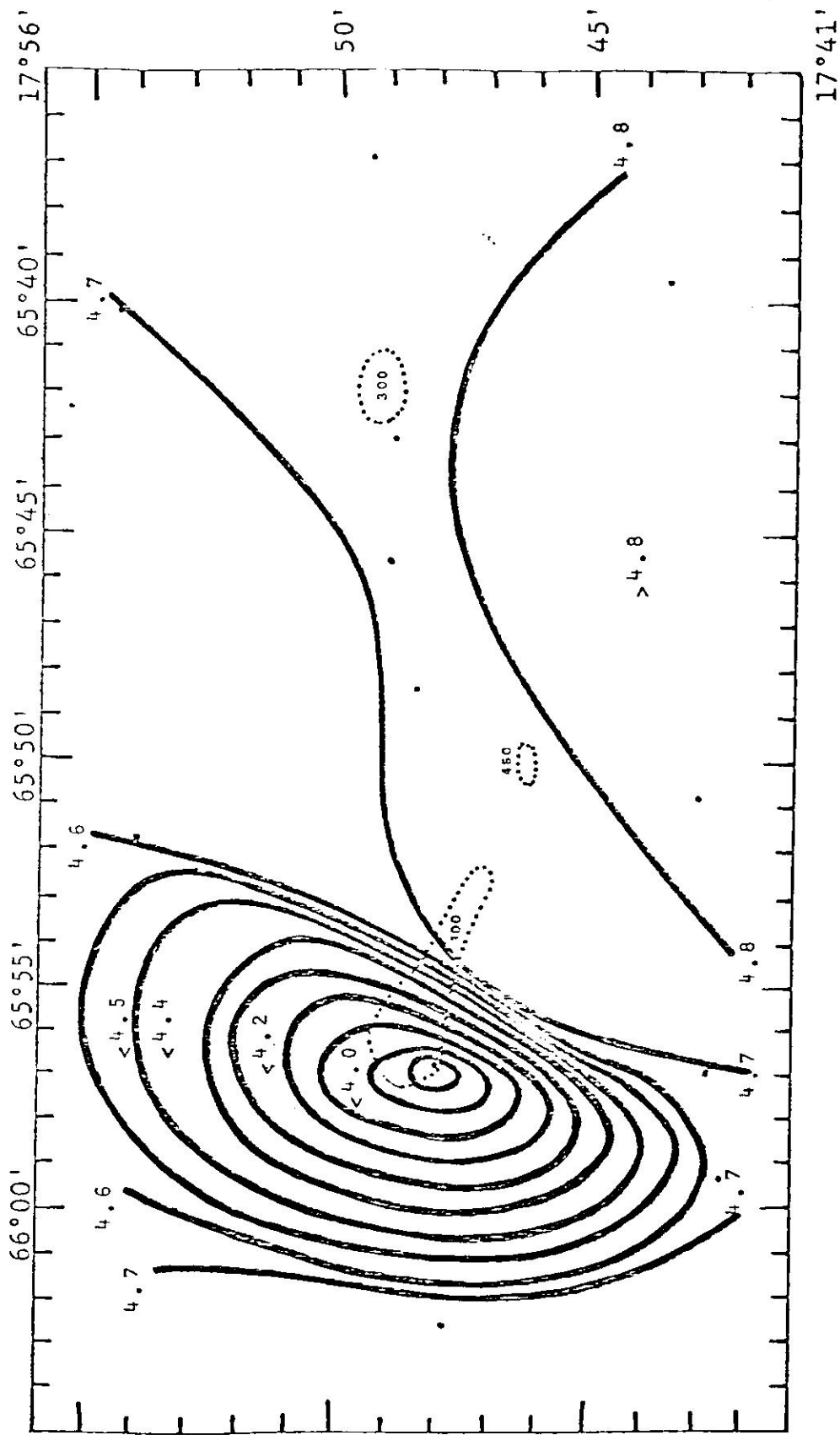
Figure 13e.   Parameter contours at a depth of 50m; dissolved oxygen (ml/L).
95% F_c = 8.74, 90% F_c = 5.22, f_{sept} = 207.4, f_{nov} = 23.0.

53

a)

b)
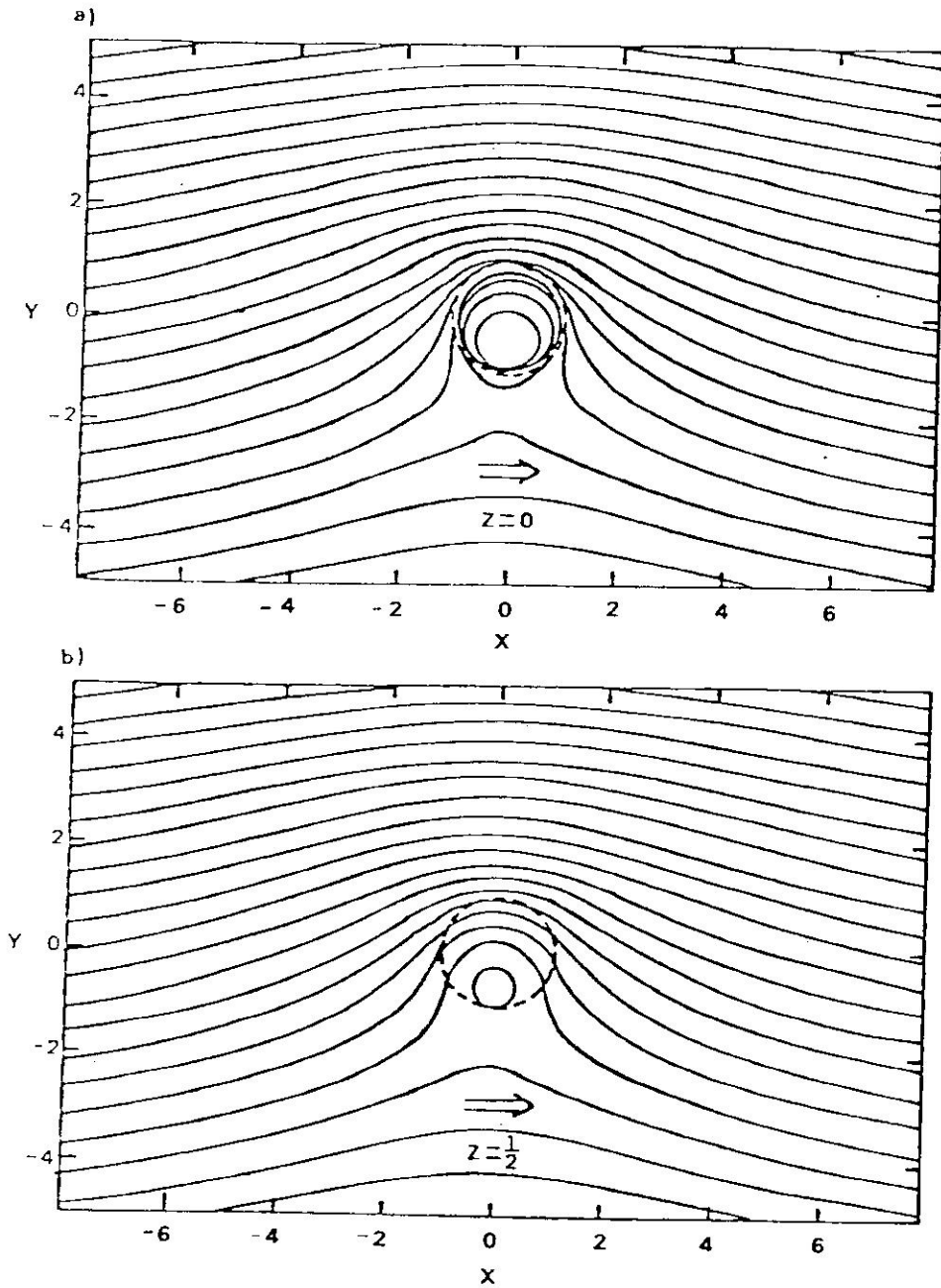
Figure 14a and 14b. For explanation see
Figure 14c.
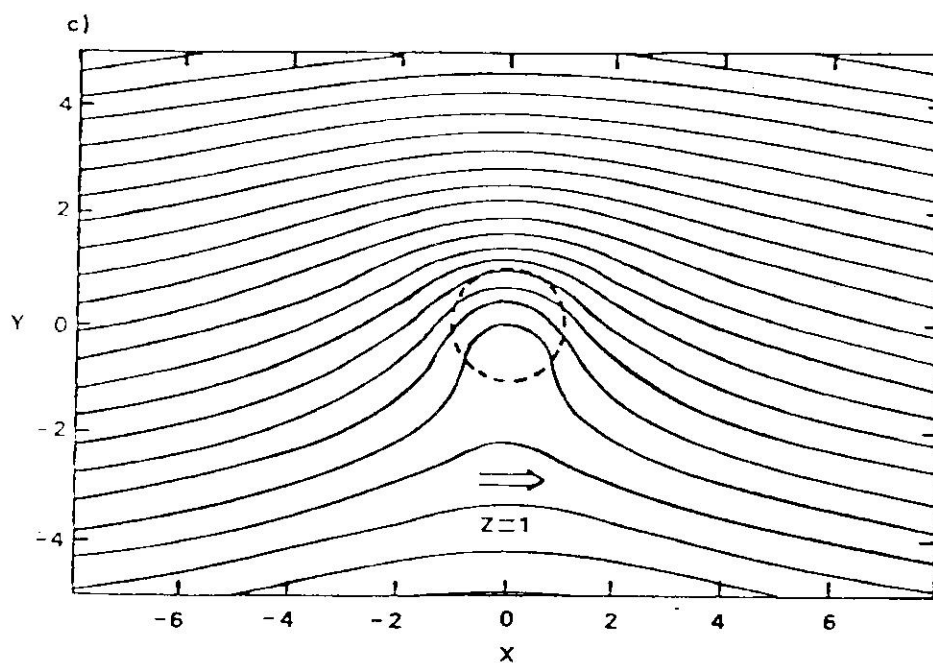
Figure 14c. Streamline plot for U' o(z)= 1, B=3 and S=1 at: a) at the obstacle's level, b) half way to the surface, and c) at the surface (from Hogg, 1973).

explained as due to the uplifting of deeper water to the top of the seamount by the oncoming flow (Huppert and Bryan, 1976). Mean upward vertical displacements of the isotherms and isohalines, calculated from the typical depth profiles, are a 5m elevation at a depth of 20m (Figures 12c and 12d) and a 2m elevation at a depth of 50m (Figures 13c and 13d). Although the vertical displacements are expected to decrease with height above the obstacle the presence of a strong thermocline (and pycnocline) at a depth of 50m could possibly account for this anomalous behaviour. An accompanying down-welling of water from the top of the sea-mount is expected to produce a warm eddy in its lee which is either trapped or shed during the initiation process. Relative vorticity generated by these processes accounts for the cyclonic (warm eddy) and anticyclonic (cold eddy) nature of these perturbations (Huppert and Bryan, 1976).

This perturbation on top of Grappler Seamount is qualitatively similar to other cold, dense features found associated with other seamounts in the New England Sea-mount Chain, in the recirculating region of the Gulf Stream (Huppert and Bryan, 1976; Owens and Hogg, 1980; Vastano and Warren, 1976); in the Emperor Seamount Chain, in the Kuroshio Extension region (Roden et al., 1982); in the North Pacific (Royer, 1978); and in the Norwegian shelf (Eide, 1979). These findings at other seamounts have been interpreted mainly in terms of Taylor column theory,

although other possibilities have been explored (Eide, 1979). Cyclonic and articyclonic motions have been observed in the vicinity of seamounts thru the use of Lagrangian drifters (Richardson, 1981; Schmitz, 1981) and current meter measurements (Owens and Hogg, 1980). An association between the cold region on top of the seamount and the anticyclonic motion was definitively established (Owens and Hogg, 1980).

Table II shows the values for the critical parameters in Hogg (1973), Huppert (1975) and Huppert and Bryan, 1976 obtained from the site specific data. The theoretical predictions from these models, based upon the values in Table II, are: 1) a perturbation (Taylor Cone or anti-cyclonic eddy) will be formed over both Grappler and Whiting Seamounts at flow speeds of less than 15 cm/s, 2) the upward vertical extent (fL/N) of these dynamic features will be in the order of 75 to 90m for Grappler Seamount and 38 to 45m for Whiting Seamount. This limited vertical extent of the Taylor Cone is due to the high fluid stratification at the study site rather than to seamount configurations, and 3) the warm eddy which forms in as-sociation to the main cold eddy (or Taylor Cone) is always shed downstream from the seamounts.

Plates 1 to 3 show what seems to be a cyclonic eddy to the southwest of Grappler Seamount. Two simultaneous views taken on June 9, 1973 from the Skylab show a circular

Table IIa.   Values for the critical parameters in
             Hogg (1973).

U*o(0) =>	1	5	10	15	20
Grappler	42.3	8.4	4.2	2.5	2.1

$B=h_o f L U^*o(0)$

$HU^{**}2$

| Whiting | 18.2 | 3.6 | 1.8 | 1.2 | 0.9 |

	Surface	100 meters
Grappler	398	277

$S=(NH/fL)^{**}2$

| Whiting | 1593 | 1106 |

B=topographic parameter; S=stratification parameter;
U*o(0)=flow speed at the obstacle's level; ho= the
obstacle's height; f=Coriolis parameter; L=obstacle's
length scale; H=total water depth; N=Brunt-Vaisala
frequency; U=root mean square speed integrated over the
entire fluid depth.

(See Appendix B for computational details.)

Table IIb. Values for the critical parameters in
Huppert (1975).

V =>	1	5	10	15	20
Grappler	42.3	8.4	4.2	2.8	2.1
ho/R					
Whiting	18.2	3.6	1.8	1.2	0.9

	Surface	100 meters
Grappler	20.0 (75)	15.5 (90)
B=NH/fL (fL/N)		
Whiting	39.9 (38)	31.0 (45)

ho=scaled obstacle's height (maximum); R=Rossby number;
N=Brunt-Vaisala frequency; L=obstacle's length scale;
H=total water depth; f=Coriolis parameter; V=upstream speed
(See Appendix B for computational details.)

Table IIc.   Values for the critical parameter Nh_m/U_o in Huppert and Bryan (1976).

	U_o =>	1	5	10	15	20
Grappler	Surface	8.4	1.7	0.8	0.6	0.4
	100 meters	7.0	1.4	0.7	0.5	0.4
Whiting	Surface	7.2	1.4	0.7	0.5	0.4
	100 meters	6.0	1.2	0.6	0.4	0.3

U_o=upstream speed; h_m=maximum obstacle height;
N=Brunt-Vaisala frequency

(See Appendix B for computational details.)

Plate 1.   Skylab image of the seamount
           region showing an eddy-like
           feature in the vicinity of
           Grappler Seamount.
           June 9, 1973a; B&W 0.5-0.6um.

Plate 2. Skylab image of the seamount
          region showing an eddy-like
          feature in the vicinity of
          Grappler Seamount.
          June 9, 1973a; B&W 0.6-0.7um.
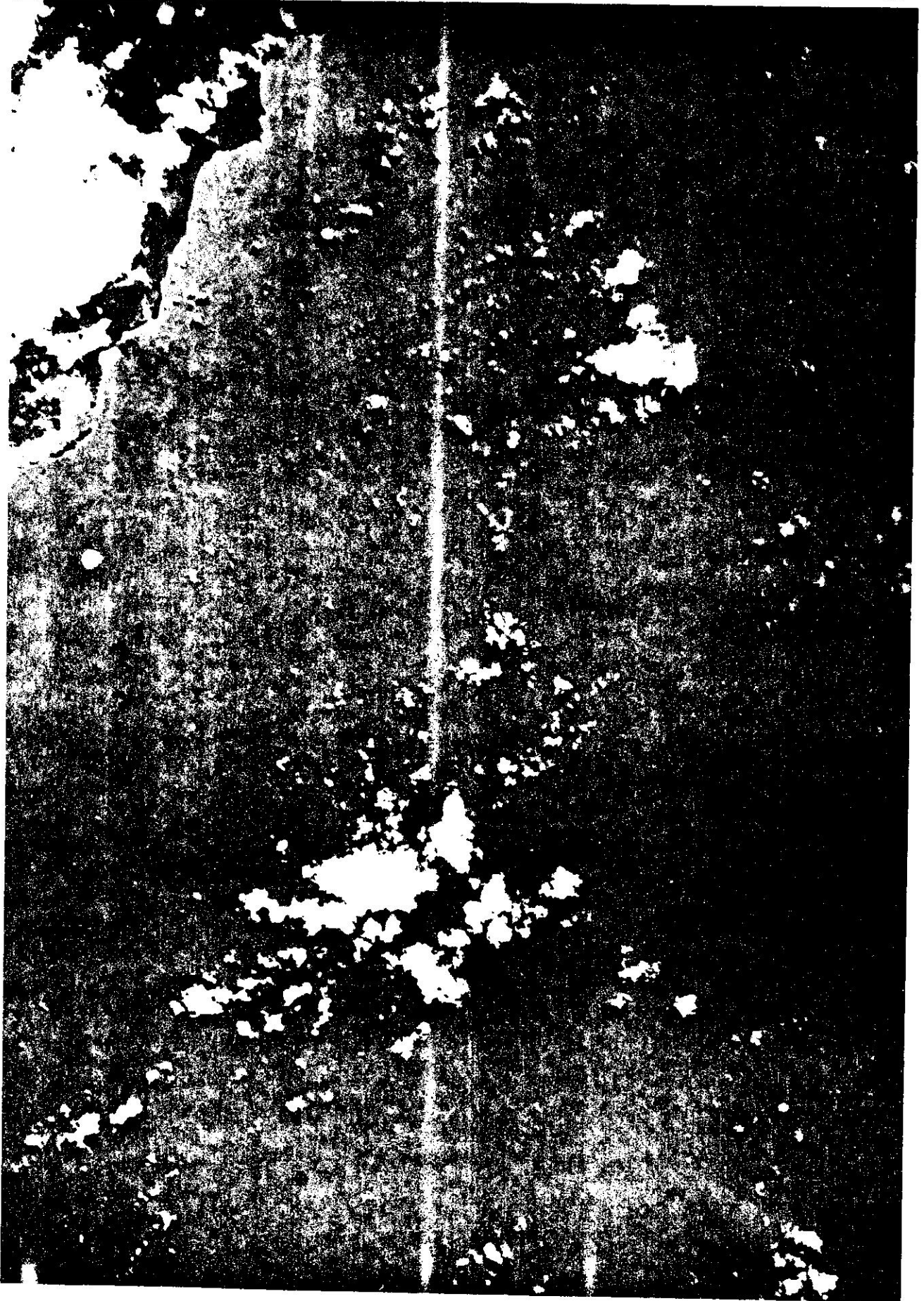
Plate 3.   Skylab image of the seamount
region showing an eddy-like
feature in the vicinity of
Grappler Seamount.
June 9, 1973b; B&W 0.5-0.6um.

feature (eddy?) with a diameter of 14km (7km radius) located 20km to the southwest of Grappler Seamount (Figure 15). Its length scale (radius) is roughly similar to Grappler's radius, at mid-elevation. This same feature appears in all versions of the same scenes (photographed by a multispectral camera array) described in the Appendix C (color (0.4 to 0.7 um), color infrared (0.5 to 0.88 um) and two frequencies in black and white (0.5 to 0.6 um and 0.6 to 0.7 um; Plates 1 to 3). Considering a typical speed of 10 cm/s, it would have taken the eddy approximately two days to drift from the vicinity of the seamount to the point where it was photographed. This was the only distinguishable feature observed in the satellite images from the seamount area. Although these photographs do not link the eddy directly to the seamounts, they are suggestive of a possible association.

Other eddies found previously, during CEER research in the area, are typically larger and do not resemble the Taylor Cone type of perturbation found on top of Grappler Seamount during the seamount survey, except for the anti-cyclonic eddy found centered near Grappler Seamount during the month of May 1980 (Figure 16). This eddy has a very similar water mass structure to the Grappler eddy and its larger size could be due to interpolations among wider spaced stations (at this scale the eddy is defined by only one station). A cyclonic eddy was also found to the west
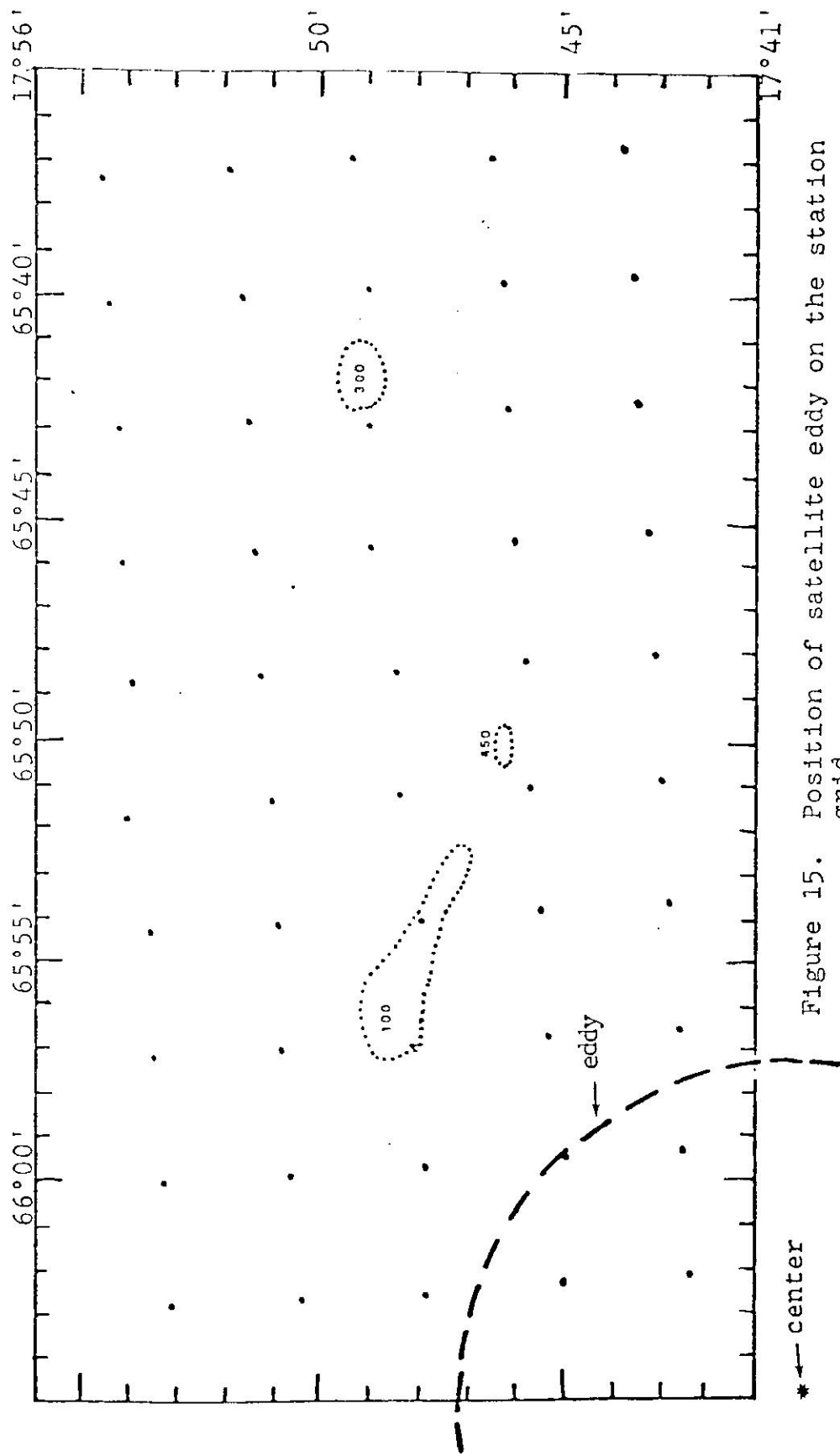
Figure 15. Position of satellite eddy on the station grid.
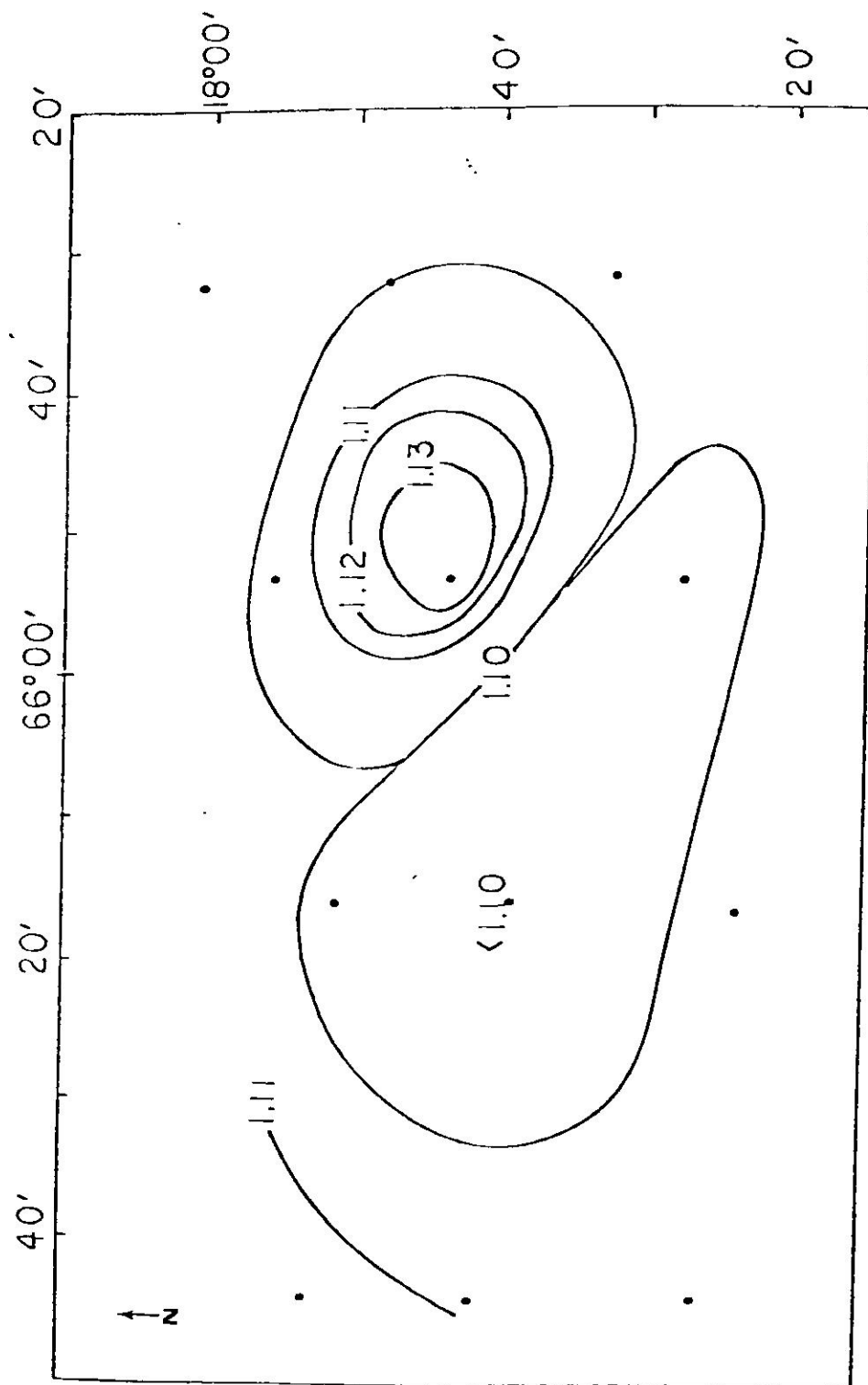
Figure 16. Dynamic height contours during the May, 1980 CEER cruise relative to the 800m reference level.

of Grappler Seamount during the May cruise which could possibly be an eddy shed from the seamount, according to Huppert and Bryan's (1976) theory. No feature was observed in satellite images synoptic with this cruise.

B. 70-150m Depth Layer

From below the top of Grappler Seamount and down to a depth of 150m the features shown in the distribution of the different parameters bear little relationship to each other and also the f-ratios are smaller (usually <1.0) than in the subsurface region. Figure 17 shows the parameter topographies at a depth of 125m. The dynamic height topography still maintains the main features described for the upper layers except for the disappearance of the dynamic high to the northeast of Grappler Seamount. Geostrophic currents decrease in speeds with mean southwest speeds of 5 to 10 cm/s and westward speeds, west of the seamount, decreasing from 32 to 10 cm/s in the depth interval from 75 to 200m (Figure 17a). Below a depth of 100m the f-ratios of the dynamic height distribution are always less than one, which means the signal is weak. The XBT temperatures show a continuation of the cold region over Grappler Seamount spreading around it. The warm region southwest of the seamount has also spread out towards the north. Temperatures are higher in the eastern half of the survey area and patches of warm water can now be observed over Whiting

68
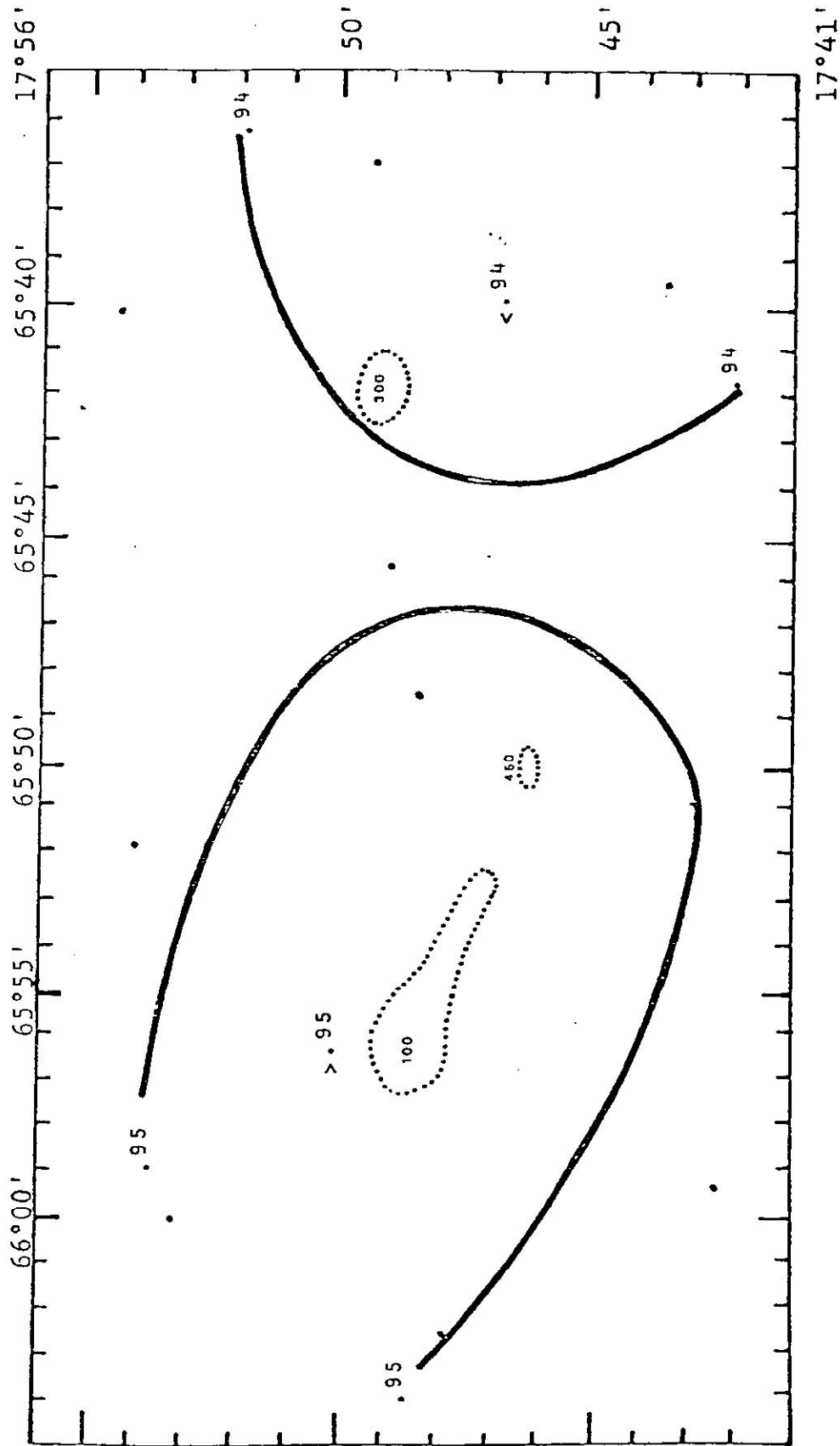
Figure 17a. Parameter contours at a depth of 125m; dynamic height. 95% F_c = 8.79, 90% F_c = 5.23, f_{sept} = 0.81, f_{nov} = 0.48.
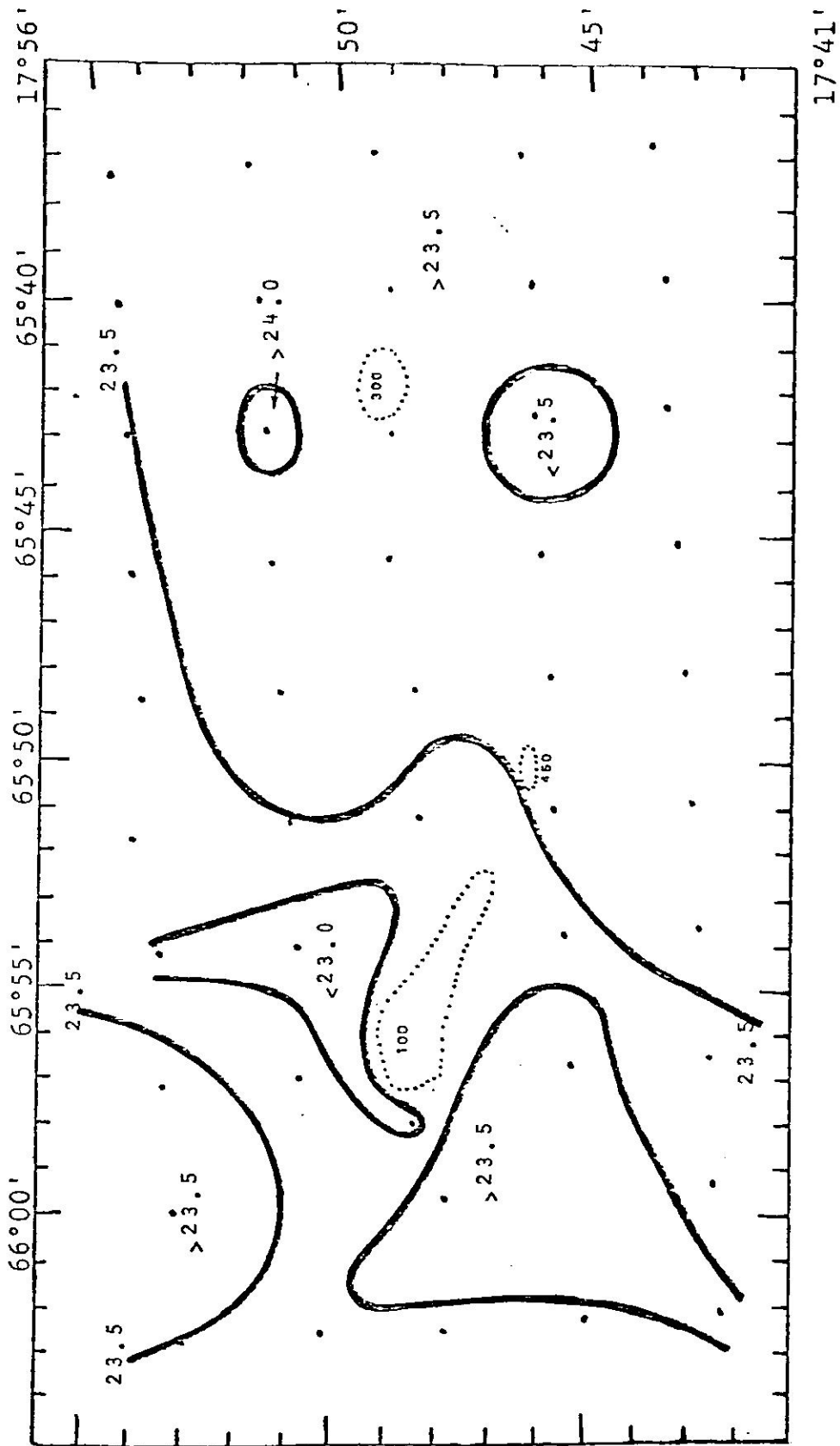
Figure 17b. Parameter contours at a depth of 125m: XBT temperature (°C).
95% F_c = 8.58, 90% F_c = 5.15, f_{sept} = 139.4, f_{nov} = 19.2.
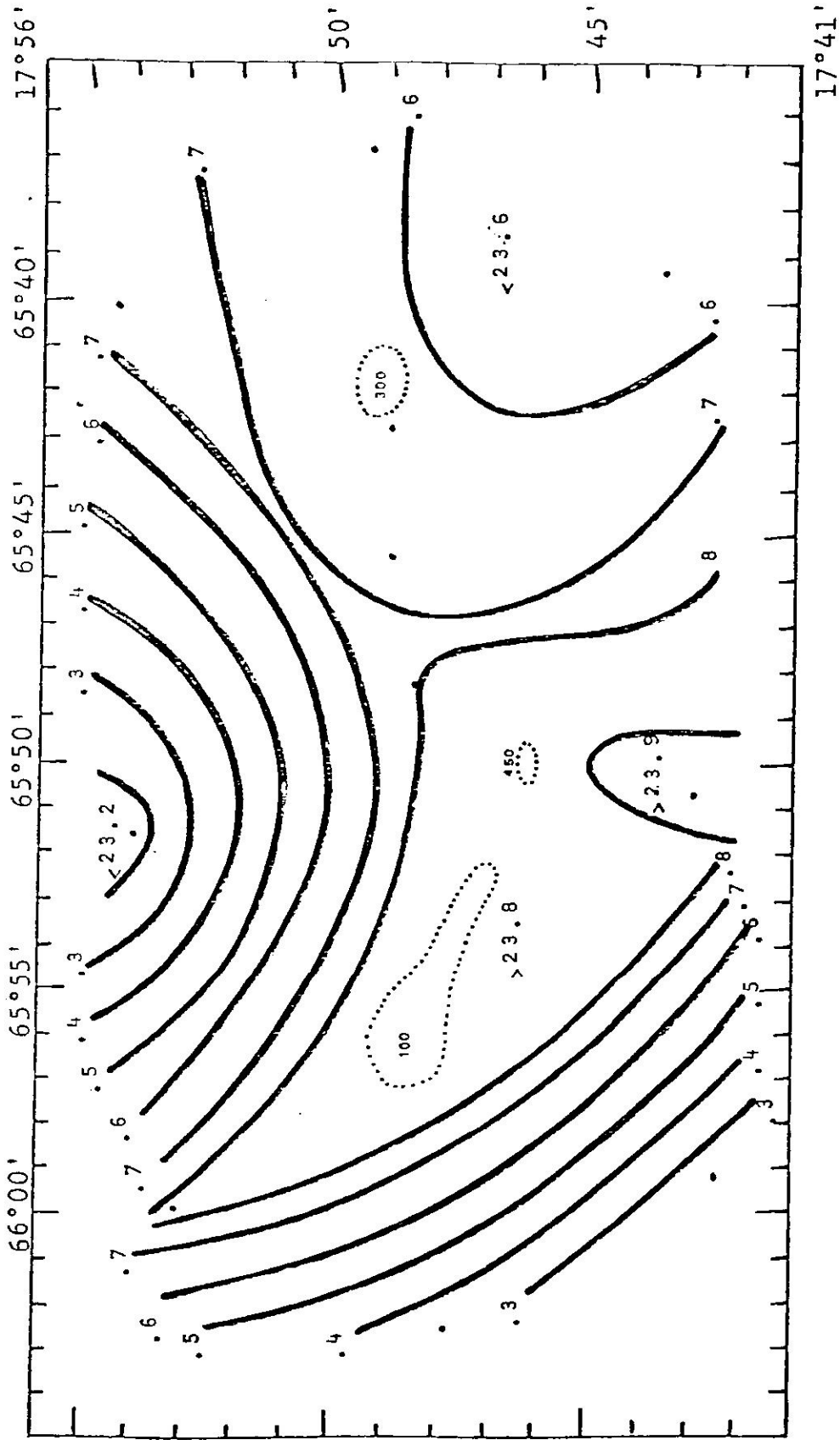
Figure 17c. Parameter contours at a depth of 125m: hydrocast temperature (°C). 95% F_c = 8.67, 90% F_c = 5.22, f_{sept} = 0.94, f_{nov} = 13.1.

70
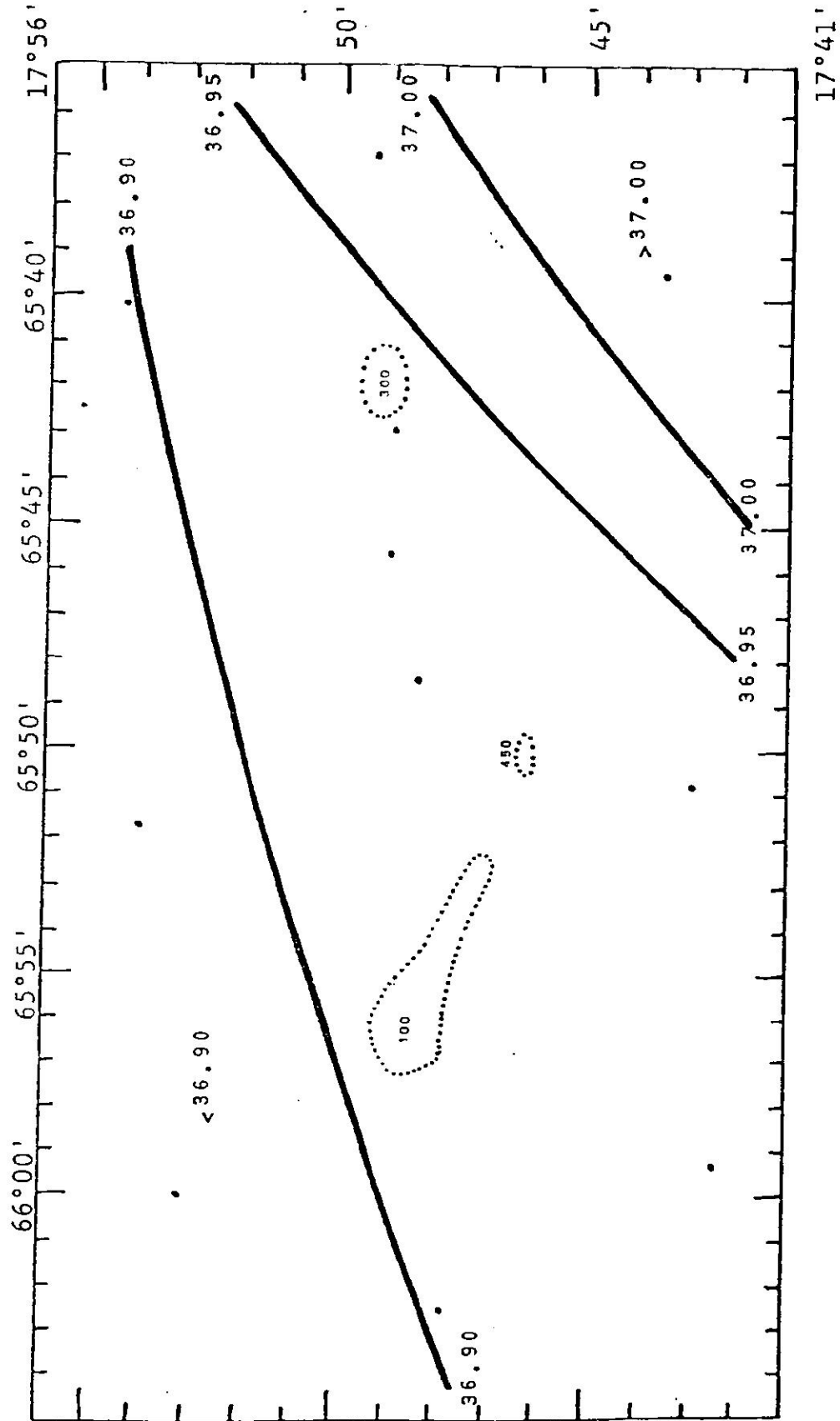
Figure 17d. Parameter contours at a depth of 125m: salinity ($^{\circ}/_{\circ\circ}$).
95% F_c = 8.76, 90% F_c = 5.22, f_{sept} = 68.0, f_{nov} = 20.2.

71
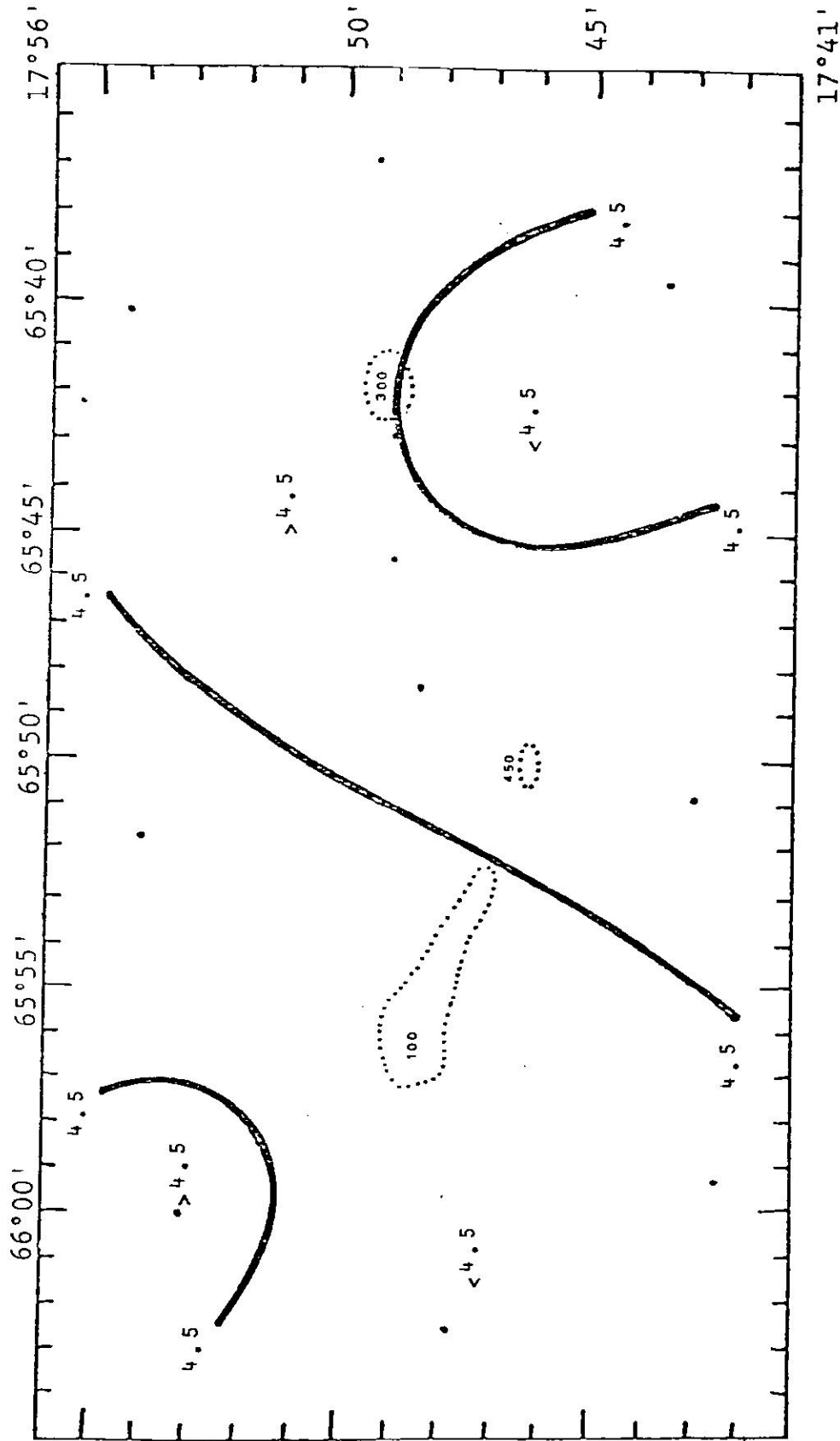
Figure 17e. Parameter contours at a depth of 125m: dissolved oxygen (ml/L).
95% F_c = 8.76, 90% F_c = 5.22, f_{sept} = 2.04, f_{nov} = 0.67.

Seamount (Figure 17b). Some of these features, specially
the east-west gradient, also show in the thermometric
temperature field (Figure 17c).

The salinity contours demonstrate a well-defined gradient
with higher salinities to the southeast decreasing towards
the west-northwest (Figure 17d). This result is consistent
with the expected circulation of the Subtropical Underwater
(SUW) water mass, although it was not expected to show so
strongly at this small sampling scale. The dissolved oxygen
distribution at this depth level, figure 17e, does not show
any organized feature although the isolines are well-aligned
with the salinity contours.

A total of seven different trajectories (paths) were
obtained from the November 10-14, 1982 drogue survey; these
are shown in figures 18 to 20. At a depth of 100m the
drifters were below the top of the seamount ($\pm$70m), whose
100m depth contour is shown in the figures. This contour
was obtained using the depth sounder on board the R/V SULTANA
during the cruise. The main aspects observed in the drifter
trajectories are: 1) the steering of the drogues around the
seamount, 2) the tendency for these trajectories to converse
downstream from the seamount, and 3) the larger average
speeds on the left side of the seamount (looking downstream),
18 cm/s average for trajectories A-1, B-1, D-1, as compared
to the right side, 8 cm/s average for trajectories A-2, D-3
(Figure 18). This difference in speeds on opposite sides
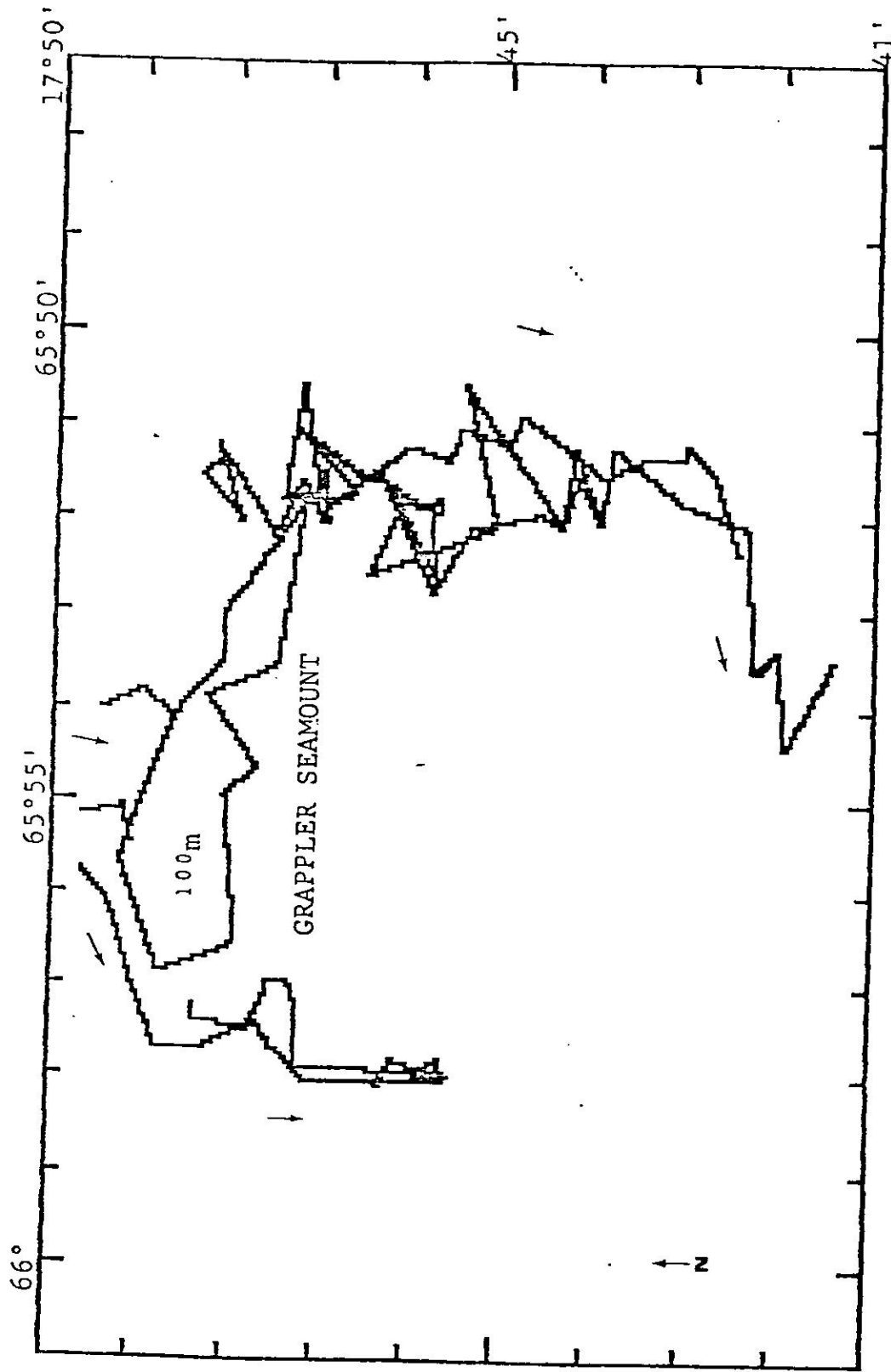
Figure 18. Drifter trajectories in the vicinity of Grappler Seamount from November 10 to 14, 1982. All (7) trajectories are shown. Drifters were drogued at a depth of 100m.
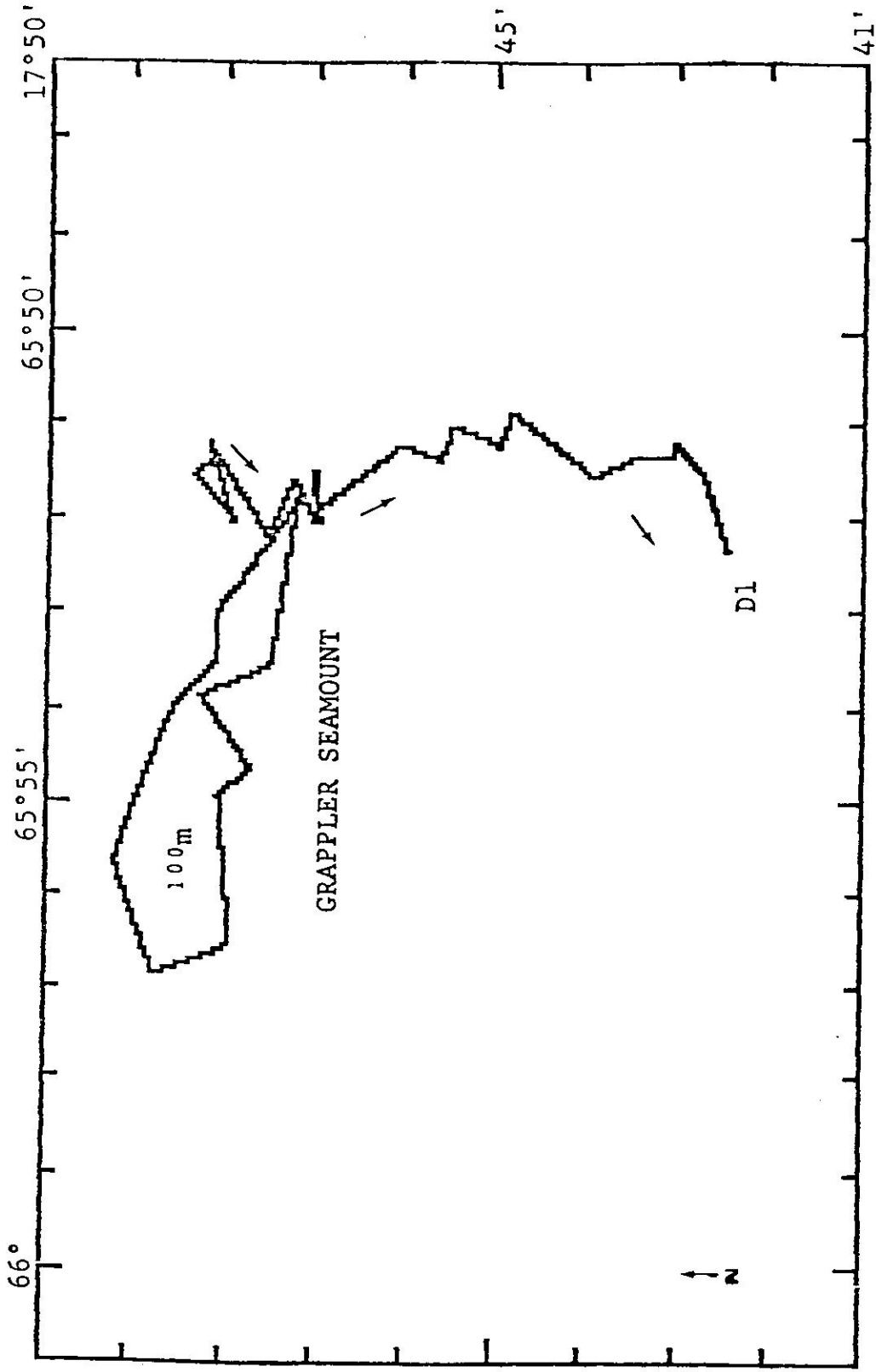
Figure 19. Trajectory of drifter D-1, typical trajectory around the eastern margin of Grappler Seamount (November 10-12, 1982).
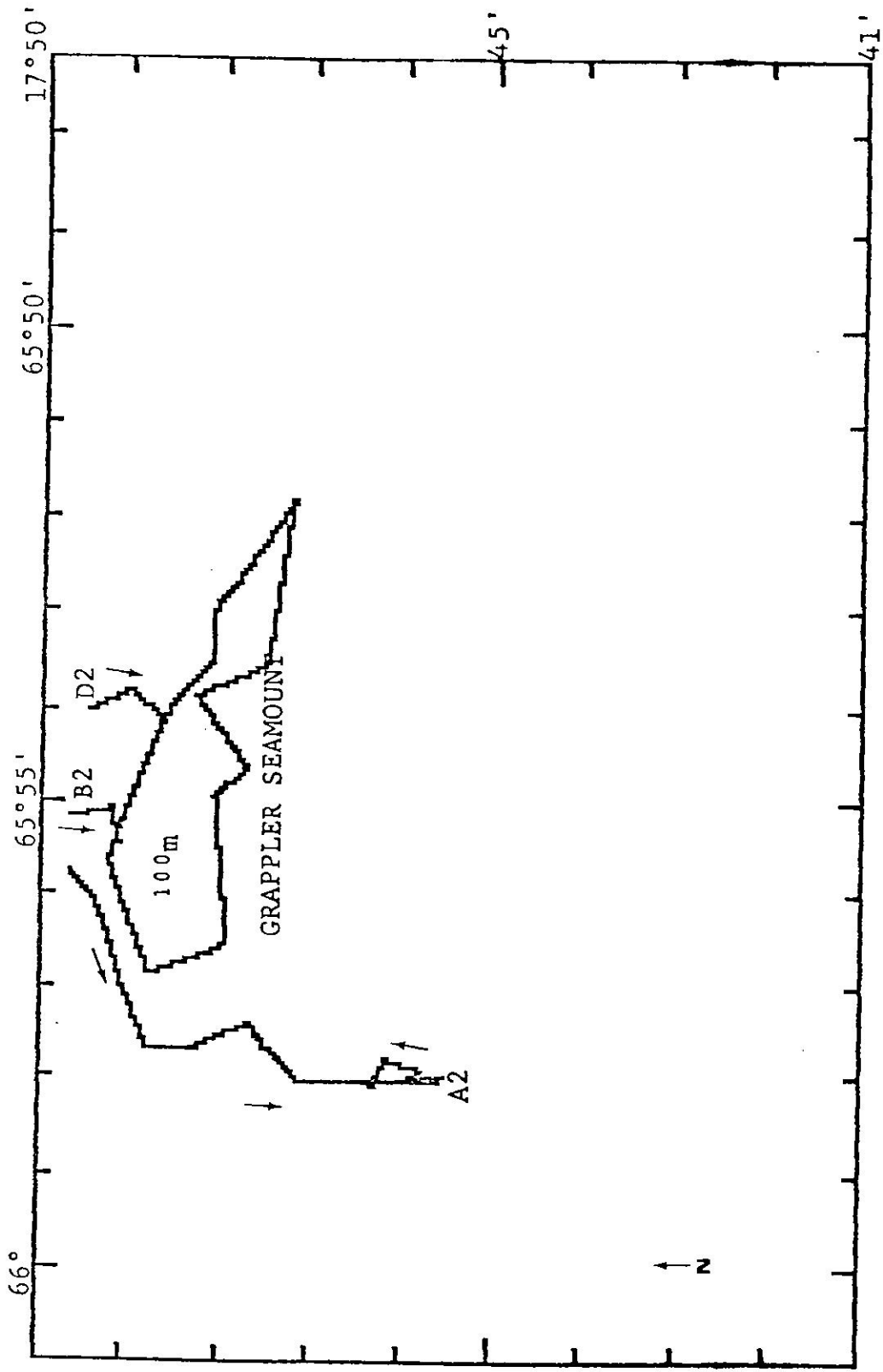
Figure 20. Trajectories of drifters A-2, B-2 and D-2 (November 12-14, 1982).

76

of Grappler Seamount indicates a tendency for anticyclonic motion, which may occur under the appropriate flow conditions as predicted by Huppert (1975) and Huppert and Bryan (1976). The grounding of drifters B-2 and D-2 may imply the presence of a vertical motion (upwelling) in that region to which the drogues could not respond.

C. 200-300m Depth Layer

The top of Whiting Seamount lies at a depth of 218m and the parameter topographies in this depth interval are dominated by closed contour areas of high salinity, high temperature and low D.O. in the vicinity of the seamount as shown in figures 21b to 21e. The f-ratios are generally higher in this region than in the regions above and below it. Although the dynamic height signal is very weak, geostrophic currents maintain the same distribution as in the upper layers, but the speeds have increased to around 10 cm/s in this depth interval (Figure 21a). This speed increase is hard to explain and might be related to the motion of the Sargasso Sea Water (SSW) or to thermal wind effects.

The well-organized salinity gradient has disappeared and low salinity patches are now found (Figure 21d). At a depth of 250m the waters upstream from Whiting Seamount are less saline and colder, while downstream they are saltier and warmer (Figures 21c and 21d). This distribution is
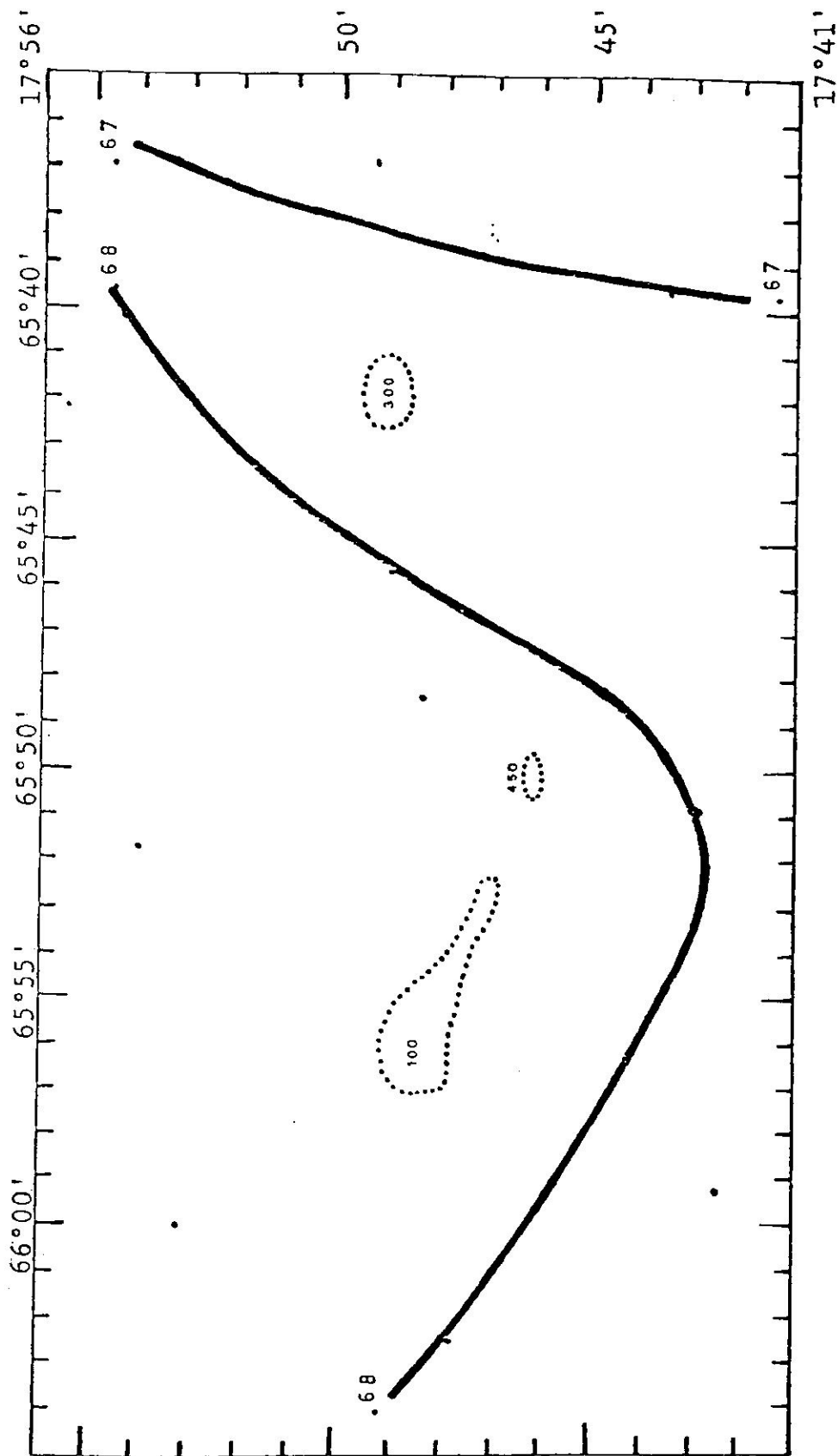
Figure 21a. Parameter contours at a depth of 250m: dynamic height.
95% F_c = 8.79, 90% F_c = 5.23, f_{sept} = 0.34, f_{nov} = 0.49.
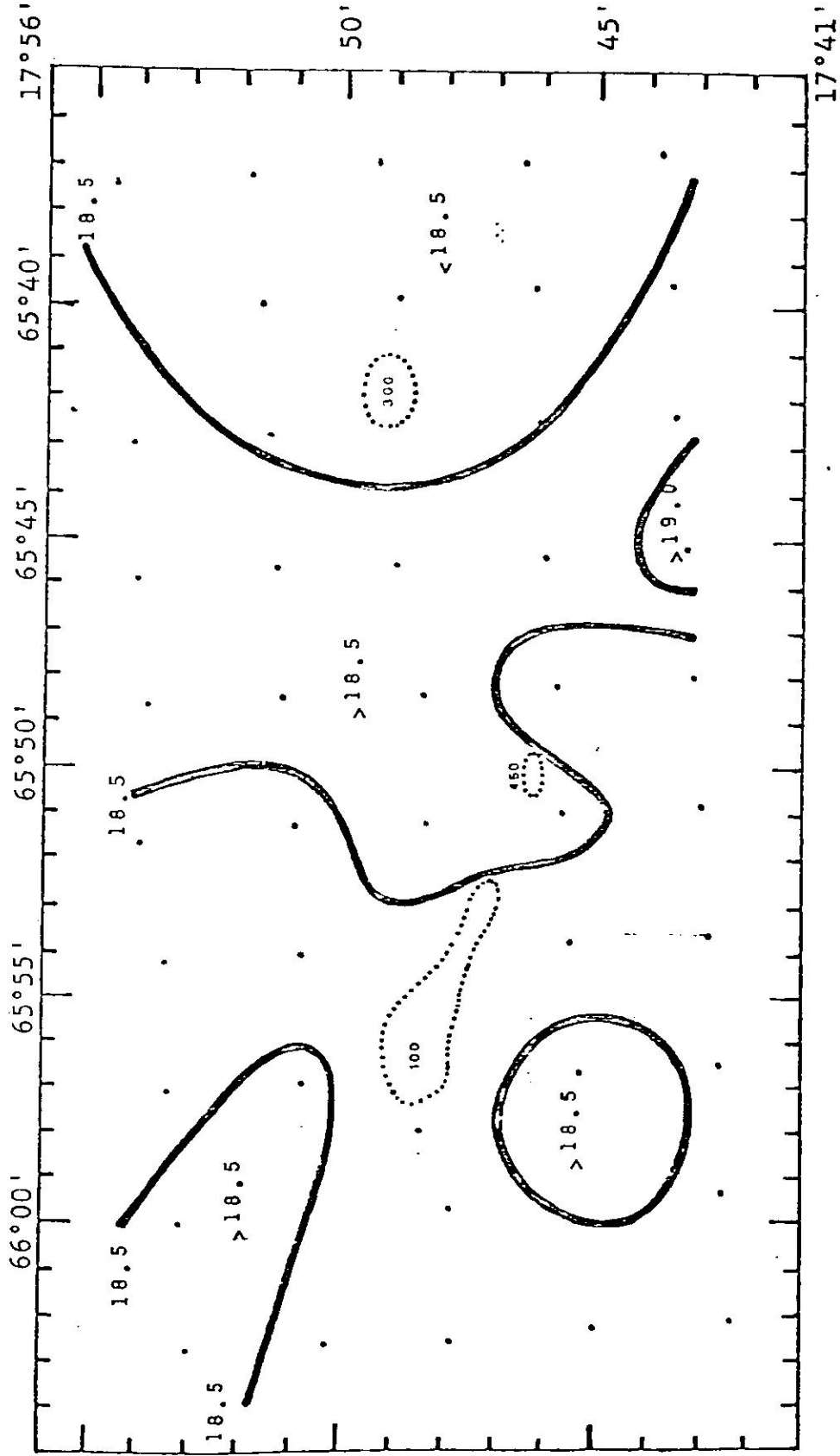
Figure 21b. Parameter contours at a depth of 250m: XBT temperature (°C). 95% F_c = 8.58, 90% F_c = 5.16, f_{sept} = 2.44, f_{nov} = 1.93.
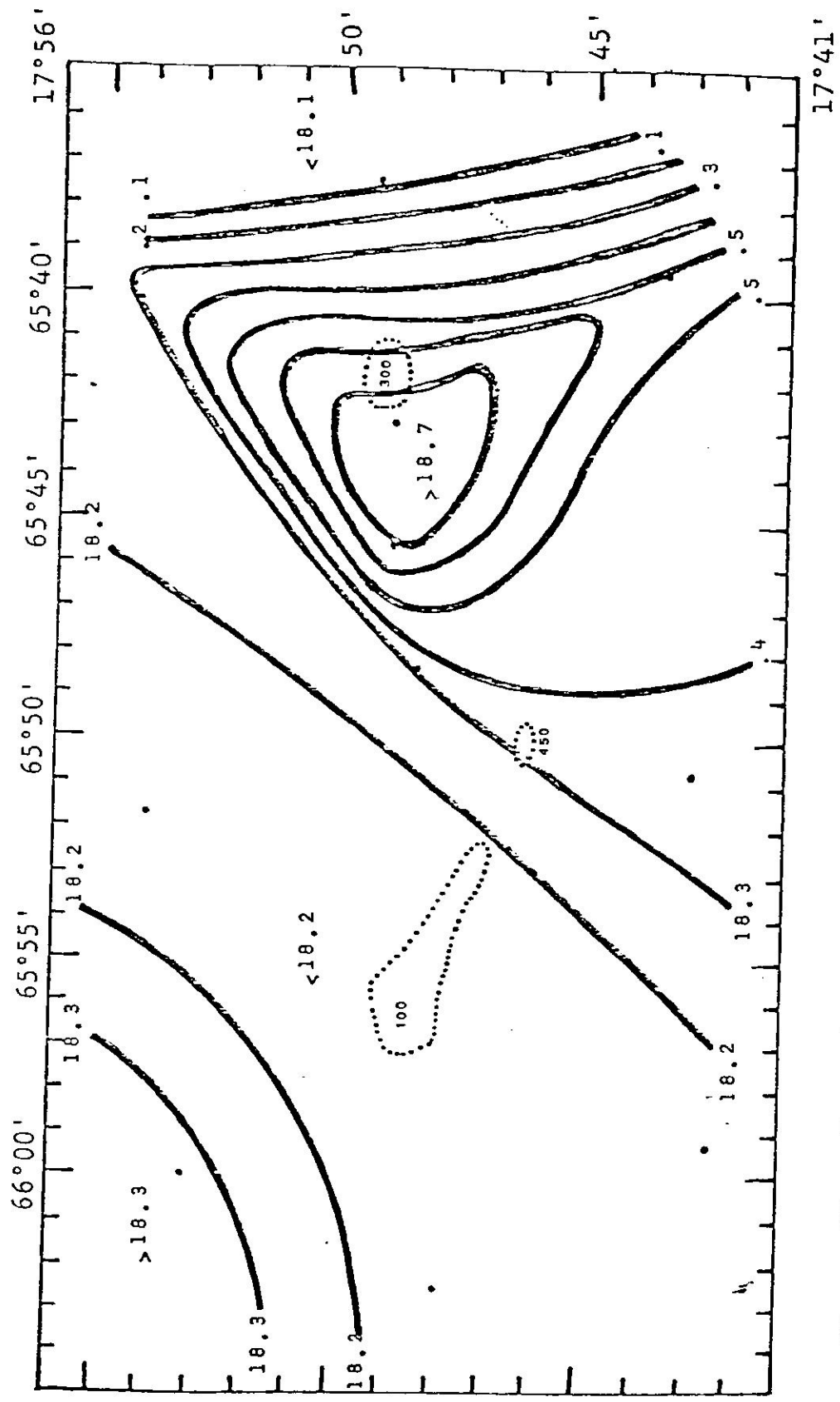
Figure 21c. Parameter contours at a depth of 250m: hydrcast temperature (°C).
95% F_c = 8.76, 90% F_c = 5.22, f_{sept} = 2.53, f_{nov} = 1.99.
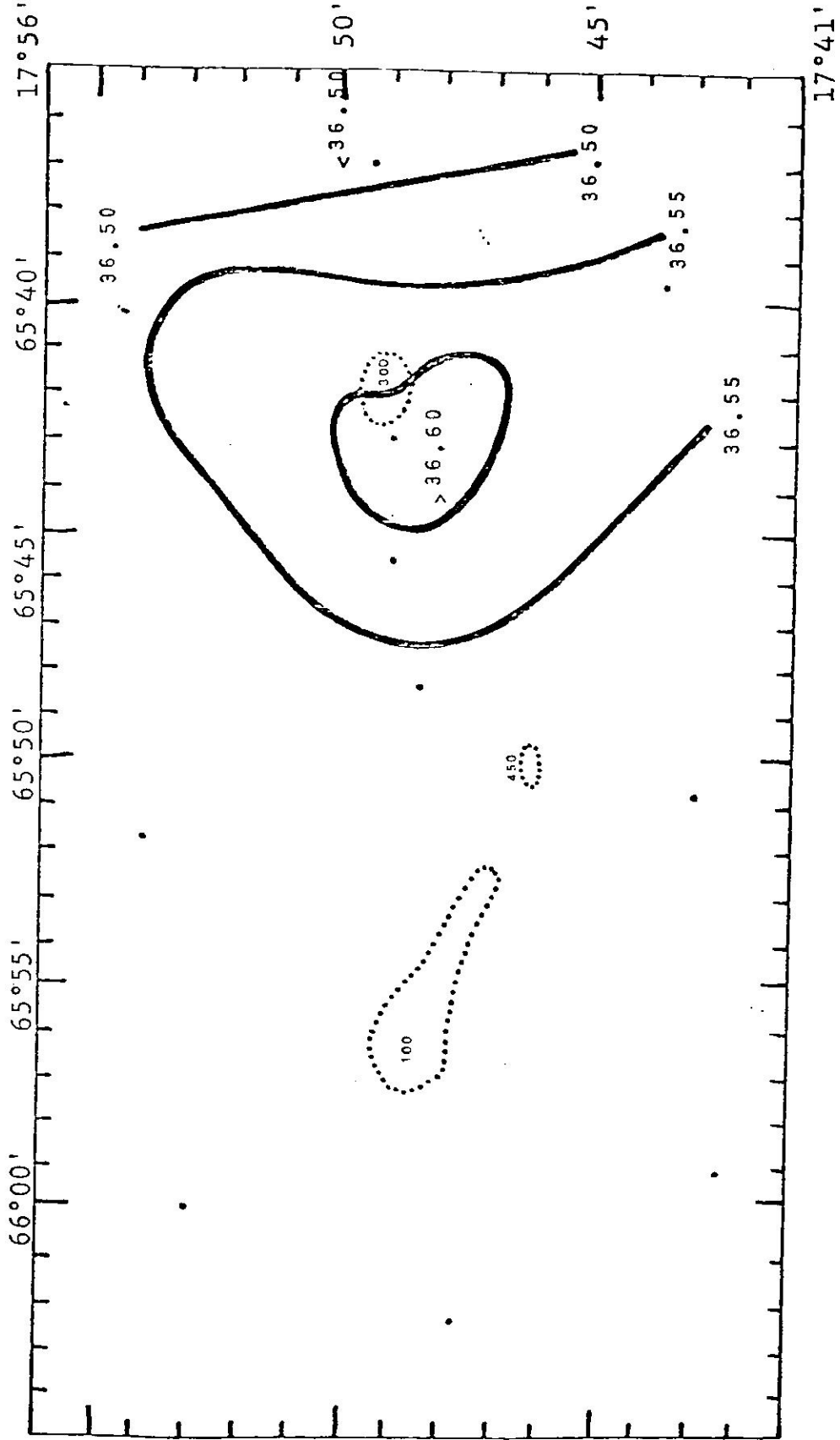
Figure 21d. Parameter contours at a depth of 250m; salinity (°/oo).
95% F_c = 8.76, 90% F_c = 5.22, F_c = 4.41, f_{sept} = 4.41, f_{nov} = 3.03.
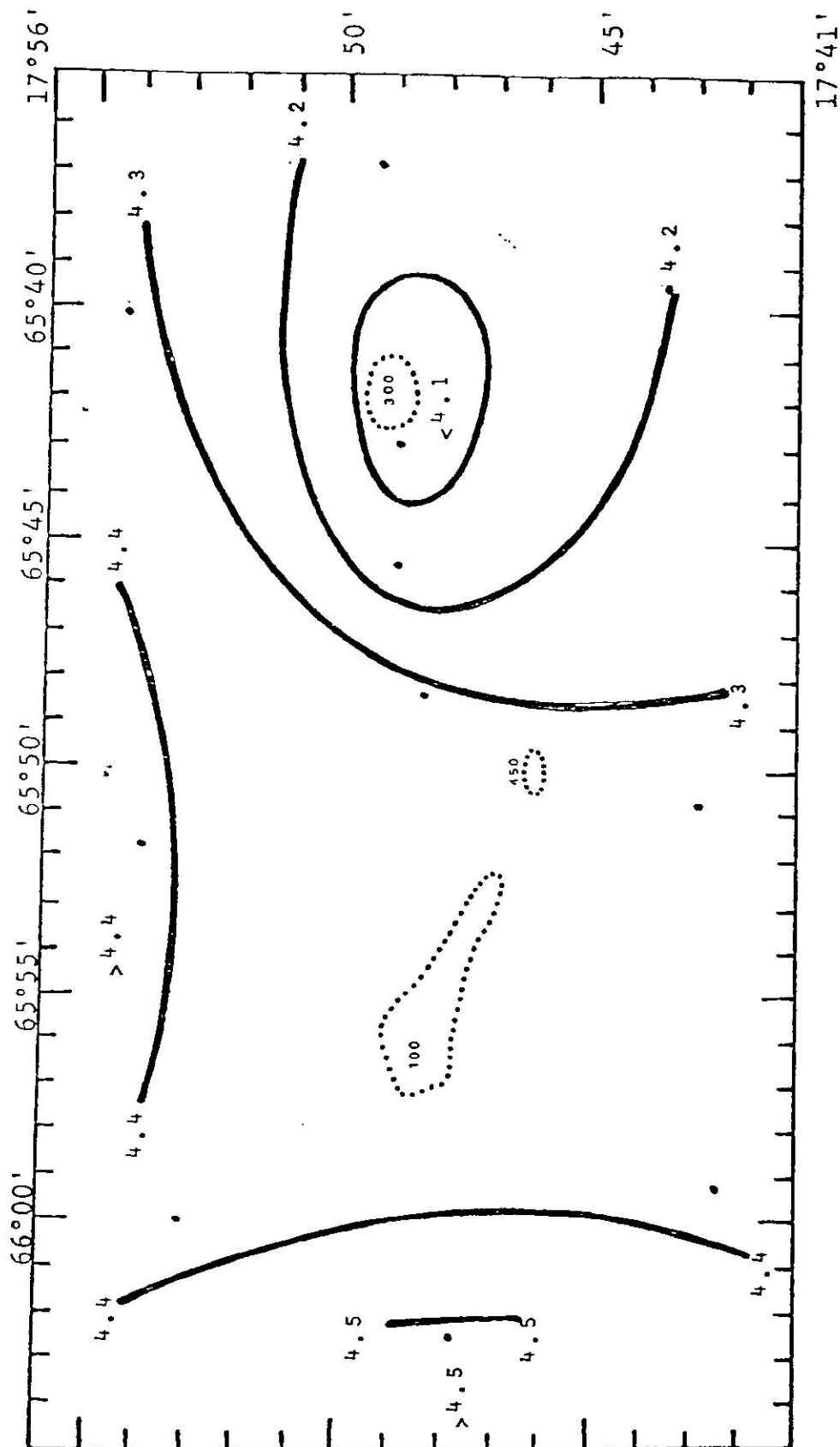
Figure 21e. Parameter contours at a depth of 250m: dissolved oxygen (ml/L). 95% F_c = 8.76, 90% F_c = 5.22, F_c = 5.22, f_{sept} = 22.0, f_{nov} = 49.6.

consistent with the model predictions. At this depth
interval, the salinity is decreasing with depth so the
expected salinity distribution is just the opposite as that
for the upper layers (<150m deep). The upward vertical
deflection of the isobaths and isohalines, calculated from
the mean depth profiles of salinity and temperature, is of
18 meters. The vertical, detectable, extent of both seamount
perturbations is within range of the predicted values
(Table IIc).

D. Depths Below 400m

Below a depth of 400m the f-ratios are generally lower
than one for all the parameters. Although this implies a
very weak signal, a well-defined southeast-northwest gradient
(low => high) shows in the salinity and temperature fields
as shown in figures 22d and 22c, respectively. This gradient
is consistent with the motion of the Antarctic Intermediate
Waters (AIW) thru this area. There are no closed contour
features associated with any of the seamounts at this
depth range.
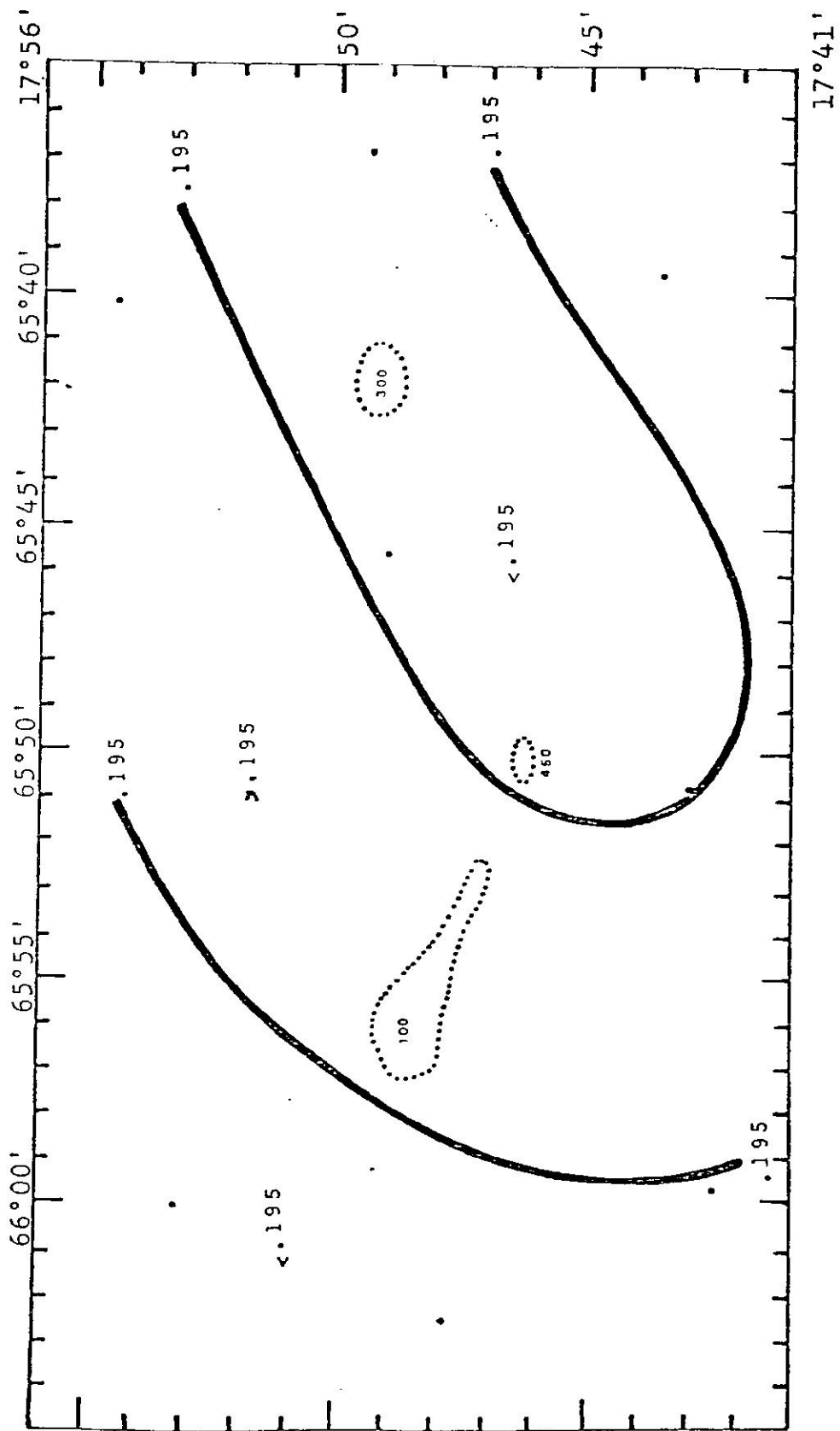
Figure 22a.   Parameter contours at a depth of 600m: dynamic height.
95% F_c = 8.79, 90% F_c = 5.23, f_{sept} = 0.18, f_{nov} = 0.27.
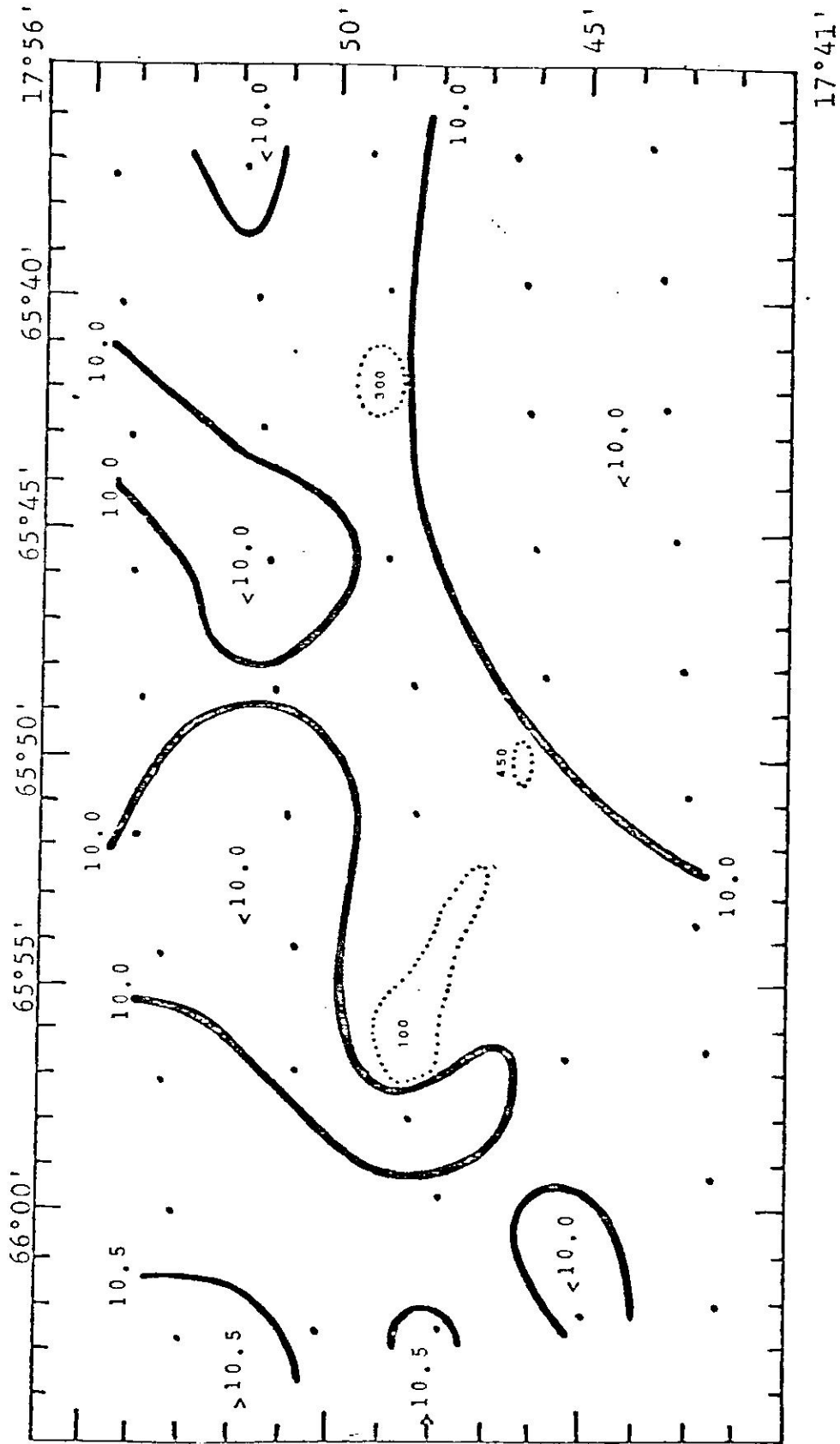
Figure 22b.   Parameter contours at a depth of 600m: XBT temperature   (°C).
95% F_c = 8.59, 90% F_c = 5.16, f_{sept} = 0.56, f_{nov} = 0.49.
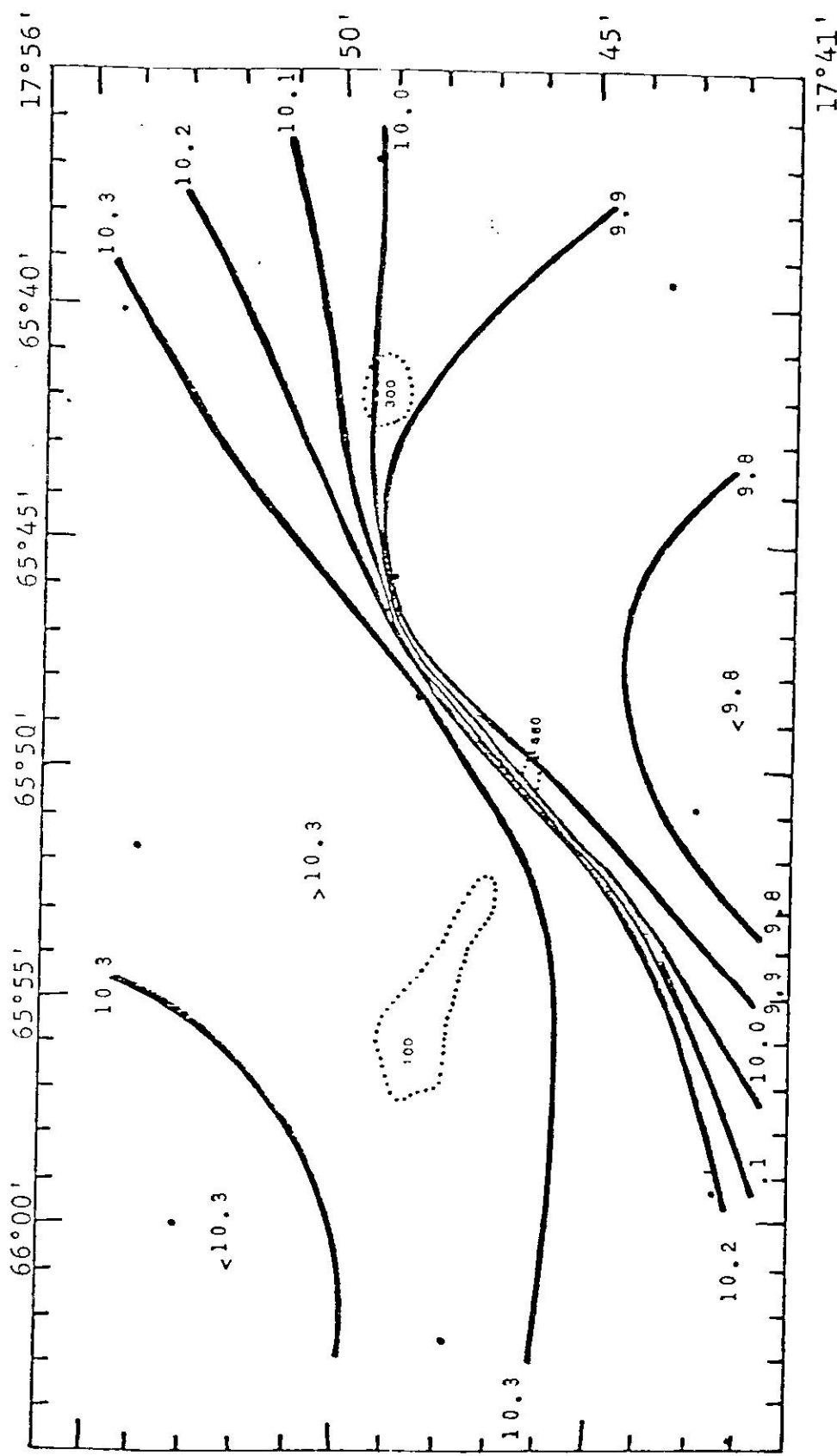
Figure 22c. Parameter contours at a depth of 600m: hydrocast temperature (°C). 95% F_c = 8.79, 90% F_c = 5.23, f_{sept} = 0.29, f_{nov} = 0.25.

87
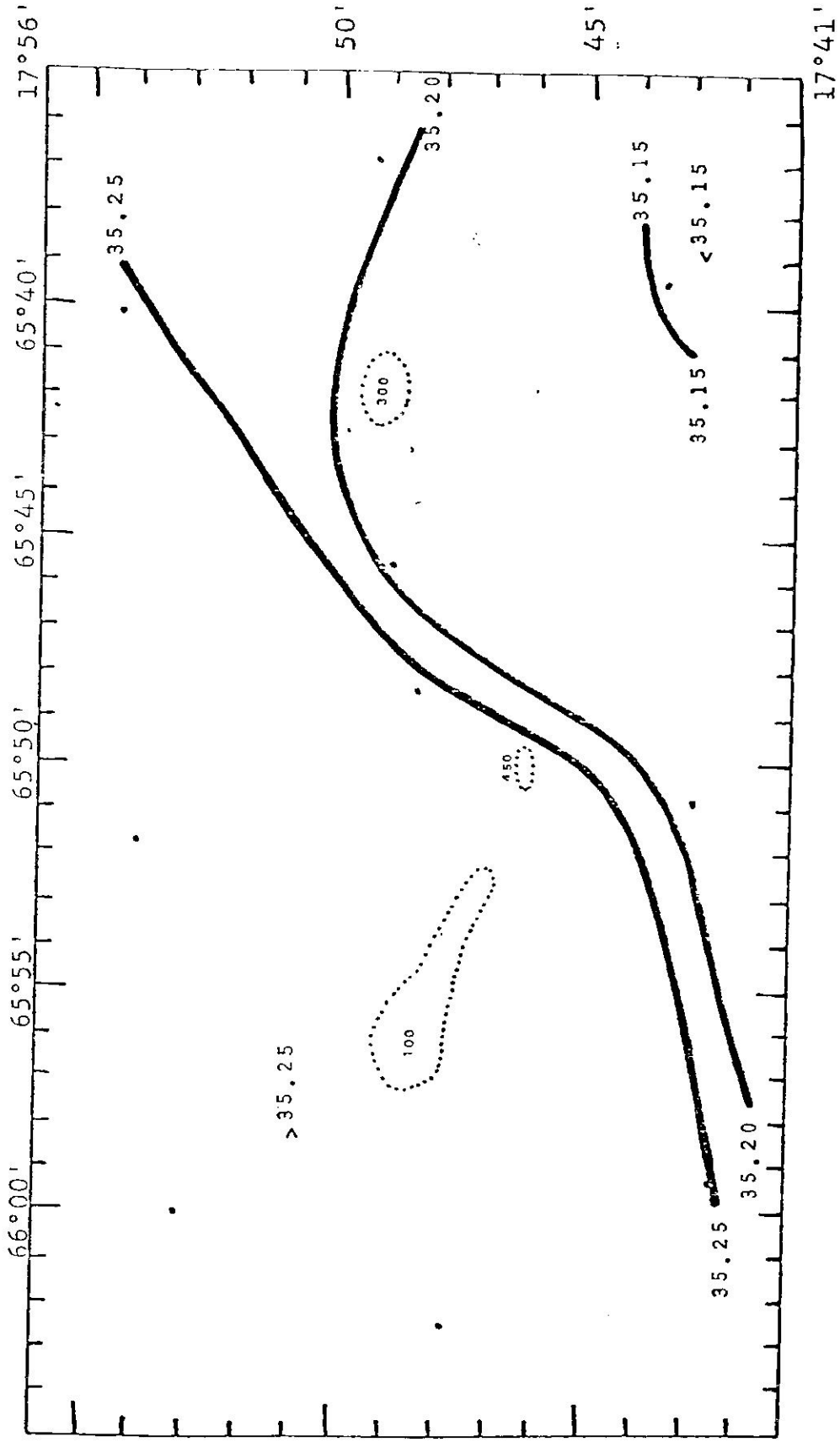
Figure 22d. Parameter contours at a depth of 600m: salinity (°/oo).
95% F_c = 8.79, 90% F_c = 5.23, f_{sept} = 0.53, f_{nov} = 0.21.
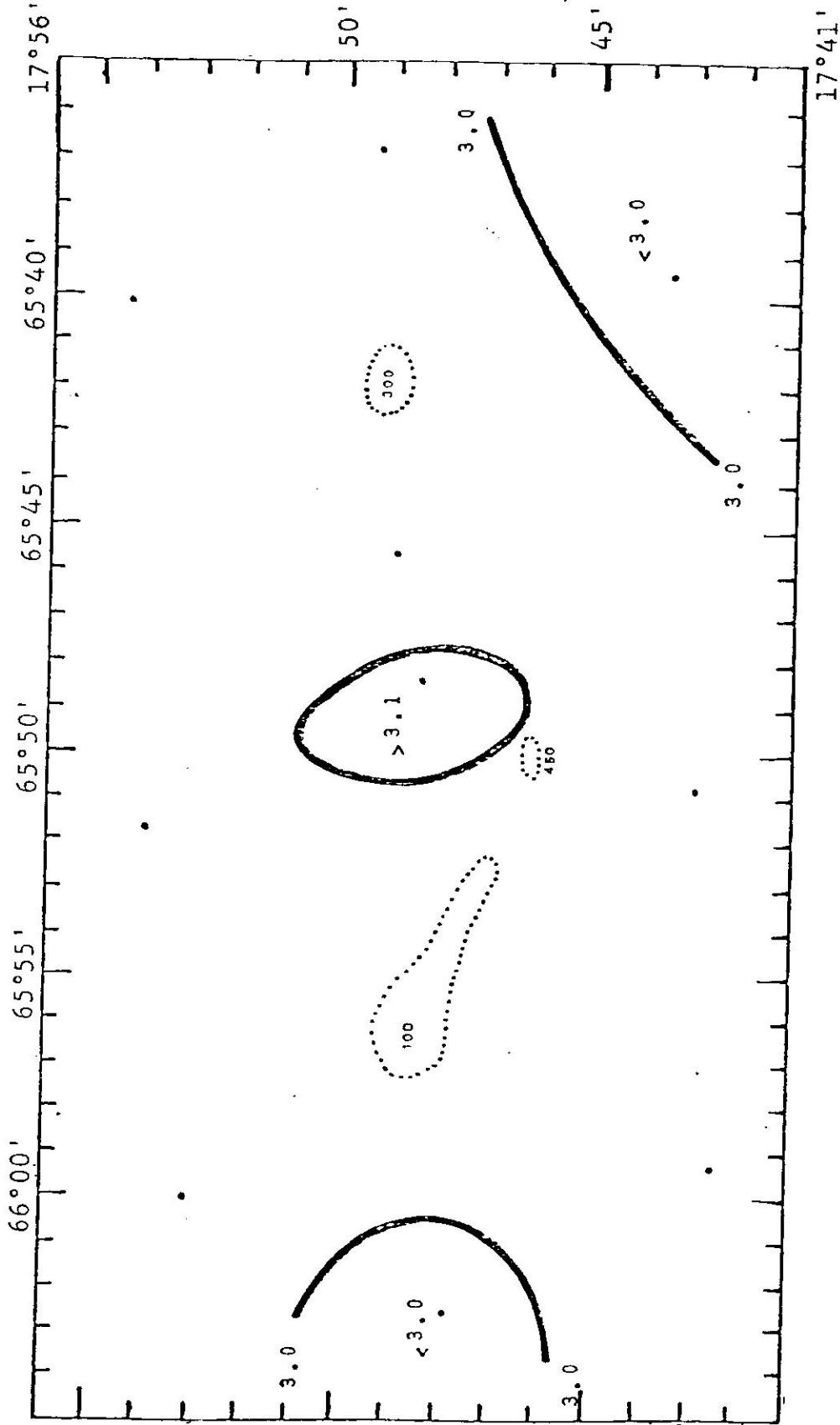
Figure 22e.   Parameter contours at a depth of 600m: dissolved oxygen (ml/L).
95% F_c = 8.79, 90% F_c = 5.23, f_{sept} = 5.2, f_{nov} = 0.21.

SUMMARY AND CONCLUSIONS

The geostrophic flow in the seamount area was in a south-southwest direction, being modified under the influence of Grappler Seamount. This result is corroborated by the close agreement with observed, synoptic, current meter data at a depth of 20m from the OTEC Benchmark.B, with (non-synoptic) Lagrangian drifter trajectories over and around Grappler Seamount and with the expected streamline pattern derived from numerical and analytical models.

The highest signal levels for all parameters were concentrated in the regions over and close to the top of both seamounts. A low temperature, high salinity and low dissolved oxygen dome was found in the same region where the flow was affected by the Grappler Seamount. A region of low salinity and low temperature was found upstream from Whiting Seamount while a high salinity, high temperature region was present in its downstream side. These observations of dynamic perturbations over the Grappler and Whiting Seamounts are consistent with the expected perturbation from an obstacle immersed in a rapidly rotating, stratified, slow moving fluid according to the theories of Hogg (1973), Huppert (1975) and Huppert and Bryan (1976).

Based upon the hydrodynamic parameters calculated from the field hydrographic data both seamounts were expected to produce Taylor Cone (also referred to as a seamount associated cold dome or anticyclonic eddy) type of perturbations as predicted by the numerical and analytical models. The agreement between field observations and model predictions suggest a highly dynamic environment in the seamount area with permanent or semi-permanent Taylor Cones present over both seamounts. The time dependent structure of such a dynamic phenomena will depend on the vertical stratification of the surface and subsurface water layers and the speed and persistence of the flow. Eddies shed during the formation stage of the Taylor Cone are also expected to occur. These shed eddies, with a length scale similar to the length scale of the generating seamount, could impact the insular shelf environment at surface and subsurface depths (for eddies shed from Grappler Seamount) or at depths below 100m (for eddies generated by the Whiting Seamount). An eddy-like feature was observed in Skylab images from June, 1973. This cyclonic eddy was located some 20km southwest of Grappler Seamount. Its size and position are suggestive of a seamount-eddy association.

Planktonic organisms, suspended particles, and floating or dissolved substances trapped during the formation of the cyclonic eddy are expected to drift

within the eddy for an unknown time period. During this time interval the biological, chemical, and physical characteristics of the eddy may change. If such an eddy comes in contact with the insular shelf of Puerto Rico it will induce changes in the circulation and water mass characteristics of the shelf environment, which will depend on the conditions at the time of the formation of the eddy, and the changes brought about during the advection period. The stationary anticyclonic eddy or Taylor Cone will only affect the environment in the immediate vicinity of the generating seamount. The residence time of the waters that form the Taylor Cone (and everything in them) will increase for as long as the perturbation persists. This trapped water mass may be important to the development of fish larvae and might explain the high fishing productivity of the seamount region.

The results from this study lead to the following conclusions:

1) Both seamounts are producing mesoscale perturbations thru interaction with the oncoming flow. Two types of perturbations are generated by the seamounts: (a) A stationary Taylor Cone (cold dome or anticyclonic eddy) that remains over the generating seamount, and (b) A cyclonic

eddy, formed during the formation stage of the Taylor Cone, which drifts downstream from the generating seamount.

2) These perturbations are qualitatively similar to those predicted by the numerical and analytical models of Hogg (1973), Huppert (1975) and Huppert and Bryan (1976). This agreement constitutes field verification of the models under conditions of high relative obstacle elevation and a small Coriolis parameter (low latitude).

3) The impact of an OTEC plant (reduction in the variable Δt) by the observed temperature perturbations would be small compared to the seasonal changes, but relatively large when compared to the monthly changes during the fall season. The maximum temperature drop at a depth of 20m, an OTEC plant's intake depth, over Grappler Seamount would produce a 2.3% (0.5°C) reduction in the thermal resource available to such a plant as compared to the 0.4% (0.08°C) maximum natural variability at the Benchmark B for the months of September and November (1980). The seasonal change is close to 4°C.

4) The results of the study suggest that
   further research is necessary, specially
   to understand the effects of the hydro-
   dynamic perturbations on the circulation
   near the coast and their influence upon
   the fishing potentialities around the
   seamounts. The temporal occurrence and
   persistence of the perturbations (temporal
   patterns) should be investigated to define
   the parametric regions which govern their
   behaviour. Observations should be conducted
   during the early spring months when the
   Grappler Seamount's top lies above the
   thermocline.

APPENDIX A

STATION POSITIONS: R/V CRAWFORD 8110
                     October 15-16, 1981

Station #	Latitude	Longitude
1	17 53.0	66 02.8
2	17 50.3	66 02.6
3	17 47.8	66 02.5
4	17 45.0	66 02.3
5	17 42.3	66 02.1
6	17 42.5	65 59.3
7	17 45.2	65 59.5
8	17 47.8	65 59.6
9	17 50.5	65 59.8
10	17 53.2	66 00.0
11	17 53.4	65 57.2
12	17 50.7	65 57.0
13a	17 48.5	65 58.0
13	17 48.0	65 56.8
14	17 45.3	65 56.7
15	17 42.6	65 56.5
16	17 42.8	65 53.6
17	17 45.5	65 53.8
18	17 47.9	65 54.0
19	17 50.8	65 54.1
20	17 53.5	65 54.3
21	17 54.0	65 51.7
22	17 51.0	65 51.3
23	17 48.4	65 51.2
24	17 45.7	65 51.0
25	17 43.0	65 50.8
26	17 43.1	65 48.0
27	17 45.8	65 48.2
28	17 48.5	65 48.4
29	17 51.2	65 48.5
30	17 53.9	65 48.7
31	17 54.1	65 45.9
32	17 51.4	65 45.7
33	17 49.0	65 45.6
34	17 46.0	65 45.4
35	17 43.3	65 45.2
36	17 43.5	65 42.3
37	17 46.2	65 42.5
38	17 49.0	65 42.9
39	17 51.5	65 42.8
40	17 54.2	65 43.0
41	17 54.4	65 40.2
42	17 51.7	65 40.0
43	17 49.0	65 39.8

STATION POSITIONS: (continued)

Station #	Latitude	Longitude
44	17 46.3	65 39.7
45	17 43.6	65 39.5
46	17 43.8	65 36.7
47	17 46.5	65 36.9
48	17 49.4	65 36.9
49	17 51.9	65 37.2
50	17 54.6	65 37.4

APPENDIX B

PROCEDURES FOR DATA ANALYSIS

B-1. Reiniger and Ross Interpolation Method

Let the parameter V take the values V1, V2, V3, V4 at the depths Z1, Z2, Z3, Z4 where Z1 through Z4 are the levels used for the interpolation in order of increasing depth. Let Vp be the interpolated value at a depth Z such that $Z1<Z2<Z<Z3<Z4$. Reiniger and Ross (1968) then calculate a weighted mean for the two hyperbola, using the following equations:

$$Vp = \frac{\left| Vr - Vp1 \right| Vp + \left| Vr - Vp2 \right| Vp1}{\left| Vr - Vp1 \right| + \left| Vr - Vp2 \right|}$$

where:

$$Vr = 0.5 \left[V23 + \frac{(V23 - V34)^2 \, V12 + (V12 - V23)^2 \, V34}{(V23 - V34)^2 + (V12 - V23)^2} \right]$$

$$Vp1 = O_{23}^1 \, V1 + O_{21}^2 \, V2 + O_{12}^3 \, V3$$

$$Vp2 = O_{34}^2 \, V2 + O_{42}^3 \, V3 + O_{23}^4 \, V4$$

$$O_{jk}^i = \frac{(Z - Z_j)(Z - Z_k)}{(Z_i - Z_j)(Z_i - Z_k)}$$

$$V_{ij} = \frac{V_i (Z - Z_j) - V_j (Z - Z_i)}{Z_i - Z_j}$$

An error estimate of the interpolated value is calculated by:

$$P = 0.33 \left[\left| (Vp - Vp1) \; (Vp - Vp2) \right| \right]^{0.5}$$

The interpolation scheme requires two observed values of a parameter above, and two below the interpolation depth. When this is not the case, a linear interpolation is performed or the data are not interpolated at all. If linear interpolation is used, the interpolated value is followed by "LI" in the precision code column. The following special cases can be distinguished:

1. When less than four depths have been observed. In case no interpolations are performed.

2. Near the surface. If less than two observations occur above Z, a linear interpolation using the two upper observations is performed. No extrapolations are made over a distance exceeding 13 meters or 1.3 x (Z2 -Z1), whichever is smaller.

3. Near the bottom. If less than two observations occur below Z, a linear interpolation using the two lowest observations is performed. No extrapolation is performed to depths exceeding the deepest observation by more than 10% of the depth difference between the deepest two observed levels.

4. The desired standard depth coincides with an observed depth. In this case the observed variables are transferred without change to the standard depth and "EX" is indicated in the precision code column.

5. Observed depths are spaced too far apart or too irregularly. This can occur if the bottles are purposely spaced closely at some levels, or if two partially overlapping casts are taken, of if values for the parameter are missing at two or more consecutive depths. Sample spacing, therefore, is checked as shown below and judged unacceptable if:

$$\frac{z_{j-1} - z_{j-2}}{z_j - z_{j-1}} < 0.2$$

or

$$\frac{z_{j+1} - z_j}{z_j - z_{j-1}} < 0.2$$

In the first case, with too small an interval between the upper two points, interpolation is carried out using z_{j-3}, z_{j-1}, z_j, z_{j+1} instead of z_{j-2}, z_{j-1}, $z1$, z_{j+1}. If lowest interval is too small, z_{j+1} will be replaced by z_{j+2}. In either case the equations are tested again before the interpolation is completed, and the procedure is repeated until they are satisfied or until surface or bottom is reached. When that happens, the value will be determined by linear interpolation using z_{j-1} and z_j.

6. The interpolation error is too large. Linear interpolation will be used when the error estimator P exceeds 0.1 for temperature, 0.01 for salinity or 20 units for any chemical parameter.

B-2. Sigma-t, Specific Volume and Specific Volume Anomaly

The following formulas were obtained from H.O. Pub. 614.

$Sigma\text{-}t = Sumt + (SgO + 0.1324)(1 - At + Bt(SgO - 0.1324))$

where:

$$Sumt = -\left[\frac{(t - 3.98)^2}{503.570}\right]\left[\frac{t + 238}{t + 67.26}\right]$$

$SgO = -0.069 + 1.4708C1 - 0.001570C1^2 + 0.0000398C1^3$

$At = t(4.7867 - 0.098185t + 0.0010843t^2)\ 10^{-3}$

$Bt = t(18.030 - 0.8164t + 0.01667t^2)\ 10^{-6}$

$C1 = Salinity/1.80655$

$t = $ temperature of water in °C

Specific Volume = A7 + A8 (A1 + A2 + A3 + A4 + A5 + A6)

where:

$A1 = 4886 / (1 + 0.00001832)$

$A2 = -(227 + 28.33t - 0.551t^2 + 0.004t^2)$

$A3 = (0.0001Z)(105.5 + 9.5t - 0.158t^2)$

$A4 = 1.5Z^2 t \times 10^{-8}$

$A5 = -((SgO - 28) / 10)((147.3 - 2.72t + 0.04t^2) - 0.0001Z (32.4\ 0.87t + 0.02t^2))$

$A6 = ((SgO - 28) / 10)^2 (4.5 - 0.1t - 0.0001Z (1.8 - 0.06t)$

$A7 = 1 / (1 + ((Sigma\text{-}t) \div 1000))$

$$A8 = -Z \times 10^{-9} \times A7$$

Specific Volume Anomaly = Specific Volume (in situ) −
Specific Volume (35,0, p)

B-3. Dynamic Height and Dynamic Height Anomaly

The formula for the calculation of dynamic heights is:

$$\text{Dyn. Height} = \int_{p_1}^{p_2} \alpha \, dp$$

$$\text{Dyn. Height Anom.} = \int_{p_1}^{p_2} (\alpha - 35, 0, p) \, dp = \int_{p_1}^{p_2} \delta \, dp$$

where:

α = Specific Volume

δ = Specific Volume Anom.

p = In situ pressure in decibars

Both equations are evaluated using the trapezoidal rule:

$$\text{D.H.}_{Z_n} = 0.5 \sum_{i=1}^{n} (\alpha_{Z_i} + \alpha_{Z_{i-1}})(Z_i - Z_{i-1})$$

$$\text{D.H.A.}_{Z_n} = 0.5 \sum_{i=1}^{n} (\delta_{Z_i} + \delta_{Z_{i-1}})(Z_i - Z_{i-1})$$

Where Z is the depth in meters.

B-4. Calculation of the Critical Parameters from the Numerical Models Using the Seamount Survey Data

Constants:

1. Grappler Seamount's elevation = 1400 meters

2. Whiting Seamount's elevation = 1200 meters

3. Mean depth at base of seamounts (H) = 1500 meters

4. Grappler's length scale (L) = 10 kilometers

5. Whiting's length scale (L) = 5 kilometers

6. Coriolis parameter (f) = 2 sin (18) = $4.51 \times 10^{-5} s^{-1}$

7. Brunt-Vaisala frequency = N = $\left(\dfrac{g \; \Delta\sigma^+}{\rho_o \; H} \right)^{0.5}$

where: ρ_o = in situ density (1/specific volume) at the bottom

      = 1.0347 grams/cm (at stations 21 and 45, the only reaching to 1500 meters)

$\Delta\sigma_+$ = difference in sigma-t between the bottom and the surface (0.005 g/cm at both stations) or between the bottom and 100 meters (0.003 for both stations)

g = force of gravity

   = 9.8 m/s^2

Substituting these values into the formula for N we get

$$N_{surf} = \left[\frac{9.8 \times 0.005}{1.0347 \times 1500} \right]^{0.5} = 0.006 \; rad/s$$

$$N_{100m} = \left[\frac{9.8 \times 0.003}{1.0347 \times 1400} \right]^{0.5} = 0.005 \; rad/s$$

I. Hogg (1973)

ho = obstacle's elevation

= H/L

$$U = \left[\frac{1}{H} \int_o^H U_o^* (Z^*)^2 \, d \, Z^* \right]^{\frac{1}{2}}$$

values from the seamount survey range from 10-15 cm/s but the following values were used for more general results: 1, 5, 10, 15 and 20 cm/s

E = U/fL

U*(0) = current speed at the obstacle's depth

= U due to the seamounts high relative elevation (ho/H)

Final numbers are shown in Table Ia.

II. Huppert (1975)

V = uniform flow far upstream from the obstacle

= the same values as for U were employed: 1, 5, 10, 15, 20 cm/s

B = NH/fL

R = V/fL

ho = maximum obstacle height / H

= ho/R; when B => (Huppert's equation 3.34)

Values of B and ho/R are shown in Table IIb.

III. Huppert and Bryan (1976)

hm = maximum obstacle height

Uo = barotropic velocity after a time to, used same values as for U and V

B = NH/fL (same as in Huppert (1975)

Values of Nhm/Uo are shown in Table IIc.

APPENDIX C

SATELLITE DATA

Table Ia. TIROS-NOAA Satellite Data

Date	Platform
January 24, 1980	NOAA-6
March 26, 1980	TIROS-N
March 27, 1980	TIROS-N
May 18, 1980	NOAA-6
June 30, 1980	TIROS-N
July 31, 1980	TIROS-N
November 29, 1980	NOAA-6
February 26, 1981	NOAA-6
March 2, 1981	NOAA-6
October 9, 1981	NOAA-7
October 10, 1981	NOAA-7

Two scenes were obtained for each date at different frequencies: visible (channel 1, 0.61um) and infrared (channel 4, 11um). The standard product obtained from NOAA-NESS is a 25-by-25 cm black and white contact print for each scene.

Table 1b. Landsat Satellite Data

Date	Platform	Sensor	I.D. #
August 12, 1976	Landsat 2	RBV	8258613563200
August 30, 1976	Landsat 2	RBV	8256813572200
March 29, 1978	Landsat 2	MSS	82116213390X0
May 31, 1978	Landsat 3	RBV	83008714045XA

RBV= Return Beam Vidicon (or television system)

MSS= Multispectral Scanner (four frequency bands: 0.5-0.6um, 0.6-0.7um, 0.7-0.8um and 0.8-1.1um)

Images supplied as black and white negatives.

Table Ic. Skylab Data

Date	Freq. Band	I.D #
June 9, 1973a	COL	G20A010181000
"	CIR	G20A009181000
"	B&W	G20A012173000
"	B&W	G20A011173000
June 9, 1973b	COL	G20A010182000
"	CIR	G20A009182000
"	B&W	G20A011174000
"	B&W	G20A012174000
November 30, 1973	CIR	G40A051087000
"	BIR	G40A049088000
"	BIR	G40A049087000

COL=0.4-0.7um : CIR=0.5-0.88um : B&W=0.5-0.6um and 0.6-0.7um

Images supplied as 2-by-2 negatives

REFERENCES

Anderson, G.C., 1971: Oxygen Analysis. Marine Technician's Handbook. SIO Ref. No. 71-10, Sea Grant Pub. No. 11, 29 pp.

Atwood, D.K., P. Duncan, M.C. Stalcup and M.J. Barcelona, 1976: Ocean thermal energy conversion: Resource Assessment and Environmental Impact for the proposed Puerto Rico Site. NSF Grant No. AER 75-00145, August 1976, 104 pp.

Carpenter, D.H., 1965: The Chesapeake Bay Institute technique for the Winkler dissolved oxygen method. Limnol. Oceanogr., 10, 141-143.

Davies, P.A., 1972: Experiments on Taylor columns in rotating stratified fluids. J. Fluid Mech., 54(4), 691-717.

Defant, A., 1940: Die ozeanographischen Verhaltnisse wahrend der Ankerstation des "Altair" am Nordrand des Hauptstromstriches des Golfstromes nordlich der Azoren. Ann. d. Hydr. u. Marit. Meteorol., 68.

Eide, L.I., 1979: Evidence of a topographically trapped vortex on the Norwegian continental shelf. Deep Sea Res., 26(6a), 601-621.

Fornshell, J.A., J.M. López and J. Capella, 1981: Eddy observations south of Puerto Rico. EOS, 62(17), pp. 305 (abs.).

_____ and J. Capella, 1982: Lagrangian current measurements in the Caribbean Sea South of Puerto Rico. EOS, 63(45), pp. 1000 (abs.).

Froelich, P.N. and D.K. Atwood, 1976: Dissolved silicate and salinity structure of the upper waters of the Venezuela Basin, Caribbean Sea. CICAR II Symposium Report, 299-314.

Goldman, G.C., M.L. Hernandez-Avila and J.A. Suarez-Caabro, 1979: A historical review of the physical and biological characteristics of the ocean near Puerto Rico, relative to an OTEC power plant. CEER-0-51, 318 pp.

Goldman, G.C., M.L. Hernandez-Avila, J.G. González and
     D. Pesante, 1979: Results of oceanic measurements
     relatable to an OTEC installation at Punta Tuna,
     Puerto Rico. CEER-0-57, 588 pp.

Gordon, A.L., 1967: Circulation of the Caribbean Sea.
     J. Geophys. Res., 72(24), 6207-6223.

Hide, R., 1961: Origin of Jupiter's Great Red Spot.
     Nature, 190, 895-896.

Hogg, N.G., 1973: On the stratified Taylor column.
     J. of Fluid Mech., 58(3), 517-537.

Huppert, H.E., 1975: Some remarks on the initiation of
     inertial Taylor columns. J. of Fluid Mech., 67(2),
     397-412.

_____ and K. Bryan, 1976: Topographically
     generated eddies. Deep Sea Res., 23, 655-679.

Kinard, W.E., D.K. Atwood and G.S. Guiese, 1974: Dissolved
     oxygen as evidence for 18 Sargasso Sea Water in the
     Eastern Caribbean Sea. Deep Sea Res., 21, 79-82.

Lafond, E.C., 1951: Processing Oceanographic Data. H.O.
     Pub. 614, 114 pp.

López, J.M., P.M. Yoshioka, J.G. González, J.E. Capella,
     J.A. Fornshell and J.A. Ramírez Barbot, 1981: The
     structure of the ocean off Punta Tuna, Puerto Rico in
     relation to OTEC. Proceedings of the Eighth Ocean
     Energy Conference, 565-573.

McCartney, M.S., 1975: Inertial Taylor columns on a beta
     plane. J. of Fluid Mech., 68(1), 71-96.

Metcalf, W.G., 1976: Water exchange between the Atlantic
     Ocean and the Caribbean Sea. CICAR II Symposium
     Report, 63-77.

Molinari, R., R.L. Spillane, I. Brooks, D. Atwood and
     C. Duckett, 1981: Surface currents in the Caribbean
     Sea as deduced from lagrangian observations. J.
     Geophys. Res., 86(C7), 6537-6542.

Morrison, J.M. and W.D. Nowlin, 1982: General distribution
     of water masses within the Eastern Caribbean Sea during
     the winter of 1972 and fall of 1973. J. of Geophys.
     Res., 87(C6), 4207-4229.

Nelepo, B.A., V.N. Stepanov, R.P. Bulatov and M.M. Domanov, 1976: Soviet investigations of the dynamics and properties of the Caribbean Sea and Gulf of Mexico. CICAR II Symposium Report, 119-131.

Owens, W.B. and N.G. Hogg, 1980: Oceanic observations in stratified Taylor columns near a bump. Deep Sea Res., 27A, 1029-1045.

Proudman, J., 1916: On the motion of solids in a liquid possessing vorticity. Proc. Roy. Soc., A92, 408-424.

Reiniger, R.F. and C.K. Ross, 1968: A method of interpolation with application to oceanographic data. Deep Sea Res., 15, 185-193.

Richardson, P.L., 1981: Gulf Stream trajectories measured with free drifting buoys. J. of Phys. Oceanog., 11, 999-1019.

Roden, G.I., B.A. Taft and C.C. Ebbesmeyer, 1982: Oceanographic aspects of the Emperor Seamounts Region. J. of Geophys. Res., 87(C12), 9537-9552.

Royer, T.C., 1975: Ocean eddies generated by seamounts in the North Pacific. Science, 199, 1063-1064.

Schmitz, W.J., Jr., J.F. Price, P.L. Richardson, W. Brechner Owens and D.C. Webb, 1981: A preliminary exploration of the Gulf Stream System with SOFAR floats. J. of Phys. Oceanog., 11, 1194-1204.

Sokal, R.R. and J. Rohlf, 1969: Biometry. W.H. Freeman and Co., San Francisco, 776 pp.

_____ _____ _____ _____: Statistical Tables. W.H. Freeman and Co., San Francisco, 253 pp.

Sturges, W., 1965: Water characteristics of the Caribbean Sea. J. Mar. Res., 23(1), 147-161.

Swallow, J.C. and B.V. Hamon, 1960: Some measurements of deep currents in the eastern North Atlantic. Deep Sea Res., 6, 155-168.

Tabata, S., 1982: The anticyclonic, baroclinic eddy off Sitka, Alaska, in the Northeast Pacific Ocean. J. of Phys. Oceanog., 12, 1260-1282.

Taylor, G.I., 1917: Notion of solids in fluids when the flow is not irrotational. Proc. Roy. Soc., A93, 99-113.

_____, 1923: Experiments on the motion of solid bodies in rotating fluids. Proc. Roy. Soc., A106, 213-218.

Trumbull, J.V.A., P. Wilde, T.E. Chase, W.R. Normark, C.P. Miller, B.A. Seekins and J.D. Young, 1981: Oceanographic data off Puerto Rico and the Virgin Islands. LBL Pub. 360, Lawrence Berkeley Laboratory, University of California. (poster)

Vastano, A.C. and B.A. Warren, 1976: Perturbations to the Gulf Stream by the Atlantis II Seamount. Deep Sea Res., 23, 681-694.

Worthem, S. and F. Ostapoff, 1976: The response of the Tropical North Atlantic to meteorological forcing functions. CICAR II Symposium Report, 505-530.

Wust, G., 1964: Stratification and circulation in the Antillean-Caribbean Basins. Columbia Univ. Press, New York, 201 pp.